University of Alberta

DYNAMIC MODELLING AND CONTROL OF A SOLID OXIDE FUEL CELL

by

Achara Chaisantikulwat 

A thesis submitted to the Faculty of Graduate Studies and Research
in partial fulfillment of the requirements for the degree of

Master of Science

in

Process Control

Department of Chemical and Materials Engineering

Edmonton, Alberta
Fall 2006

Your file Votre référence
ISBN: 978-0-494-22237-9
Our file Notre référence
ISBN: 978-0-494-22237-9

Abstract

Most solid oxide fuel cell (SOFC) modelling efforts emphasize steady-state cell operation. However, understanding the dynamic behaviour is essential to predict the performance and limitations of SOFC power systems. This thesis presents the development of a dynamic model of a SOFC, and a feedback control scheme that can maintain output voltage despite load changes. Dynamic responses are determined as the solutions of coupled partial differential equations derived from conservation laws of charges, mass, momentum, and energy. To obtain the performance curve, the dynamic model is subjected to varying load current for different fuel specifications. From such a model, the voltage responses to step changes in the fuel concentration and load current are determined. Low-order dynamic models that are sufficient for feedback control design are derived from the step responses. The development of the partial differential equation model is outlined, and the limitations of the control system are discussed.

Acknowledgements

I would like to express my gratitude to my supervisor, Dr. Carolina Diaz-Goano. Her untiring advice, support and words of encouragement have had a significant influence on my degree completion. I am also indebt to Dr. Edward Scott Meadows for his supervisory throughout my academic program. I could not have made this accomplishment without his guidance and remarkable commitment to be actively involved in this work.

I would like to extend my thanks to friends and colleagues at the Department of Chemical and Materials Engineering who have given me insightful information and technical guidance and support towards this research.

This research was made possible in part by funding from the Alberta Energy and Research Institute (AERI). The additional financial support from the Department of Chemical and Materials Engineering at the University of Alberta is gratefully acknowledged.

Table of Contents

1 Introduction 1
- 1.1 Status of Dynamic SOFC Modelling and Control . . . 2
- 1.2 Research Objective . . . 5
- 1.3 Overview . . . 5

2 Fuel Cell Overview 7
- 2.1 Introduction . . . 7
  - 2.1.1 Fuel Cells Types . . . 8
  - 2.1.2 Advantage and Disadvantage of Fuel Cells . . . 9
- 2.2 Solid Oxide Fuel Cells . . . 11
  - 2.2.1 Cell Reactions . . . 12
  - 2.2.2 SOFC Component Materials . . . 12
  - 2.2.3 Design of a Single Cell . . . 15
- 2.3 SOFC Performance . . . 20
  - 2.3.1 Thermodynamics of Solid Oxide Fuel Cells . . . 20
  - 2.3.2 Equilibrium Potential . . . 21
  - 2.3.3 Voltage and Overpotentials . . . 22
  - 2.3.4 Electrochemical Kinetics . . . 23
  - 2.3.5 Reactant Utilization . . . 24

3 Dynamic Model Development 27
- 3.1 Introduction . . . 27
- 3.2 Modelling Assumptions . . . 27
- 3.3 Modelling Geometry . . . 28
- 3.4 Transport Equations . . . 29
  - 3.4.1 Ionic Charge Transport . . . 30
  - 3.4.2 Electronic Charge Transport . . . 33
  - 3.4.3 Mass Transport . . . 35
  - 3.4.4 Momentum Transport . . . 42
  - 3.4.5 Heat Transport . . . 46
- 3.5 Mesh . . . 52
  - 3.5.1 Solver Settings . . . 52

4 Numerical Results and Discussion 54
- 4.1 Introduction . . . 54
- 4.2 Parameters Settings and Solution Algorithm . . . 54
- 4.3 Steady-State Analysis . . . 57
  - 4.3.1 Steady-state Modelling Results . . . 57
  - 4.3.2 Steady-state Model Validation . . . 77
  - 4.3.3 Mass Balance Verification . . . 80
- 4.4 Dynamic Analysis . . . 81

4.4.1 Nominal Operating Condition 82
4.4.2 Dynamic Modelling Results 83
4.4.3 Dynamic Model Validation 90

5 Process Control of SOFC **94**
5.1 Introduction 94
5.2 Low-Order Dynamic Model 95
5.3 Feedback Control 97
5.3.1 Closed-loop SOFC System Response 98

6 Conclusion **105**
6.1 Future Work 106

Bibliography **108**

Appendix **112**

A Thermodynamics of Hydrogen Fuel Cell **112**
A.1 Enthalpy of Reaction 112
A.2 Entropy of Reaction 112
A.3 Gibbs Free Energy 113
A.3.1 Standard Electrode Potential 114

B Estimation of Gas Property **116**
B.1 Gas Binary Diffusivity 116
B.2 Dynamic Viscosity of Multicomponent Gas Mixtures 117
B.3 Isobaric Heat Capacity of Multicomponent Gas Mixtures 119
B.4 Thermal Conductivity of Multicomponent Gas Mixtures 120
B.5 Convective Heat Transfer Coefficient 121

C Modelling Parameters **122**

List of Tables

2.1 Type of fuel cells and their components, operating conditions, and reactions [12, 20]. 10

3.1 Dimension of solid oxide fuel cell modelling domain. 31
3.2 Summary of 3D mesh parameters. 53

4.1 Simulation parameters for the half-channel SOFC model. 56
4.2 Comparison of the simulated results with the experimental results from Keegan et al. [29]. 78
4.3 Summary of the component balance in the steady-state analysis. 80
4.4 Summary of the simulated and theoretical reactant consumptions and product generation. 81
4.5 Summary of nominal SOFC operating condition for the dynamic model. . . 82
4.6 Steady-state gains in the output voltages with respect to the load step changes. 85
4.7 Steady-state gains in the output voltages with respect to the changes in the inlet hydrogen compositions. 88
4.8 Comparison of the dynamic modelling results at 750°C and 0.8 A/cm^2 with the interpolated results from Keegan et al. [29]. 90

A.1 Summary of molar enthalpy and entropy at 298.15 K and 0.1 MPa for the hydrogen fuel cell [31]. 113

B.1 Collision diameter and dimensionless temperature parameter from the Lennard-Jones potentials [10]. 117
B.2 Coefficients to calculate the dynamic viscosity in Equation (B.6) 118
B.3 Gas property data used in the dynamic viscosity of a gas mixture calculation 119
B.4 Coefficients to calculate the isobaric heat capacity of pure gas in Equation (B.10) 119
B.5 Coefficients to calculate the gas thermal conductivity in Equation (B.13) . . 120

C.1 Modelling parameters 122

List of Figures

2.1 Schematic diagram of a fuel cell. 7
2.2 Fuel cell types and fuel processing overview [12]. 8
2.3 Application of Fuel cells [31]. 9
2.4 Solid oxide fuel cell Technology [13]. 11
2.5 Schematic diagram of mass and charges flow in SOFC components. 13
2.6 Ionic conductivity of various electrolyte materials as a function of dimensionless temperature [27]. 13
2.7 Three-phase boundary location [28]. 14
2.8 Siemens Westinghouse tubular SOFC design [46]. 16
2.9 Planar SOFC cross-current flow (a) [46], and counter-current flow (b) design. 17
2.10 Planar SOFC co-current flow monolithic design [46, 33]. 17
2.11 Electrolyte-supported and anode-supported planar SOFC [1]. 18
2.12 Planar solid oxide fuel cell [11]. 19
2.13 SEM cross section image of a planar solid oxide fuel cell [11]. 19
2.14 Current-voltage relationship in local electrodes. 23
2.15 Cell voltage and its limitations with respect to the current density [3]. . . . 25
2.16 Overall fuel cell performance showing the relative voltage losses. 26

3.1 Schematic diagram of an anode-supported planar SOFC. 29
3.2 SOFC modelling domain. 30
3.3 Applicable domain for ionic charge transport. The arrows indicate the direction of ionic current flow. 32
3.4 Ionic and electronic charges flow direction at the electrode-electrolyte boundaries 33
3.5 Applicable domains for electronic charge transport. The arrows indicate the direction of electronic current flow. 34
3.6 Applicable domains for mass transport (air). 39
3.7 Applicable domains for mass transport (fuel). 41
3.8 Applicable domains for momentum transport. 44
3.9 Applicable domain for momentum transport in porous media. 45
3.10 Applicable domains for solid temperature modelling. 49
3.11 Geometry for the view factor calculation. 50
3.12 Mapped mesh for 3D geometry. 52

4.1 Computational algorithm for steady-state and dynamic SOFC model analysis. 55
4.2 Predicted cell voltage and power density as a function of current density at 750°C. The solid line represents the voltage, and the dashed line represents the power density. 58
4.3 Potential losses as a function of current density for 49% H_2 fuel. 60
4.4 Cross-sectional voltage (x = 9.5 mm) with arrows showing the direction of the current flow. The arrow magnitude is proportional to the current density. 61

4.5 Cross-sectional SOFC showing streamlines of current density (x = 0 mm) for 49% H_2 fuel at 0.8 A/cm^2. 62
4.6 Activation overpotential at the cathode-electrolyte interface for 49% H_2 fuel at 0.8 A/cm^2. 63
4.7 Local potentials at the cathode-electrolyte interface (x = 9.5 mm) for 49% H_2 fuel at 0.8 A/cm^2. 64
4.8 Activation overpotential at the anode-electrolyte interface for 49% H_2 fuel at 0.8 A/cm^2. 65
4.9 Local potentials at the anode-electrolyte interface (x = 9.5 mm) for 49% H_2 fuel at 0.8 A/cm^2. 66
4.10 Molar fraction of hydrogen in the anode and the fuel channel for 49% H_2 fuel at 0.8 A/cm^2. 67
4.11 Molar fraction of water in the anode and the fuel channel for 49% H_2 fuel at 0.8 A/cm^2. 67
4.12 Molar fraction of hydrogen and water across the anode and the fuel channel (x = 9.5 mm, y = 0) for 49% H_2 fuel at 0.8 A/cm^2. 68
4.13 Molar fraction of oxygen in the cathode and the air channel for 49% H_2 fuel at 0.8 A/cm^2. 69
4.14 Molar fraction of oxygen across the cathode and the air channel (x = 9.5 mm, y = 0) for 49% H_2 fuel at 0.8 A/cm^2. 70
4.15 Fluid velocity in the electrodes and the gas channels. The arrows show the gas flow directions with the arrow magnitude being proportional to the velocity magnitude. 71
4.16 Pressure in the gas channels and the porous electrodes for 49% H_2 fuel at 0.8 A/cm^2. 72
4.17 Solid temperature of the electrolyte, electrodes, and interconnects for 49% H_2 fuel at 0.8 A/cm^2. 73
4.18 Solid temperature across the electrodes and electrolyte (x = 9 mm, y = 1 mm) for 49% H_2 fuel at 0.8 A/cm^2. 74
4.19 Cross-sectional solid temperature at various interfaces along SOFC length (y = 0.25 mm) for 49% H_2 fuel at 0.8 A/cm^2. 75
4.20 Cross-sectional solid temperature at various interfaces along SOFC width (x = 8.4 mm). 76
4.21 Fluid temperature in the gas channels for 49% H_2 fuel at 0.8 A/cm^2. 77
4.22 The experimental cell voltage as a function of current density at 750°C [29]. 79
4.23 Output voltage responses (a) and the temperature responses (b) to step changes in load current densities (c). 84
4.24 Time responses of the anode (a) and cathode (b) activation overpotentials to step changes in load current densities. 86
4.25 Time responses of hydrogen (a), water (b), and oxygen (c) outlet mass fluxes to step changes in load current densities. 87
4.26 Output voltage responses (a) and the temperature responses (b) to step changes in inlet hydrogen molar fractions (c). 89
4.27 Time responses of the anode (a) and cathode (b) activation overpotentials to step changes in inlet hydrogen molar fractions. 91
4.28 Time responses of hydrogen (a), water (b), and oxygen (c) outlet mass fluxes to the step changes in inlet hydrogen molar fractions. 92
4.29 Interpolation of cell performance curve for 38%, 55%, and 60% hydrogen fuel. 93

5.1 Block diagram of the SOFC system with two process transfer functions. . . 95

5.2 Block diagram for the SOFC system with feedback control. 98
5.3 Open-loop and closed-loop feedback control diagram in MATLAB Simulink. 99
5.4 Closed-loop voltage responses (a) and controller output responses (b) for the proportional control settings. 100
5.5 Closed-loop voltage responses (a) and controller output responses (b) for the proportional and integral control settings. 102
5.6 Closed-loop voltage responses (a), open-loop voltage (b), and controller output responses (c) under various load changes obtained from the PI controller settings: $K_c = 1$, $\tau_I = 10$ s. 104

A.1 Change in Gibbs free energy of water formation at standard state (0.1 MPa) as a function of temperature [16]. 114
A.2 Standard electrode potential of a hydrogen fuel cell as a function of temperature at 0.1 MPa 115

List of Symbols

a	Stoichiometric coefficient	
AU	Percentage of air utilization	%
C_p	Isobaric molar heat capacity	J/kgK
D_{ik}	Binary diffusivity between species i and k	m^2/s
$\tilde{D}_{ik}$	Multicomponent Fick diffusivity between species i and k	m^2/s
D_K	Knudsen diffusivity	m^2/s
E	Electrical potential	V
E	Potential field	V/m
e	Error signal	
E_{act}	Activation energy	J/mol
F	Faraday's constant	96,484.56 C/mol e^-
$\hat{F}$	Radiative view factor	
FU	Percentage of fuel utilization	%
G	Gibbs free energy	J/mol
G_C	Controller transfer function	
G_L	Disturbance transfer function	
G_P	Process transfer function	
h	Convective heat transfer coefficient	$W/(m^2K)$
h_i	Species enthalpy of i	J/kg
J	Current density	A/m^2
J_o	Exchange current density	A/m^2
j_i	Mass flux of species i	$kg/(m^2s)$
k	Thermal conductivity	W/mK

k_B	Boltzmann's constant	1.38066×10^{-23} J/K
K_c	Controller gain	
K_P	Process steady-state gain	
K_L	Disturbance steady-state gain	
$\dot{m}$	Mass flow rate	kg/s
MW	Molecular Mass	kg/mol
N	Number of gaseous species	
n_e	Number of electron	
P	Pressure	Pa
P_i	Partial pressure of species i	Pa
P_{ref}	Reference pressure	Pa
Q	Heat source	W/m^3
R	Universal gas constant	8.314 J/(molK)
$\hat{R}$	Reaction rate	$kg/(m^3s)$
r_i	Production or consumption rate of species i	$kg/(m^2s)$
R_Ω	Resistivity	Ωm^2
$\bar{r}_i$	Mean pore radius	m
S	Entropy	J/(molK)
$\hat{S}$	Current Source	A/m^3
T	Temperature	K
u	Controller output	
$\mathbf{u}$	Velocity field	m/s
V	Voltage or potential	V
W_e	Electrochemical work	J/mol
w_i	mass fraction of species i	
x_i	Molar fraction of species i	
y	Controller output	

Greek symbols

α	Apparent transfer coefficient in the Butler-Volmer equation

γ	Pre-exponential coefficient	
δ	Layer thickness	m
ϵ	Emissivity	
ε	Porosity	m^3/m^3
η_{act}	Activation overpotential	V
η_{conc}	Concentration overpotential	V
κ	Permeability	m^2
μ	Dynamic viscosity	kg/(ms)
ν_i	Mean molecular velocity	m/s
ρ	Density	kg/m^3
$\hat{\rho}$	Charge density	C/m^3
σ	Conductivity	S/m
$\hat{\sigma}_{ik}$	Average collision diameter between species i and k	Å
$\tilde{\sigma}$	Stefan-Boltzmann constant	5.67×10^{-8} $W/(m^2K^4)$
τ	Tortuosity	$(m/m)^2$
$\vec{\tau}$	Stress tensor	$kg/(ms^2)$
τ_D	Derivative time	s
τ_I	Integral time	s
τ_L	Disturbance time constant	
τ_P	Process time constant	
$\hat{\Omega}_{D,ik}$	Collision integral between species i and k	

Superscripts

$\circ$	Property at standard state pressure, $P^\circ = 0.1$ MPa
eff	Effective parameter in porous medium

Subscripts

A	Anode
AI	Anode Interconnect
ave	Average
$bulk$	Bulk property

C	Cathode
$cell$	Fuel cell property
CI	Cathode Interconnect
E	Electrolyte
el	Electronic property
eff	Effective parameter in porous medium
f	Fluid property of reactive gas
in	Inlet condition
io	Ionic property
$load$	Load resistance
mix	Property of gas mixture
OCV	Open circuit voltage condition
out	Outlet condition
rev	Reversible energy
s	Solid property of fuel cell components
sp	Set-point value
$wall$	Gas channel wall

Chapter 1

Introduction

In the continuous pursuit to generate clean, low-emission power, fuel cells appear to be an attractive alternative. Fuel cells have the ability to convert electrochemical energy directly to electricity, making high efficiency achievable. Unlike fossil fuels, fuel cells distribute reliable power generation without emission of NO_x, SO_x, and other volatile organic compounds. Hydrogen fuel source for fuel cell application offers clean electricity and high-quality heat with only water as a by-product. Thus, fuel cells can potentially provide long-term benefits to the reduction of greenhouse gasses emission from the power generation and transportation industries.

Solid oxide fuel cells (SOFC) have emerged as one of the leading fuel cell technologies which can be used in a wide range of commercial applications. A distinguished feature of SOFC is the solid ceramic electrolyte which provide ease of handling and corrosion maintainability compared with liquid-electrolyte fuel cells. SOFC operate on the principle that ion oxides of oxygen are transported through ceramic electrolyte. High operating temperatures in the range of 600°C–1,000°C increase the cell performance by facilitating electrochemical kinetics and mass diffusion mechanisms, and reducing ohmic resistance. Conventionally, SOFC require hydrogen as a fuel source. They are also capable of internally reforming hydrocarbon fuels into hydrogen and carbon monoxide, which can participate in the electrochemical reactions to produce oxygen ions. Since SOFC can directly employ a variety of hydrocarbon fuel source, they are fuel flexible.

Unfortunately, high manufacturing costs, performance improvement setbacks, and fuel infrastructure still remain as major challenges for the commercialization of SOFC. A key

contribution to the development of SOFC involves complete knowledge of transport phenomena, electrochemical and surface chemical reactions in improved electrode and electrolyte materials. In recent years, the number of computational models of SOFC has been gradually increasing. The modelling progress has significantly contributed to the development of SOFC.

SOFC operations are not always at steady-state. The transient operations specifically dominate for fuel cells in transportation applications. Recent research activities have increasingly focused on fuel cell dynamics to accommodate practical operations. Since SOFC operate at elevated temperatures, their transient operations during start up, cool down, and load changes often lead to material degradation caused by spontaneous temperature change. The development of a physically-based model can provide significant insights into the dynamic behaviour of SOFC. With a comprehensive dynamic SOFC model, various sensitivity analyses can be performed.

The dynamic model simulations often provide useful information for the process control of a system. However, applying the control techniques on the physically-based model requires substantial computational effort. The detailed model is often reduced to a simpler model which sufficiently captures the majority of the dynamic characteristics. The lower-order dynamic model can be derived from a physically-based model to provide an initial consideration for process control. With the low-order model, a prerequisite for the controller design can be established in the development stage. A dynamic SOFC model offers a powerful tool for optimum design envelopes and control systems, bringing the SOFC technology one step closer to commercialization.

1.1 Status of Dynamic SOFC Modelling and Control

In SOFC research, broad areas of publication include material and catalyst development, performance improvement, integrated SOFC power systems, and computational modelling. Although, SOFC modelling activity has been accelerating in recent years, the majority of SOFC models does not address transient operation. Furthermore, control of fuel cells on a cell-level has received considerably less attention. In normal operations, SOFC are often subjected to transient condition such as changes in power demand. It is known that the

cell performance is significantly influenced by the mechanical properties of its components, which in turn rely heavily on temperature distribution along the cell. Frequent temperature changes triggered by transient operation often leads to excessive thermal stress and material degradation at both cell and stack levels. Concerns on thermal degradation and reliability during transient operations have been steadily increasing in SOFC technology development. Since the SOFC performance is sensitive to changes in operating conditions, consideration has been given to dynamic modelling and control of SOFC.

Generally, mathematical models of SOFC are derived from coupled partial differential equations describing the transport of charges, mass, momentum, and energy. Additionally, knowledge of thermodynamics and electrochemical kinetics are essential for model development. Earlier work on dynamic SOFC modelling was presented by Achenbach (1994, 1995) [5, 6]. The two-dimensional (2D) and three-dimensional (3D) dynamic models were used to investigate a stack-level dynamic responses, such as output voltage and temperature distribution during step changes in stack current. The model was repeated on different configurations to predict the optimal operating conditions. This work showed that the output voltage dynamics are strongly related to the temperature responses. A similar modelling effort was done by Hall and Colclaser (1999) [24]. The transient responses of the cell voltages and temperatures were obtained for tubular SOFC. Though the presented model did not account for mass transport effects, it provided a foundation for further detailed study.

Padullés et al. (2000) presented a stack-level dynamic SOFC model which showed transient responses of the stack voltage without considering the effects of temperature, mass transport, and other electrochemical losses [37]. Khaleel et al. (2001) developed a full 3D model based on computational fluid dynamics to represents the electrochemistry and heat transport in a stack [30]. This detailed model allowed for sensitivity studies on the cell performance with various operating parameters such as gas compositions, diffusion parameters, cell thicknesses, etc.

In the work by Haynes (2002), a dynamic model was developed for tubular SOFC [25]. From the dynamic responses to load changes, it was determined that dynamic time scales can be separated into three parts; electrochemical, electrical, and thermal time scales. The thermal time constant was observed to be significantly larger than the electrochemical and electrical time scales. The electrochemical model was presumed to be steady-state while the

electrical model was found to be dependent on mass transport.

The dynamic models of a standard tubular and a micro-tube SOFC were developed by Ota et al. (2003) [36]. It was found that the micro-tube had a faster response time to load changes than the standard tubular cell. The thermal inertia of SOFC had a large time constant, which was dependent on the scale size and geometry of the cell.

In the work of Qi et al. (2005), the dynamic SOFC behaviour at cell-level was modelled using a nonlinear state-space technique [40]. Sets of differential equations were derived using the combination of parallel and series equivalent circuit approach. The study determined that the gas diffusion mechanisms had a strong effect on the dynamic behaviour.

Most of the previously discussed dynamic models were used for prediction of SOFC performance and limitations. The majority of modelling efforts with process control considerations was presented for the integrated SOFC and turbine systems [48, 49]. The temperature control of a stack-level SOFC model was presented by Aguiar et al. (2005). A feedback PID controller was implemented in the developed model to maintain the outlet fuel temperature and the fuel utilization during load changes by varying the air flow rates [9]. The control objective was to minimize the thermal stress caused by temperature gradients during load changes. However, the importance of consistent output power demand usually took precedence over maintaining temperature gradients under a normal fuel cell operation. This also was suggested by Aguiar et al. that a voltage control must be implemented over the proposed temperature control loop in practical operation. In order to develop a comprehensive dynamic model to satisfy the control objective, suitable controlled parameters must be specified.

A dynamic model which extended its evaluation to thermal stress during transient operations was presented by Nakajo et al. (2006) [34]. The material stresses caused by thermal expansion mismatch between SOFC components during load changes were shown to be more severe than under steady-state operation. Although estimations of material thermal properties were uncertain, this model provided a helpful tool for the design of a less material stressed SOFC.

The dynamic models and control designs for other types of fuel cells have also been presented. In the work of Zenith and Skogestad (2004, 2005), the dynamic models of a proton exchange membrane fuel cell for use in electric vehicles were developed specifically

for control purposes [55, 56]. Their objective was to maintain the output voltage close to the reference voltage in the presence of load disturbances by using a converter to regulate the voltage. Although the dynamic model was simplified into an equivalent electrical circuit and the mass diffusion and temperature effects were not considered, it was justified that feedback control will likely compensate for minor modelling errors.

In many SOFC modelling activities, validation of the model results with experimental data is often overlooked. A validated model is an essential tool to accurately identify fuel cell characteristics and performance under specified operating conditions.

1.2 Research Objective

The majority of research activities in the dynamic modelling of SOFC with an interest on process control has focused on stack-level and the integrated-SOFC power plant system. It is evident that the dynamic behaviour of the SOFC stack is strongly influenced by an individual cell. The primary goal of this research is to develop a cell-level dynamic model that serves as a foundation for process control. The current work presents a three-dimensional (3D) dynamic model for control-design purposes. The model is capable of predicting the main steady-state properties of SOFC at various range of operating conditions. A physically-based dynamic SOFC model is developed to evaluate the cell performance and limitations under transient conditions. The mathematical model consists of coupled partial differential equations which describe the conservation of mass, momentum, energy, and charges. The steady-state modelling results are validated with published data from an existing experiment. To investigate transient characteristics of SOFC, the dynamic models are subjected to step changes in inlet gas concentrations and to external load disturbances. Simplified models capable of capturing the main dynamic characteristics of the system are derived and implemented in a feedback control simulation. An approach to control the output voltage such that it is close to the set-point voltage despite external load changes will be outlined.

1.3 Overview

The remainder of this thesis is organized as follows:

Chapter 2 presents an overview of fuel cell technology and their applications. Also discussed are SOFC principles, component materials, cell designs, and cell configurations. A review of the theoretical background in thermodynamics, electrochemistry, current-voltage characteristics, and the reactant utilization is also given in this chapter.

Chapter 3 provides the fundamentals of this work in regards to dynamic SOFC model development. A 3D model is developed for a counter-current flow planar SOFC configuration. Detailed transport equations derived from conservation laws of energy, mass, and charges are described in the form of partial differential equations (PDE). The coupled PDE representing the dynamic model are implemented and solved using COMSOL Multiphysics with a finite element method.

A significant portion of Chapter 4 includes modelling results. This chapter is divided into two parts: steady-state results, and dynamic responses. Steady-state simulation results are identified with experimental results from literature. The dynamic simulation results are determined from the step responses to system input and disturbance variables. The analysis of the dynamic behaviour is presented in this chapter.

Chapter 5 is devoted to investigating strategies to control the SOFC systems by maintaining SOFC output voltage despite load changes. From the dynamic responses, low-order dynamic models are derived and implemented in a feedback control scheme. The feedback controller responses are obtained and the limitations of the control system are investigated.

Chapter 6 presents the conclusion from this research, followed by suggestions and recommendations for future work.

Estimations of thermodynamic properties of SOFC and their gas constituents are given in Appendix A and B, respectively. Modelling parameters are given in Appendix C.

Chapter 2

Fuel Cell Overview

2.1 Introduction

Fuel cells utilize the principle of direct-energy conversion, i.e., the free energy change of an electrochemical reaction is converted directly to electrical energy. Generally, a fuel cell consists of positive (anode) and negative (cathode) electrodes separated by an electrolyte. A schematic diagram of a fuel cell is shown in Figure 2.1. Interconnect plates are installed to provide electrochemical contact between electrodes. Electrons travel between electrodes through an external load to complete the electrical circuit. Oxidant is reduced at the cathode and the mobile ion is transported through an electrolyte to the anode where fuel is oxidized. The fuel cell potential is obtained according to the energy change of the overall reaction.

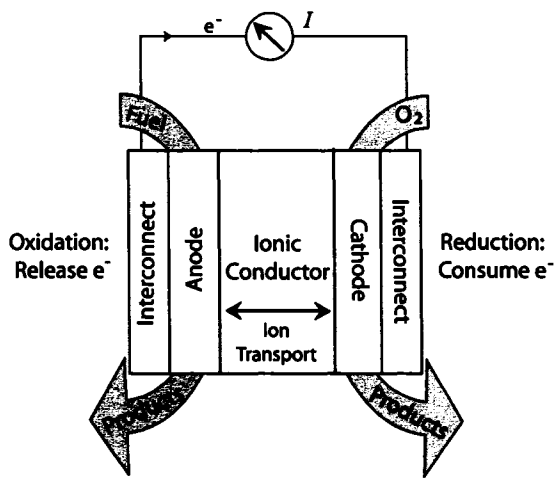

Figure 2.1: Schematic diagram of a fuel cell.

Electrical current is produced by an electrochemical process in a fuel cell, when an external load is applied. The electrical power generated by the fuel cell is equal to the product of the cell potential and the load current.

2.1.1 Fuel Cells Types

Types of fuel cells vary by their component materials, fuel types, and their operating conditions. Types of fuel cell currently available are

- Proton exchange membrane fuel cell (PEMFC) or solid polymer electrolyte fuel cell
- Direct Methanol Fuel Cells (DMFC)
- Alkaline fuel cell (AFC)
- Phosphoric acid fuel cell (PAFC)
- Molten carbonate fuel cell (MCFC)
- Solid oxide fuel cell (SOFC)

Each type of fuel cell requires different fuels and methods of fuel processing as illustrated in Figure 2.2.

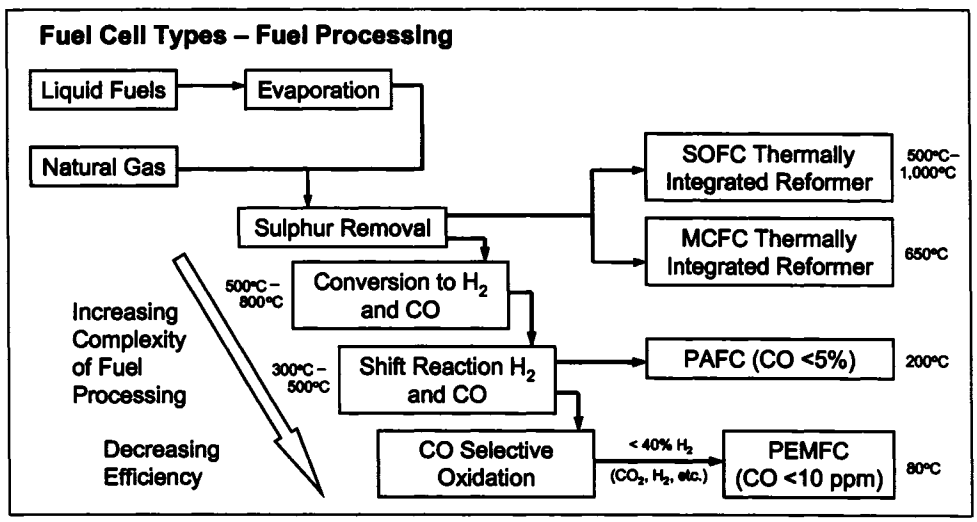

Figure 2.2: Fuel cell types and fuel processing overview [12].

Fuel cell materials, operating conditions and corresponding half cell reactions are summarized in Table 2.1. Due to differences in their size, fuel selectivity, and range of power generated, fuel cells are suitable for various applications as shown in Figure 2.3.

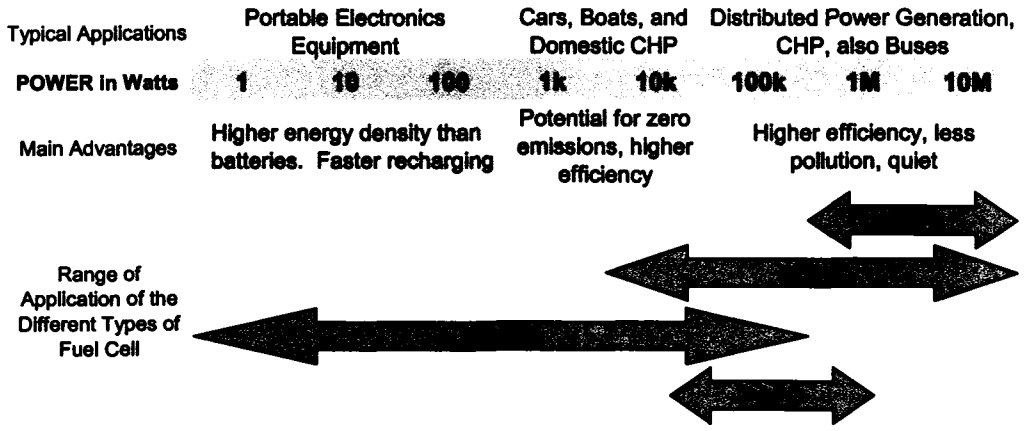

Figure 2.3: Application of Fuel cells [31].

2.1.2 Advantage and Disadvantage of Fuel Cells

Unlike heat engines, fuel cells are not limited by the Carnot cycle. The theoretical energy of the electrochemical reactions is converted directly to electrical energy. Hence, fuel cells provide the highest efficiency when connected to the lowest electrical loads [32]. Since fuel cells are scalable, they can be utilized in applications that require both low and high power outputs. Fuel cells deliver a quiet form of power generation that can be applicable in locations independent of the electrical grid. Depending on the fuel storage, their applications can be either modular or portable. Additionally, fuel cells are environmentally friendly since no NO_x or SO_x are produced.

The disadvantages of fuel cells include cost, fuel availability (in the case of hydrogen), familiarity and auxiliary services [12]. For high temperature fuel cells, the operating temperature places severe restriction on material selection and its fabrication process. There is ongoing research activity on alternative fuel cell materials to resolve this issue. These drawbacks must be overcome to make the commercialization of fuel cells possible.

In the present study, the modelling effort is focused on SOFC. These systems have been

Table 2.1: Type of fuel cells and their components, operating conditions, and reactions [12, 20].

	Low Temperature Fuel Cells			High Temperature Fuel Cells		
	PEMFC	DMFC	AFC	PAFC	MCFC	SOFC
Anode	Pt catalyst on carbon black	Pt, Ru catalyst	Ni catalyst	Pt catalyst on carbon bonded with PTFE[a]	Ni-Cr/Ni-Al	Ni-YSZ
Cathode	Pt catalyst on carbon black	Pt catalyst on carbon black	Li-doped NiO	100% H_3PO_4 in SiC matrix	Li-doped NiO in $LiAlO_2$ matrix	LSM
Electrolyte	Nafion®[b]	Nafion®	85 mol% KOH	Pt catalyst on carbon bonded with PTFE	62 mol% Li_2CO_3 - 38 mol% K_2CO_3	8 mol% YSZ
Absolute Pressure	1 atm	1 atm	2-44 atm	1 atm	1 atm	1 atm
Temperature	70°C-80°C	70°C-80°C	80°C-230°C	220°C	600°C-700°C	650°C-1,000°C
Mobile Ion	H^+	H^+	OH^-	H^+	CO_3^{2-}	O^{2-}
Anode Reaction	$2H_2 \rightarrow 4H^+ + 4e^-$	$2CH_3OH + 2H_2O \rightarrow 12H^+ + 12e^- + 2CO_2$	$2H_2 + 4OH^- \rightarrow 4H_2O + 4e^-$	$2H_2 \rightarrow 4H^+ + 4e^-$	$H_2 + CO_3^{2-} \rightarrow H_2O + CO_2 + 2e^-$	$H_2 + O^{2-} \rightarrow H_2O + 2e^-$
Cathode Reaction	$O_2 + 4e^- + 4H^+ \rightarrow 2H_2O$	$12e^- + 12H^+ + 3O_2 \rightarrow 6H_2O$	$O_2 + 4e^- + 2H_2O \rightarrow 4OH^-$	$O_2 + 4e^- + 4H^+ \rightarrow 2H_2O$	$O_2 + 2CO_2 + 4e^- \rightarrow 2CO_3^{2-}$	$O_2 + 4e^- \rightarrow 2O^{2-}$
Overall Reaction	$2H_2 + O_2 \rightarrow 2H_2O$	$2CH_3OH + 3O_2 \rightarrow 4H_2O + 2CO_2$	$2H_2 + O_2 \rightarrow 2H_2O$	$2H_2 + O_2 \rightarrow 2H_2O$	$2H_2 + O_2 \rightarrow 2H_2O$	$2H_2 + O_2 \rightarrow H_2O$

[a] Polytetrafluoroethylene

[b] Fluorinated sulfonic acid, registered trademark of E.I. du Pont de Nemours & Company, Inc. [20]

used in large scale power generation and distribution facilities. An advantageous application of SOFC are large scale manufacturing facilities which utilize energy integration to increase overall plant efficiency. In effect, a more competitive product can be manufactured. In recent years, SOFC have also been proposed in transportation applications. The modelling activities of SOFC significantly contributes to the performance improvement in many applications. In the following section, SOFC operating principles, component materials, and the current-voltage characteristics are discussed in detail.

2.2 Solid Oxide Fuel Cells

SOFC technology commences from the knowledge of ceramic conductors developed by Nernst in 1899. The first SOFC were fabricated by Baur and Pries in 1937 [45]. SOFC operates based on the principles that ionic oxides are transported through ceramic electrolyte. The operating principle of SOFC is illustrated in Figure 2.4.

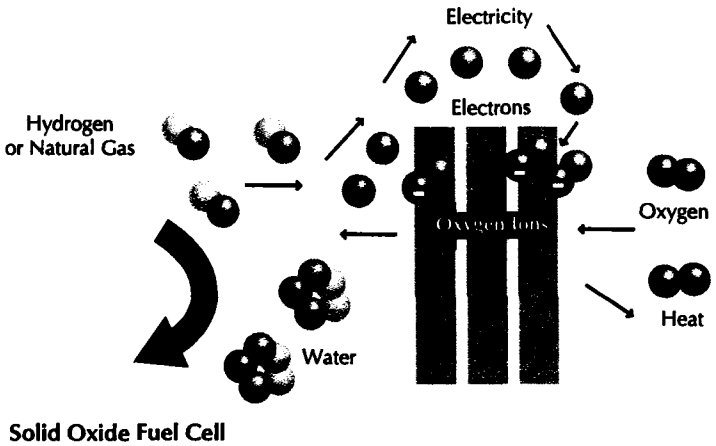

Figure 2.4: Solid oxide fuel cell Technology [13].

In principle, SOFC can be operated on any combustible fuel which can be oxidized to release oxide ion, O^{2-}. SOFC use solid electrolyte which alleviates corrosion problems that are normally experienced in liquid electrolyte fuel cells. SOFC are operated at elevated temperatures, usually between 600°C–1,000°C. High temperature operation promotes rapid reaction kinetics which increases the rate of oxide ion migration through the electrolyte. As a result, increased power generation can be achieved and high quality heat is released. This

waste heat can be recycled for used in SOFC power system such as running steam turbines or endothermic steam reforming reactions. In conventional SOFC where hydrogen is used as a fuel source, heat is emitted and water is the only reaction product. Hydrocarbons and carbon monoxide can also be directly used as fuels in SOFC. Due to their high temperature operations, internal reforming of hydrocarbon into hydrogen is feasible. Although hydrogen is generated directly, carbon dioxide is produced as an unavoidable by-product in the reforming process.

2.2.1 Cell Reactions

In SOFC, the oxygen ion (O^{2-}) is the mobile ion transferred through a solid ceramic electrolyte in the half cell reactions. Molecular oxygen from air is reduced to O^{2-} at the cathode according to the half cell reaction

$$\frac{1}{2}O_2 + 2e^- \leftrightarrow O^{2-} \tag{2.1}$$

The oxide anion diffuses through solid electrolyte to the anode. For hydrogen operating fuel cells, hydrogen fuel is oxidized by O^{2-} at the anode according to the reaction

$$H_2 + O^{2-} \leftrightarrow H_2O + 2e^- \tag{2.2}$$

Electrons from the anode migrate through the interconnect to the cathode, where molecular oxygen is reduced. The overall reaction is then

$$H_2 + \frac{1}{2}O_2 \rightarrow H_2O \tag{2.3}$$

A schematic diagram presenting the flow of mass and charges for SOFC is shown in Figure 2.5.

2.2.2 SOFC Component Materials

Electrolyte

The electrolyte is made from a dense material used to separate gas flow and promote electron migration between porous electrodes. High ionic conductivity and low electronic conductivity characteristics are essential properties which help facilitate O^{2-} transport. A ceramic

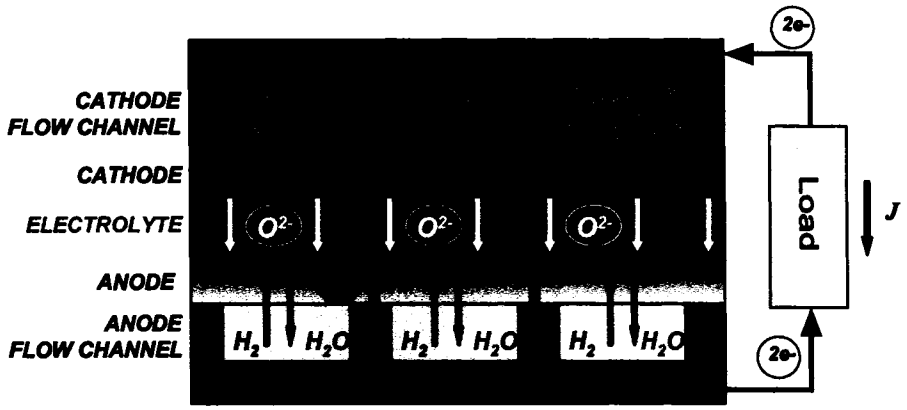

Figure 2.5: Schematic diagram of mass and charges flow in SOFC components.

material is often used since it has a stable microstructure which maintains good mechanical stability in oxidizing and reducing environments. Some of the electrolyte materials commonly used are yttria-stabilized zirconia (YSZ), gadolinium-doped ceria (GCO), strontium and magnesium doped lanthanum gallate (LSGM), and scandium-stabilized zirconia (ScSZ). Their conductivities, as a function of temperature, are shown in Figure 2.6 [27]. It can be seen in Figure 2.6 that higher operating temperatures promote higher ionic conductivity of the electrolyte.

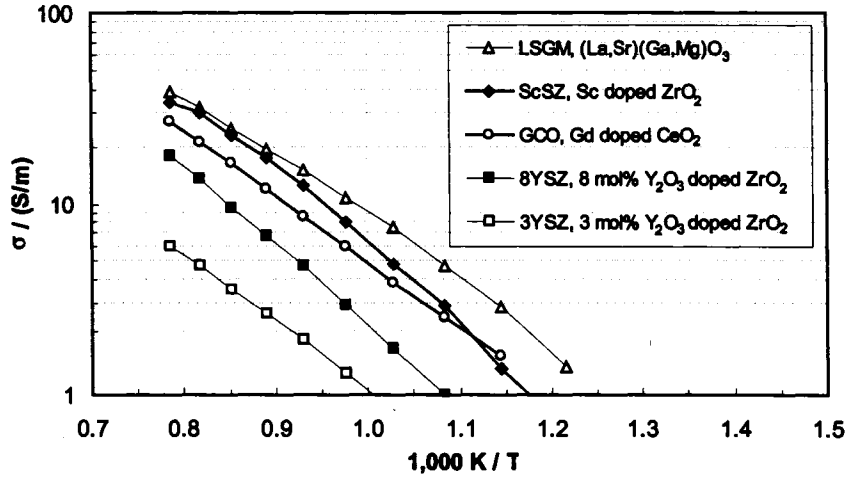

Figure 2.6: Ionic conductivity of various electrolyte materials as a function of dimensionless temperature [27].

Since oxygen partial pressure (P_{O_2}) can change from approximately 1 atm at the cathode to 1×10^{-20} atm at the anode, an ideal electrolyte must be stable over a wide range of P_{O_2} [23]. YSZ is the most commonly used ceramic material for SOFC electrolyte due to its mechanical advantages at high temperature (> 650°C). It is non-porous, non-reactive at high temperature, and stable over a wide range of pressure. YSZ also has a compatible thermal expansion property with other SOFC components [23]. Typically, 3 mol%–10 mol% of yttria (Y_2O_3) is doped onto stabilized zirconia (ZrO_2) to create vacancies for oxide ion, but 8 mol% YSZ (8YSZ) is most commonly seen. YSZ can be fabricated as a self-supported electrolyte layer with a thickness of 150 μm or greater. A thin YSZ layer of at least 10 μm can also be cast on a thick electrode layer to make an electrode-supported structure [12].

Three Phase Boundary The electrochemical reactions in Equation (2.1) and Equation (2.2) occur at the three-phase boundary (TPB) where the electrolyte, electrode and gas phase all come in contact. At the TPB site, the migration of oxygen ion to and from electrodes can be limited by the grain boundary resistance. It is reported that this limitation occurs mostly at the anode TPB [52]. This can be mitigated by extending the electrolyte material into the anode to facilitate ions, electrons and mass transfer at the reactive site. The location of anode TPB is shown in Figure 2.7.

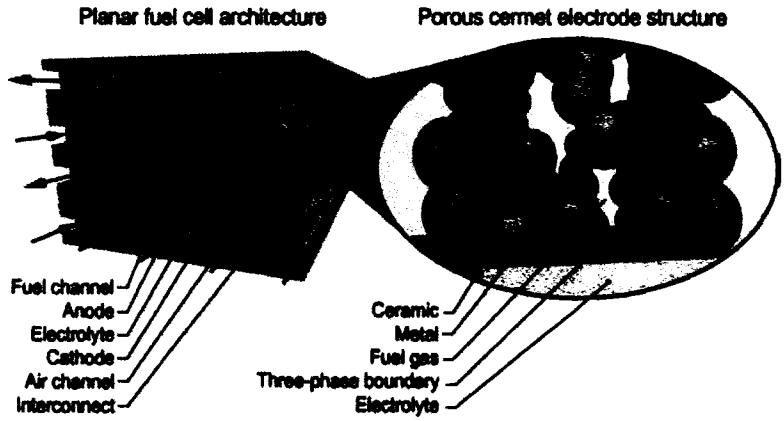

Figure 2.7: Three-phase boundary location [28].

Anode

An ideal anode material is electronically and ionically conductive. High anode porosity helps enhance diffusion of fuel gas to the three-phase boundary. A ceramic-metallic (cermet) combination of nickel (Ni) and 8YSZ is often used as anode material since Ni is an electron conductor whereas YSZ is an ion conductor. The cermet is stable in a reducing environment and is thermally compatible with the electrolyte material. Ni concentrations greater than 30 vol% are required for electronic conductivity greater than 1.0×10^4 S/m at 1,000°C [33].

Cathode

The cathode material must have high electronic and ionic conductivities. It must also be stable in an oxidizing environment and have a comparable thermal expansion property with the other materials. Porosity in the cathode promotes oxygen diffusion to the reactive sites. Strontium-doped lanthanum manganite (Sr-$LaMnO_3$ or LSM), lanthanum strontium ferrite (LSF) and lanthanum strontium cobalt iron oxide (LSCF) are typical cathode materials being used in recent development. LSM provides a good electronic conductivity of approximately 1.25×10^4 S/m at 1,000°C [33].

Interconnect

An ideal interconnect must be a good electronic conductor and an ionic insulator. Since the interconnect is in direct contact with air and fuel on each side, it has to be stable in both oxidizing and reducing environments and thermally compatible with the other components [46]. The interconnect is commonly made from metallic alloy ceramics. In early development, ceramics such as lanthanum-doped chromite ($LaCrO_3$) was used due to its excellent electronic conductivity. However, the fabrication of doped $LaCrO_3$ has been a challenge, leading to the development of other interconnect materials. Increasing use of metallic alloys and stainless steels has been observed in high temperature SOFC [12].

2.2.3 Design of a Single Cell

The design of SOFC can take on a variety of geometries unlike most other fuel cells. Although several designs have been developed, the two most common configurations of SOFC

are tubular and planar geometries. Each design brings about different advantages and disadvantages.

Tubular SOFC

In tubular SOFC design (Figure 2.8), a ceramic tube support is composed of electrodes and electrolytes. The tube serves as a gas passage where air flows in near the closed end of the tube. Fuel is introduced outside of the tube shell and oxidized while flowing to the open end. Tubular cell does not require seals with high heat integrity and can yield longer service time than planar SOFC. However, ohmic losses are comparatively higher, resulting in lower power density.

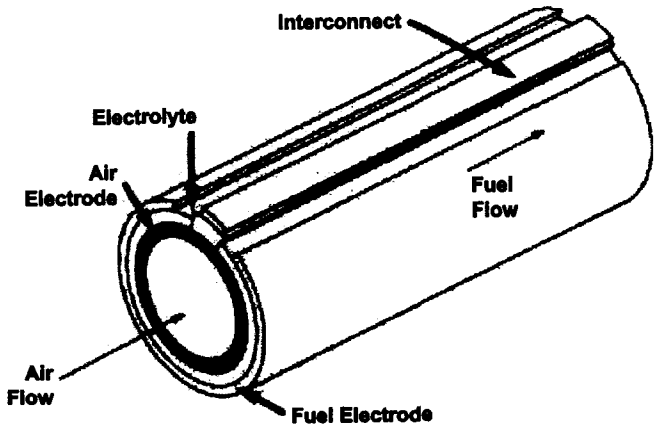

Figure 2.8: Siemens Westinghouse tubular SOFC design [46].

Planar SOFC

The planar SOFC designs are illustrated in Figure 2.9 and Figure 2.10. The interconnect forms gas-flow channels and acts as a bipolar plate contacting both electrodes. This configuration provides lower ohmic loss and higher power density based on a volumetric scale. It is also inexpensive to fabricate compared to the tubular design. However, sealing proves to be challenging in planar designs due to thermal expansion mismatch between components in the cell stack. Seals which reduce thermal stresses between cells have been developed to

mitigate this problem. The glass ceramic seals are often used for high temperature operation. For the operating temperature below 800°C, the compression gasket seals are used [31].

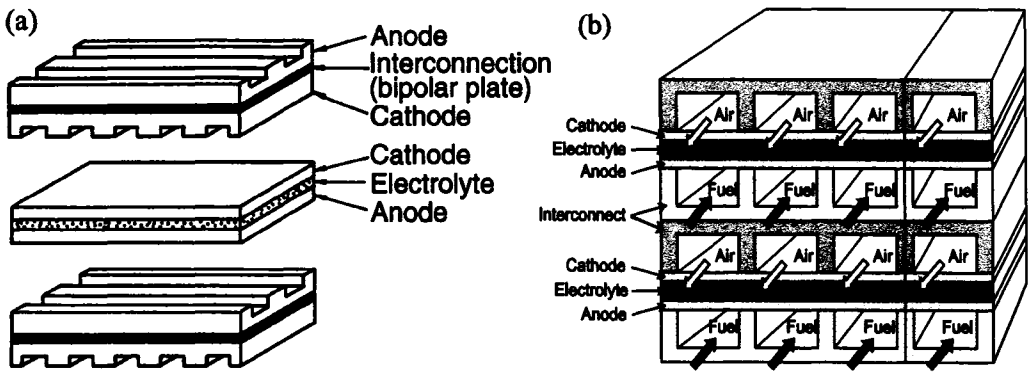

Figure 2.9: Planar SOFC cross-current flow (a) [46], and counter-current flow (b) design.

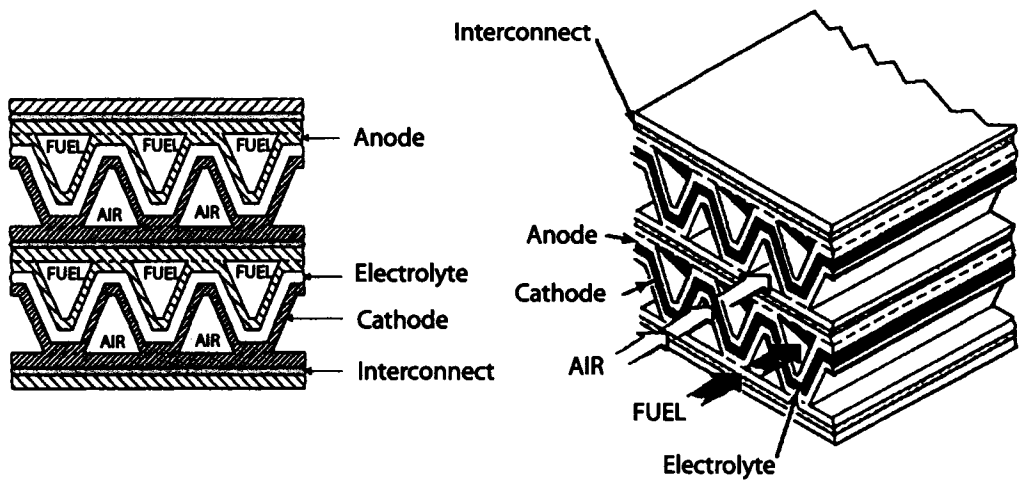

Figure 2.10: Planar SOFC co-current flow monolithic design [46, 33].

Various arrangements have been developed for planar SOFC. The cross-current flow and counter-current flow designs are shown in Figure 2.9 (a) and (b), respectively. A counter-current flow design provides high overall efficiency, where the cross-current flow yields high temperature gradients in the solid structure [5]. In a co-current flow monolithic design

(Figure 2.10), the fuel cell is composed of a ridged structure of electrodes and electrolyte composites. The monolithic design offers high power density, however the manufacturing process is challenging. The co-current flow arrangement, in general, provides the most uniform current density distribution [5].

Two common structures of planar SOFC are electrolyte-supported and anode-supported cells. In the electrolyte-supported planar SOFC, the thicknesses of the electrolyte and electrode layers are typically greater than 100 μm and 50 μm, respectively [1]. A thick layer of electrolyte promotes higher voltage drop as a result of high electrolyte resistance. Therefore, the electrode-supported cell is normally operated at temperatures above 900°C to obtain high electrical power. In the anode-supported SOFC, the thicknesses are typically 50 μm for the cathode, less than 20 μm for the electrolyte, and 300 μm–1500 μm for the anode. The electrolyte-supported and anode-supported planar designs are shown in Figure 2.11.

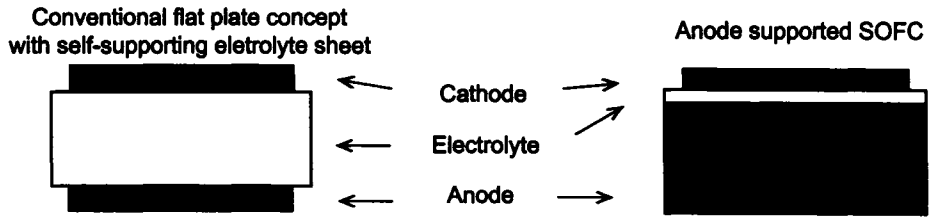

Figure 2.11: Electrolyte-supported and anode-supported planar SOFC [1].

Figure 2.12 shows a planar SOFC from Versa Power [11]. The scanning electron microscopy (SEM) image of the electrode-electrolyte layers of the planar anode-supported SOFC is presented in Figure 2.13. The cathode, electrolyte, and anode materials are 50-μm LSM, 5-μm 8YSZ, and 1-mm Ni/YSZ, respectively.

Figure 2.12: Planar solid oxide fuel cell [11].

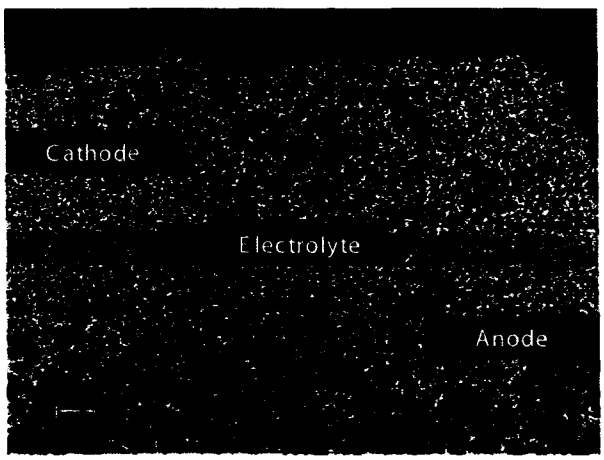

Figure 2.13: SEM cross section image of a planar solid oxide fuel cell [11].

2.3 SOFC Performance

The effects of operating conditions (e.g., temperature, pressure, and gas concentrations) contribute to the overall performance of fuel cell. Understanding how these factors thermodynamically affect the cell performance is essential to SOFC development. It is necessary to determine the ideal performance and various potential losses that contribute to the terminal voltage under load condition. In order to optimize the design and operating conditions of SOFC, the effect of chemical thermodynamics and electrochemical kinetics on the voltage-current relationships must be understood.

2.3.1 Thermodynamics of Solid Oxide Fuel Cells

In a hydrogen-oxygen fuel cell, the change in Gibbs free energy is dependent on the partial pressure of the reactants and products. For the overall chemical reaction in Equation (2.3), the change in Gibbs free energy, $\Delta G(T)$, can be expressed as

$$\Delta G(T) = \Delta G^{\circ}(T) + RT \ln \left(\frac{P_{H_2O}}{P_{H_2} P_{O_2}^{\frac{1}{2}}} \right) \tag{2.4}$$

where $\Delta G^{\circ}(T)$ is the Gibbs free energy change of the standard reaction at temperature T where the reactants and product are at the standard state pressure, P° = 0.1 MPa or 1 bar. The SOFC electrical potential is directly proportional to the maximum work for an electron to travel from the anode to the cathode. The electrochemical work, W_e, is expressed as

$$W_e = n_e F E(T) \tag{2.5}$$

where n_e is the number of electrons transferred through the cell electrode, F is the number of charges carried by a single mole of electron or the Faraday's constant. $E(T)$ is the electrical potential across the electrodes, which is a function of temperature. The value of W_e in fuel cells depends on the intrinsic nature of gaseous species, their concentrations, and the operating temperature.

At equilibrium, the change in Gibbs free energy is equal to the negative of the electrochemical work

$$\Delta G(T) = -n_e F E(T) \tag{2.6}$$

For the overall reaction in Equation (2.3), two electrons are transferred, thus $n_e = 2$. By substituting the change in Gibbs energy from Equation (2.6) into Equation (2.4), the Nernst voltage can be obtained.

$$E(T) = E^{\circ}(T) - \frac{RT}{2F} \ln \left(\frac{P_{H_2O}}{P_{H_2} P_{O_2}^{\frac{1}{2}}} \right) \tag{2.7}$$

Here $E^{\circ}(T)$ is the standard electrode potential for the overall reaction at specified fuel cell temperature. The value of $E^{\circ}(T)$ represents the theoretical no-loss voltage which is generally lower at higher temperatures. For a typical hydrogen SOFC operation at 800°C and 0.1 MPa, the standard electrode potential, E°, is approximately 0.98 V [16]. The value of E° at various temperature can be found in Appendix A.

2.3.2 Equilibrium Potential

The potential across the electrodes, $E(T)$ corresponds to the thermodynamically reversible open circuit voltage, V_{OCV}, which is the theoretical maximum work provided by the system. The V_{OCV} is equivalent to the equilibrium potential at which no current flows in the system. Here, the potential difference between the electrodes contributes to V_{OCV} in a relationship

$$V_{OCV} = V_{OCV,C} - V_{OCV,A} \tag{2.8}$$

where the equilibrium potential at the cathode and anode are

$$V_{OCV,C} = \frac{RT}{2F} \ln \left(P_{O_2}^{\frac{1}{2}} \right) \tag{2.9}$$

$$V_{OCV,A} = -E^{\circ}(T) + \frac{RT}{2F} \ln \left(\frac{P_{H_2O}}{P_{H_2}} \right) \tag{2.10}$$

At a the same temperature, the open circuit voltage does not exceed the theoretical potential ($E^{\circ} \geq V_{OCV}$). However, the open circuit voltage is usually closer to the theoretical potential at higher operating temperature [31].

2.3.3 Voltage and Overpotentials

The overall voltage of a SOFC is equal to the ideal voltage less the losses which account for non-equilibrium potential, mass transport limitation, and ohmic resistance.

$$V_{cell} = V_{OCV} - \sum |\eta_{act}| - \sum |\eta_{conc}| - JR_{\Omega} \tag{2.11}$$

Here, η_{act} is the activation overpotential, which represents the working electrode potential relative to a reference electrode. The concentration overpotential, η_{conc}, accounts for the voltage loss due to gas diffusion limitation at the reactive TPB sites near the electrode-electrolyte interface. The last term of Equation (2.11) represents the ohmic loss through ionic and electronic resistances of the cell (R_{Ω}) where J is the total current density.

The activation potential is the difference between electronic potential at the electrode and ionic potential at the electrolyte over the equilibrium potential. It contributes to the kinetic limitations of the electrode reactions occurring at the electrode-electrolyte interfaces, with larger overpotential loss leading to slower electrode kinetics.

$$\eta_{act,C} = (V_{el,C} - V_{io,C}) - V_{OCV,C} \tag{2.12}$$

$$\eta_{act,A} = (V_{el,A} - V_{io,A}) - V_{OCV,A} \tag{2.13}$$

Here, $V_{io,C}$ and $V_{io,A}$ are the ionic potentials at the electrolyte interfacing with the cathode and the anode, respectively. In a hydrogen-oxygen operating fuel cell with LSM cathode and Ni/YSZ anode, the activation overpotential is positive at the anode and negative at the cathode [17]. The activation loss at the cathode is also known to be larger than that at the anode for this cell type [51]. The electrochemical kinetics are less favourable at the cathode since a more significant overpotential is required for the reduction of oxygen than the oxidation of hydrogen.

The local voltages $V_{el,C}$ and $V_{el,A}$ can be calculated from the activation overpotentials as expressed in Equation (2.12) and (2.13). The overall cell voltage can be measured from the potential difference between the cathode and anode.

$$V_{cell} = V_{el,C} - V_{el,A} \tag{2.14}$$

Figure 2.14 illustrates the theoretical relationship between the local ionic and electronic potentials in Equation (2.12) through Equation (2.14). However, the constant equilibrium

potentials (V_{OCV}) as observed in Figure 2.14 do not precisely represent the maximum no-loss potentials in an operating fuel cell. The irreversible potential remains constant as long as there is no change in the cell temperature and the gas partial pressure at the reactive sites. Practically, this is not the case when mass diffusion limitation and temperature difference are present in the porous electrodes. With increasing current density, the mass and heat effects in the electrodes typically contributes to lower irreversible potentials.

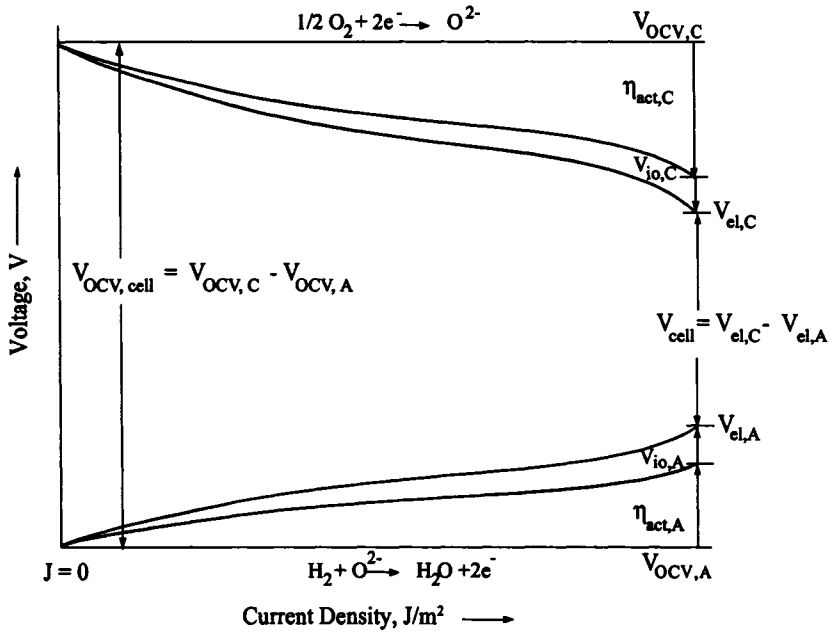

Figure 2.14: Current-voltage relationship in local electrodes.

2.3.4 Electrochemical Kinetics

The kinetics of electrochemical reaction are reflected by the activation overpotentials at the electrode-electrolyte boundaries. The amount of current density, J, being drawn from the interface is related to the activation overpotential as described by the Butler-Volmer equation.

$$J = J_o \left[\exp\left(\alpha_A \frac{F}{RT} \eta_{act}\right) - \exp\left(-\alpha_C \frac{F}{RT} \eta_{act}\right) \right] \tag{2.15}$$

Here, J_o is the exchange current density, α_A and α_C are the apparent charge transfer coefficients. By convention, the activation overpotential is negative at the cathode and positive at

the anode. Consequently, the current densities are negative at the cathode and positive at the anode. When $\eta_{act} = 0$, the anodic and cathodic current densities are equal to the exchange current densities, $J_{o,A}$ and $J_{o,C}$. The exchange current density is normally related to the partial pressure of gaseous species at the electrode-electrolyte interface where half-cell reaction takes place [19].

$$J_{o,A} = \gamma_A \left(\frac{P_{H_2}}{P_{ref}}\right)\left(\frac{P_{H_2O}}{P_{ref}}\right) \exp\left(-\frac{E_{act,A}}{RT}\right) \tag{2.16}$$

$$J_{o,C} = \gamma_C \left(\frac{P_{O_2}}{P_{ref}}\right)^{0.25} \exp\left(-\frac{E_{act,C}}{RT}\right) \tag{2.17}$$

Here, γ_C and γ_A are the pre-exponential coefficients. $E_{act,C}$ and $E_{act,A}$ represent the activation energies of the cathode and anode exchange current densities (J/mol), respectively.

The overall cell voltage as a function of current density is shown in Figure 2.15. It is observed that different types of transport limitations determine the shape of the current-voltage curve at various ranges of current density. The electrochemical reaction kinetics, which depend on the exchange current density and the Butler-Volmer parameters, predominantly affect the rate of voltage drop in the low current region. For a fuel cell with fast kinetics, a sharp drop of the cell voltage is observed when the current is being drawn in this region. For the high current region, the mass diffusion limitation results in a faster drop of the cell voltage. The electrolyte conductivity contributes more significantly to the cell voltage in the mid current region. By increasing the conductivity, a higher cell voltage can be attained as a result of Ohm's Law.

2.3.5 Reactant Utilization

From the Nernst equation, it can be seen that a higher open circuit potential is obtained by increasing the concentration of fuel cell reactants. The reactant consumptions also have a strong effect on the cell performance since it is dependent on the power demand. Under practical operations, not all reactants that enter the fuel cell are consumed in the electrochemical reactions. To determined the required amount of reactants, the coefficients of utilization are introduced.

The fuel utilization (FU) refers to the percentage of fuel consumed in the electrochemical reaction at the anode with respect to the total fuel introduced to the system. For a hydrogen

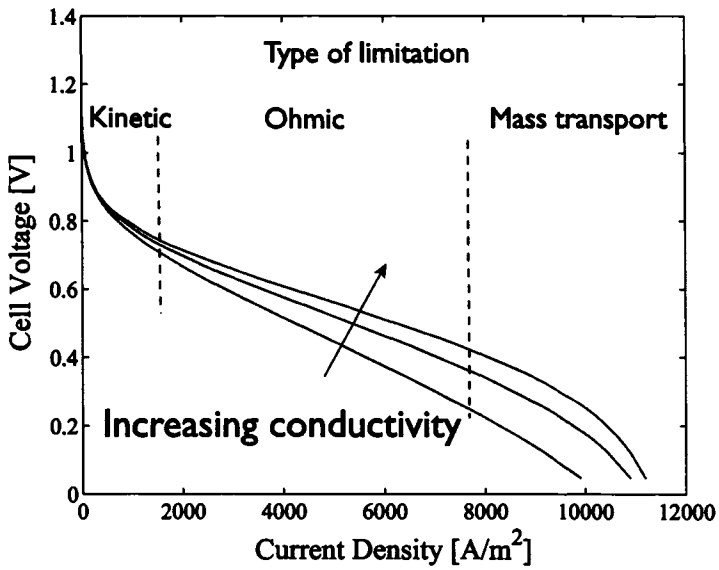

Figure 2.15: Cell voltage and its limitations with respect to the current density [3].

fuel cell, the fuel utilization is calculated directly from the inlet and the outlet mass flow rates of hydrogen.

$$\mathrm{FU} = \frac{\dot{m}_{\mathrm{H_2},in} - \dot{m}_{\mathrm{H_2},out}}{\dot{m}_{\mathrm{H_2},in}} \tag{2.18}$$

Here, $\dot{m}$ is the mass flow rate in kg/s. Similarly, the oxygen or air utilization (AU) can be calculated from

$$\mathrm{AU} = \frac{\dot{m}_{\mathrm{O_2},in} - \dot{m}_{\mathrm{O_2},out}}{\dot{m}_{\mathrm{O_2},in}} \tag{2.19}$$

Theoretically, the amount of fuel reacted in the anodic reaction is directly proportional to the total current density, J_A, being produced over the reactive surface area, A.

$$\dot{m}_{\mathrm{fuel}_{in}} - \dot{m}_{\mathrm{fuel}_{out}} = \left(\frac{\pm a}{n_e F} J_A A\right) MW_{\mathrm{fuel}} \tag{2.20}$$

Here, a and MW is the stoichiometric coefficient and the molecular weight of the fuel in the anode reaction. The amount of hydrogen consumed in the electrochemical reaction can be calculated from

$$\dot{m}_{\mathrm{H_2},in} - \dot{m}_{\mathrm{H_2},out} = \left(\frac{1}{2F} J_A A\right) MW_{\mathrm{H_2}} \tag{2.21}$$

Therefore, the hydrogen utilization is described as

$$\mathrm{FU} = \frac{1}{2F} \frac{(J_A A)}{\dot{m}_{\mathrm{H_2},in}} MW_{\mathrm{H_2}} \tag{2.22}$$

and the air utilization can be determined from

$$\mathrm{AU} = \frac{1}{4F}\frac{(J_C A)}{\dot{m}_{O_2,in}} MW_{O_2} \tag{2.23}$$

The reactant utilizations increase with increasing current density. If the reactants are limited, the power demand from an external load can only be increased to a point where the reactant utilizations reach the maximum. However, a complete utilization can hardly be achieved in a fuel cell due to the gas diffusion limitation. This limitation is especially more prominent at high current density where the demands of reactants in the electrochemical reactions exceed the mass diffusion rate. When reactant utilizations approaches 100%, the corresponding current is known as the limiting current density.

A SOFC performance curve showing breakdown of the relative potential losses and the power density is shown in Figure 2.16. It can be seen that the power density increases with increasing current density up to a maximum where a precipitous drop in voltage occurs due to mass transport limitation. It is important to operate the SOFC in the region which exhibits high voltage and power density when a maximum performance is required.

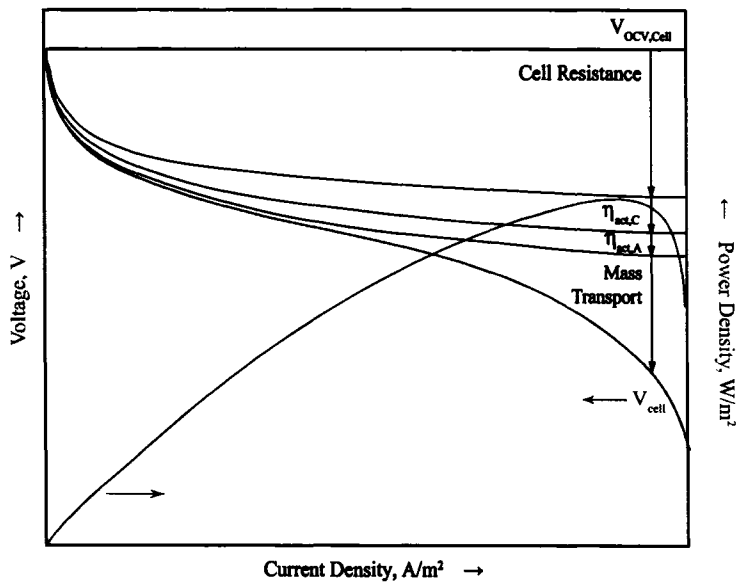

Figure 2.16: Overall fuel cell performance showing the relative voltage losses.

Chapter 3

Dynamic Model Development

3.1 Introduction

A computational model of SOFC is derived from coupled partial differential equations which represent conservation laws of charges, mass, momentum, and energy. The background of fundamental thermodynamics and electrochemical kinetics introduced in Chapter 2 is incorporated in the dynamic model development. This chapter presents detailed transport equations for a 3D SOFC model configuration. The numerical model is constructed for an anode-supported planar SOFC with a counter-current flow configuration. The chapter is divided into four parts: modelling assumptions, modelling geometry, transport equations, and mesh generation including solver settings. The solutions to the physically-based dynamic model are solved using COMSOL Multiphysics with finite element method [4].

3.2 Modelling Assumptions

Assumptions made in this study are

1. The model is a three-dimensional and is a function of x, y, and z coordinates of a anode-supported counter-current flow planar SOFC.
2. Dynamic conditions are applied for all transports except for the electronic and ionic charge transports.
3. The cathode, anode, and electrolyte materials are LSM, Ni/YSZ composite, and 8

mol% YSZ, respectively. The interconnects are metal alloys. The material mechanical properties used in the model are selected accordingly.

4. The electrochemical reactions are assumed to occur at the electrode-electrolyte boundaries.

5. Ideal gas conditions are assumed for high temperature and moderate pressure operating condition.

6. Hydrogen, water, and nitrogen are considered anodic reactants. Air is the cathodic reactant. Nitrogen acts as an inert gas and does not participate in the electrochemical reactions.

7. Bulk (molecule-to-molecule) diffusion predominates in the gas channels. Knudsen (molecule-to-wall) diffusion contributes to mass transport in the porous electrodes. Although diffusion occurs in both the electrodes and the flow channels, mass transport in the gas channels is convection-dominated.

8. All gas streams are preheated with uniform temperatures and uniform gas velocities as they enter the gas channels. The rest of the outer fuel cell boundaries are assumed to be thermally insulated.

9. The density and heat capacity of gases and solid structures are temperature independent.

10. In the gas channels, the heat transfer is convection-dominated, while it is conduction-dominated in the solid phase. Convective heat transfer is negligible in the porous electrodes.

3.3 Modelling Geometry

The modelling geometry is an anode-supported planar SOFC. The counter-current flow direction of air and fuel is specified. The schematic diagram of a planar SOFC in this study is shown in Figure 3.1. For a 10-channel cell, the cell length, L, and the width, W, are 19 mm and 20 mm, respectively. The overall cell area is 3.8 cm^2.

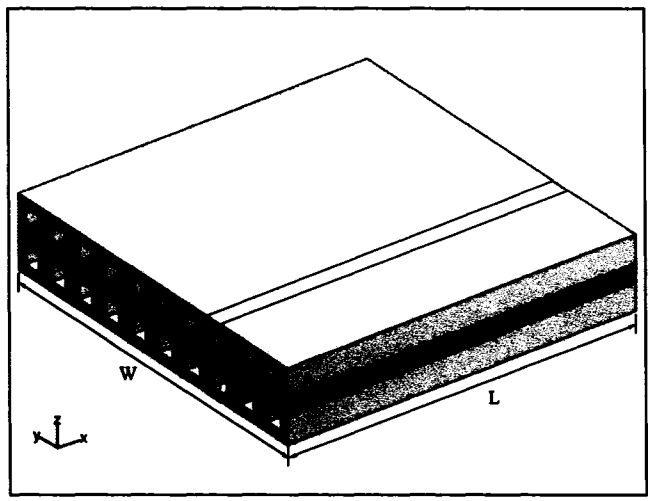

Figure 3.1: Schematic diagram of an anode-supported planar SOFC.

Due to geometric symmetry of the planar SOFC in Figure 3.1, the computational domain is reduced to a half-channel geometry as shown in Figure 3.2. The dimension of the modelling domain can be found in Table 3.1.

3.4 Transport Equations

Formulation of the transport equations are required to model the SOFC potentials, species concentrations, flow profiles, and temperature gradients in the proposed geometry. In this section, the conservation laws of each transport are derived in the form of partial differential equations. The electronic and ionic charge transports are instantaneous phenomena which are assumed to be in steady-state [25]. The mass, momentum, and heat transports occur on a larger time scale and their dynamic behaviours are accounted for. These mathematical equations are implemented in the applicable modelling subdomains. The boundary conditions required to solve the transport equations are imposed at the applicable boundaries. Method for estimating the gas mixture properties used in the model are provided in Appendix B. SOFC physical properties and other modelling parameters can be found in Appendix C.

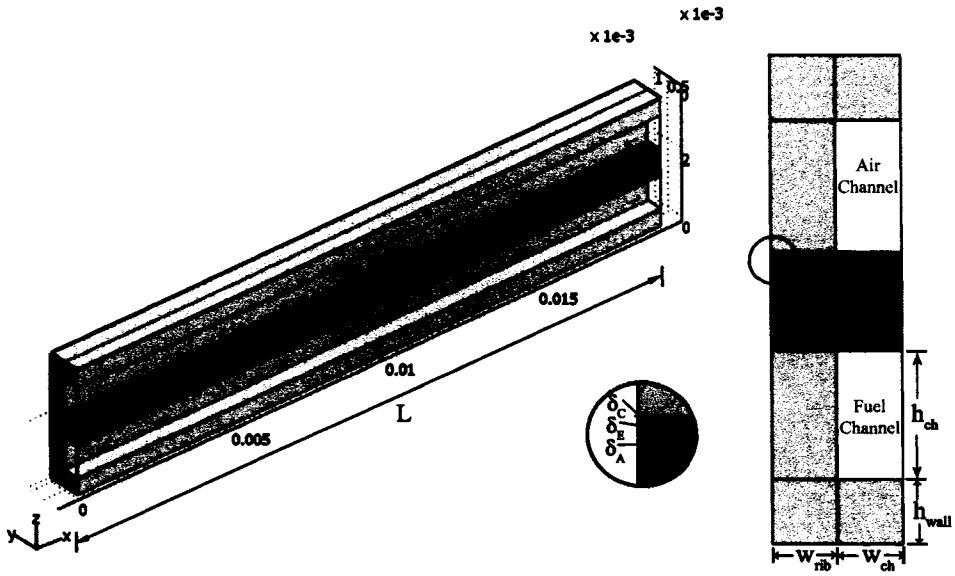

Figure 3.2: SOFC modelling domain.

3.4.1 Ionic Charge Transport

The equation of continuity for an ionic charge (O^{2-}) can be expressed as

$$\frac{\partial}{\partial t}(\rho_{io}) = -(\nabla \cdot \mathbf{J}_{io}) + \hat{S}_{io} \tag{3.1}$$

where ρ_{io} is the ionic charge density (C/m^3), J_{io} is the ionic current density (A/m^2), and $\hat{S}_{io}$ is the ionic current source (A/m^3). Since it is assumed that the current balance is at steady-state, the transient term can be dropped from Equation (3.1) [3]. There is no production or consumption of the ionic charge in the modelling domain since the electrochemical reactions only occur at the electrode-electrolyte boundaries. Therefore, the ionic current source, $\hat{S}_{io}$, is zero.

The current density J_{io} is described by Ohm's law,

$$\mathbf{J}_{io} = \sigma_{io}\mathbf{E}_{io} \tag{3.2}$$

where σ_{io} is the ionic conductivity in S/m. $\mathbf{E}_{io}$ is the ionic potential field, which is equal to the negative of the potential gradient.

$$\mathbf{E}_{io} = -\nabla V_{io} \tag{3.3}$$

Table 3.1: Dimension of solid oxide fuel cell modelling domain.

Parameter	Length	Unit
Gas channel height, h_{ch}	1.0	mm
Gas channel width, w_{ch}	0.5	mm
Top and bottom wall height, h_{wall}	0.5	mm
Rib width, w_{rib}	0.5	mm
Cathode layer thickness, δ_C	50	μm
Electrolyte layer thickness, δ_E	10	μm
Anode layer thickness, δ_A	700	μm
Fuel cell length, L	19	mm
Active surface area, A	19	mm^2

Substituting Equation (3.3) into Equation (3.2) yields

$$\mathbf{J}_{io} = -\sigma_{io}\nabla V_{io} \tag{3.4}$$

By substituting Equation (3.4) into Equation (3.1) and omitting the transient term, the charge balance equation is obtained.

$$-\nabla \cdot (\sigma_{io}\nabla V_{io}) = 0 \tag{3.5}$$

Subdomain Equation

The ionic charge of oxygen is present in the electrolyte layer. The ionic charge transport equation applies to the electrolyte domain as shown in Figure 3.3. The transport of ions through the electrolyte can be described as

$$-\nabla \cdot (\sigma_{io,E}\nabla V_{io}) = 0 \tag{3.6}$$

The ionic conductivity of YSZ electrolyte ($\sigma_{io,E}$) is temperature dependent and is given by [21]

$$\sigma_{io,E} = 3.34 \times 10^4 \exp\left(-\frac{10,300}{T}\right) \tag{3.7}$$

Boundary Condition

At the cathode-electrolyte boundary, the ionic current flows outward from the electrolyte to the cathode (see Figure 3.3). The normal ionic current density is equal to the current density

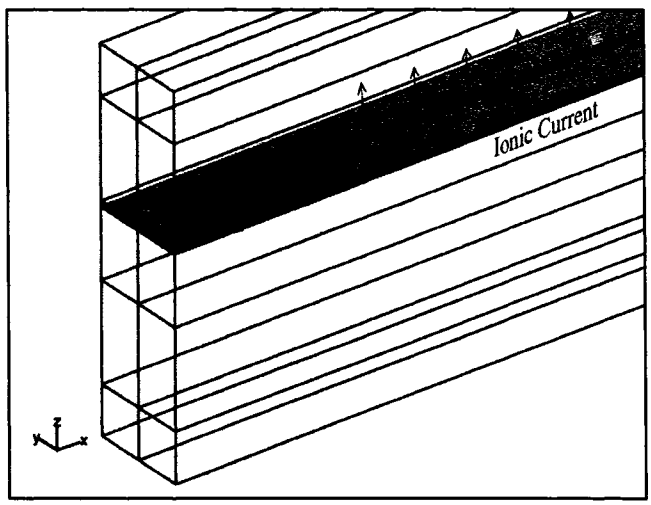

Figure 3.3: Applicable domain for ionic charge transport. The arrows indicate the direction of ionic current flow.

generated according to the Butler-Volmer equation.

$$-\mathbf{n} \cdot \mathbf{J}_{io} = -J_C \tag{3.8}$$

At the anode-electrolyte boundary, the normal ionic current density flowing from the anode into the electrolyte is given by

$$-\mathbf{n} \cdot \mathbf{J}_{io} = J_A \tag{3.9}$$

J_C and J_A are the current densities obtained from the Butler-Volmer expression (Equation (3.10) and Equation (3.11) in Chapter 2). According to Costamagna and Honegger (1998), the current density at the two electrode-electrolyte interfaces takes the forms [19]

$$J_C = J_{o,C}\left[\exp\left(1.4\frac{F}{RT}\eta_{act,C}\right) - \exp\left(-0.6\frac{F}{RT}\eta_{act,C}\right)\right] \tag{3.10}$$

$$J_A = J_{o,A}\left[\exp\left(2.0\frac{F}{RT}\eta_{act,A}\right) - \exp\left(-1.0\frac{F}{RT}\eta_{act,A}\right)\right] \tag{3.11}$$

The exchange current densities $J_{o,A}$ and $J_{o,C}$ used in the current flow model are given by

$$J_{o,A} = 7.55 \times 10^9 \left(\frac{P_{H_2}}{P_{ref}}\right)\left(\frac{P_{H_2O}}{P_{ref}}\right)\exp\left(-\frac{120 \times 10^3}{RT}\right) \tag{3.12}$$

$$J_{o,C} = 9.61 \times 10^8 \left(\frac{P_{O_2}}{P_{ref}}\right)^{0.25} \exp\left(-\frac{110 \times 10^3}{RT}\right) \tag{3.13}$$

For the other boundaries where no ionic charge are transferred, an ionic charge insulation is specified.

$$-\mathbf{n} \cdot \mathbf{J}_{io} = 0 \tag{3.14}$$

This boundary condition indicates that no ionic current components are perpendicular to the boundaries.

3.4.2 Electronic Charge Transport

Modelling of the electron transport coupled with the ionic transport provides solution to the local potential losses in the electrolyte, electrodes, and interconnects. The electronic charge transport is a steady-state analysis and the charge balance equation is similar to that of the Equation (3.1)

$$-\nabla \cdot (\sigma_{el} \nabla V_{el}) = 0 \tag{3.15}$$

where σ_{el} is the electronic conductivity of the electrodes (S/m). The schematic of charges flow at the ionic-electronic boundary layers is illustrated in Figure 3.4. At the electrodes and electrolyte interfaces, the current is coupled between the ionic and electronic charge balances.

$$\mathbf{J}_{el} = -\mathbf{J}_{io} \tag{3.16}$$

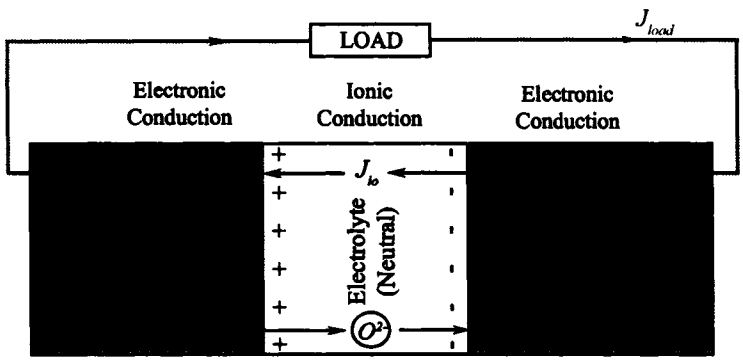

Figure 3.4: Ionic and electronic charges flow direction at the electrode-electrolyte boundaries

Subdomain Equation

The electronic charge transport equation applies to both electrodes and the interconnects. Figure 3.5 illustrates the modelling domain where the electronic charge equations are implemented. The applied equations for electronic charge balance at the electrodes and their

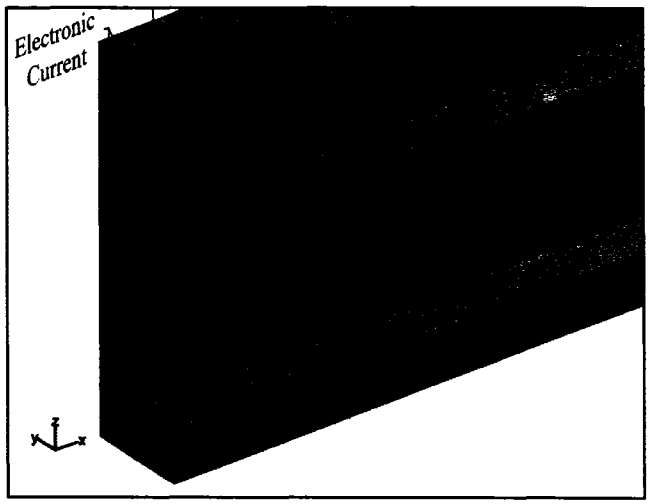

Figure 3.5: Applicable domains for electronic charge transport. The arrows indicate the direction of electronic current flow.

interconnects are as follows.

$$-\nabla \cdot (\sigma_{el,C} \nabla V_{el}) = 0 \tag{3.17}$$

$$-\nabla \cdot (\sigma_{el,CI} \nabla V_{el}) = 0 \tag{3.18}$$

$$-\nabla \cdot (\sigma_{el,A} \nabla V_{el}) = 0 \tag{3.19}$$

$$-\nabla \cdot (\sigma_{el,AI} \nabla V_{el}) = 0 \tag{3.20}$$

The electronic conductivities of the electrodes and their interconnects are temperature dependent and are given by [21]

$$\sigma_{el,C} = \frac{4.0 \times 10^7}{T} \exp\left(-\frac{1,200}{T}\right) \tag{3.21}$$

$$\sigma_{el,A} = \frac{9.0 \times 10^7}{T} \exp\left(-\frac{1,150}{T}\right) \tag{3.22}$$

The values of the electrode conductivity above conform to those reported in the literatures [19, 53, 22]. The electronic conductivity of the interconnect is 4×10^6 S/m, which agrees with the value reported by Costamagna and Honegger (1998) for an alloy metal current collector [19].

Boundary Condition

At the cathode-electrolyte boundary, the electronic current flows inward from the electrolyte to the cathode. The following current flow boundary condition is applied

$$-\mathbf{n} \cdot \mathbf{J}_{el} = J_C \tag{3.23}$$

At the anode-electrolyte boundary, the boundary condition is

$$-\mathbf{n} \cdot \mathbf{J}_{io} = -J_A \tag{3.24}$$

Again, J_C and J_A are the Butler-Volmer current densities. At the outer boundary of the cathode interconnect, the voltage is specified as a zero reference voltage.

$$V_{el} = 0 \tag{3.25}$$

At the anode interconnect boundary, the net current demanded by the external load resistance is specified.

$$-\mathbf{n} \cdot \mathbf{J}_{el} = -J_{load} \tag{3.26}$$

Insulated boundary condition is applied elsewhere including the axis of symmetry. This is to ensure that the electronic current components are perpendicular to the boundary.

$$-\mathbf{n} \cdot \mathbf{J}_{el} = 0 \tag{3.27}$$

3.4.3 Mass Transport

It is crucial to understand the mass transport mechanism in the porous electrodes since most of the electrochemical activities take place at the electrode-electrolyte boundaries. Although mass diffusion is dominated in the porous electrodes, convection can have a significant effect

in the flow channels. Since mass transport plays an important role in the concentration distribution at the reactive interfaces, a mass balance equation accounting for the diffusive and convective effects must be solved.

The continuity equation containing mass diffusive and convective fluxes are expressed as [3]

$$\frac{\partial}{\partial t}(\rho w_i) = -\nabla \cdot (\mathbf{j}_i + \rho w_i \mathbf{u}) + \hat{R}_i \tag{3.28}$$

where ρ is the density, w_i is the mass fraction, $\mathbf{j}_i$ is the mass flux, $\mathbf{u}$ is the gas velocity component, and $\hat{R}_i$ is the reaction rate or the mass source/sink term. Since the electrochemical reactions occur at the boundary, the mass consumption or production rate of gas species in the electrode, $\hat{R}_i$, is equal to zero. The fluid density can be calculated from the ideal gas law

$$\rho = \frac{P}{RT} MW_{ave} \tag{3.29}$$

where P is the total gas pressure, and MW_{ave} is the average molecular weight of the gas mixture.

The Maxwell-Stefan modelling equation is most commonly used in multi-component diffusion. Unlike Fick's diffusion which assumes that the solute gas only interacts with its solvent, the Maxwell-Stefan model accounts for molecule interactions between gas mixtures. The Maxwell-Stefan mass diffusive flux is described by

$$\mathbf{j}_i = -\rho w_i \sum_{k=1}^{N} \left[\tilde{D}_{ik} \left(\nabla x_k + (x_k - w_k) \frac{\nabla P}{P} \right) \right] \tag{3.30}$$

Here, N is the number of gaseous species present at the electrode, $\tilde{D}_{ik}$ is the multicomponent Fick diffusivity between species i and k. The symbols x_k and w_k represent the mole fraction and mass fraction, respectively. The general equation which applies to the mass transport in the gas channel becomes

$$\frac{\partial}{\partial t}(\rho w_i) = -\nabla \cdot \left[-\rho w_i \sum_{k=1}^{N} \left[\tilde{D}_{ik} \left(\nabla x_k + (x_k - w_k) \frac{\nabla P}{P} \right) \right] + \rho w_i \mathbf{u} \right] \tag{3.31}$$

The method of calculating the multicomponents Fick diffusivity from the Maxwell-Stefan diffusivities is readily implemented in the Maxwell-Stefan Diffusion and Convection application mode in COMSOL Multiphysics [3]. Since the density of gas mixture is relatively low in the hydrogen SOFC application, the Maxwell-Stefan diffusivities can be

approximated as the binary diffusivities for all pairs of gas species. From the Chapman-Enskog gas kinetic theory, the binary diffusivity is given as [10]

$$D_{ik} = \frac{(1.8583 \times 10^{-7})T^{1.5}}{P\hat{\sigma}_{ik}^2 \hat{\Omega}_{D,ik}} \left(\frac{1}{MW_i} + \frac{1}{MW_k}\right)^{0.5} \tag{3.32}$$

where $\hat{\sigma}_{ik}$ is the average collision diameter and $\hat{\Omega}_{D,ik}$ is the collision integral based on the Lennard-Jones potentials. The binary diffusivity has been evaluated as $D_{H_2-H_2O} = 7.16 \times 10^{-4}$ m^2/s, $D_{H_2-N_2} = 5.99 \times 10^{-4}$ m^2/s, and $D_{H_2O-N_2} = 2.03 \times 10^{-4}$ m^2/s for the anodic side at 1,023 K. The value $D_{O_2-N_2} = 1.67 \times 10^{-4}$ m^2/s is obtained at the cathode. These binary diffusivities are used to calculate the multi-component Fick diffusivities, $\tilde{D}_{ik}$, in COMSOL Multiphysics.

Diffusion mechanism in the porous electrode differs from that in the flow channel. In the porous electrode, the average pore size is considerably smaller than the gas particle's mean free path. The molecule-to-wall of gas particles collision will dominate the molecule-to-molecule collision. The Knudsen gas diffusion, which accounts for the molecule-to-wall collision, is incorporated in the mass transport model in the porous electrodes. According to the kinetic theory of gases, the Knudsen diffusivity coefficient depends on the mean molecular velocity of the gas, ν_i, colliding to the wall of a cylindrical pore with the mean pore radius, $\bar{r}_i$.

$$D_{K,i} = \frac{2}{3}\nu\bar{r}_i \tag{3.33}$$

The mean molecular velocity of a gas species in a mixture is given by

$$\nu_i = \sqrt{\frac{8RT}{\pi MW_i}} \tag{3.34}$$

Combining Equation (3.33) and Equation (3.34), the Knudsen diffusivity becomes

$$D_{K,i} = \frac{2}{3}\bar{r}_i\sqrt{\frac{8RT}{\pi MW_i}} \tag{3.35}$$

Combining the Knudsen diffusivity with the binary diffusivity, a modified diffusivity is obtained [26].

$$\frac{1}{\hat{D}_{ik}} = \frac{1}{D_{ik}} + \frac{1}{D_{K,i}} \tag{3.36}$$

$$\hat{D}_{ik} = \left(\frac{D_{ik}D_{K,i}}{D_{ik} + D_{K,i}}\right) \tag{3.37}$$

For mass transport in porous electrodes, the effective binary diffusivity depends on the material properties such as the porosity, tortuosity, and pore size. The effective diffusivity is often corrected by the ratio of the porosity to the tortuosity [51].

$$\hat{D}_{ik}^{eff} = \frac{\varepsilon}{\tau}\hat{D}_{ik} \tag{3.38}$$

where ε is the porosity and τ is the tortuosity factor. The tortuosity represents the ratio of the diffusion path and the mean free path in the porous materials. The effective multicomponent Fick diffusivity, $\tilde{D}^{eff}$ is calculated from the diffusivity given in Equation (3.38). The general mass transfer in the porous electrodes thus becomes

$$\frac{\partial}{\partial t}(\rho w_i) = -\nabla \cdot \left[-\rho w_i \sum_{k=1}^{N} \left[\tilde{D}_{ik}^{eff} \left(\nabla x_k + (x_k - w_k)\frac{\nabla P}{P} \right) \right] + \rho w_i \mathbf{u} \right] \tag{3.39}$$

At the electrode-electrolyte interfaces, the rate of the electrochemical reaction is related to the rate of current generation according to the Butler-Volmer expression. For example, the rate of production or consumption of species i at the anode-electrolyte boundary is expressed as

$$r_{i,A} = \left(\frac{\pm a}{n_e F} J_A \right) MW_i \tag{3.40}$$

where a is the stoichiometric coefficient, which has a negative and positive sign when the species i is being consumed and produced, respectively. Thus, the rate of hydrogen consumption at the anode is expressed as

$$r_{H_2} = \left(\frac{-1}{2F} J_A \right) MW_{H_2} \tag{3.41}$$

Subdomain Equation - Cathode and Air Channel

The governing equations for mass transport apply to the electrodes and their gas channels. The applicable modelling domains for mass transport of O_2 and N_2 in air are shown in Figure 3.6. At the porous cathode, oxygen and nitrogen are present ($N = 2$). The effective diffusivity is used in the governing equation.

$$\frac{\partial}{\partial t}(\rho w_{O_2}) + \nabla \cdot \left[-\rho w_{O_2} \sum_{k=1}^{2} \left[\tilde{D}_{O_2,k}^{eff} \left(\nabla x_k + (x_k - w_k)\frac{\nabla P}{P} \right) \right] + \rho w_{O_2} \mathbf{u} \right] = 0 \tag{3.42}$$

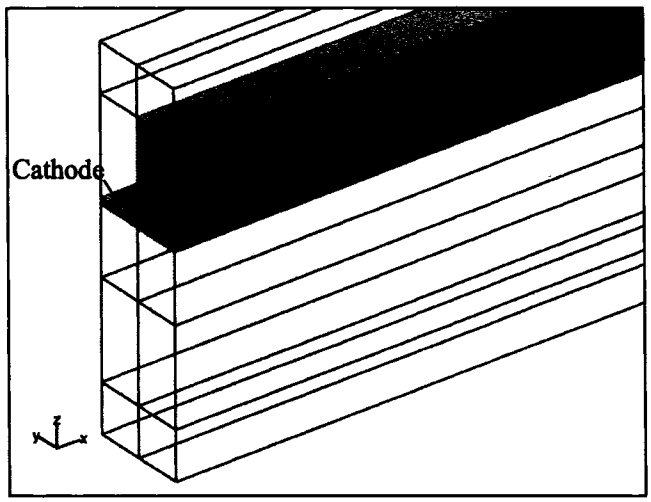

Figure 3.6: Applicable domains for mass transport (air).

In the air channel, the following equation applies

$$\frac{\partial}{\partial t}(\rho w_{O_2}) + \nabla \cdot \left[-\rho w_{O_2} \sum_{k=1}^{2} \left[\tilde{D}_{O_2,k} \left(\nabla x_k + (x_k - w_k) \frac{\nabla P}{P} \right) \right] + \rho w_{O_2} \mathbf{u} \right] = 0 \quad (3.43)$$

Since nitrogen does not partake in the electrode reaction, the mass fraction of nitrogen is calculated in all applicable domains by

$$w_{N_2} = 1 - w_{O_2} \quad (3.44)$$

Boundary Condition - Cathode and Air Channel

At the air channel inlet, a mass fraction is specified.

$$w_{O_2} = w_{O_2,in} \quad (3.45)$$

Since the mass transport in the gas channel is convection-dominated, the outlet concentration is not known. A convective flux boundary condition is specified at the air channel outlet. This boundary condition is based on the assumption that convective mass transport is

dominated in the gas channel and the diffusion flux component across this boundary will be zero.

$$-\mathbf{n}\cdot\left[-\rho w_{O_2}\sum_{k=1}^{2}\left[\tilde{D}_{O_2,k}\left(\nabla x_k+(x_k-w_k)\frac{\nabla P}{P}\right)\right]\right]=0 \tag{3.46}$$

At the cathode-electrolyte interface, oxygen is being consumed at the rate proportional to the cathodic current densities, J_C, given by the Butler-Volmer expression.

$$-\mathbf{n}\cdot\left[-\rho w_{O_2}\sum_{k=1}^{2}\left[\tilde{D}^{eff}_{O_2,k}\left(\nabla x_k+(x_k-w_k)\frac{\nabla P}{P}\right)\right]+\rho w_{O_2}\mathbf{u}\right]=-\frac{J_C}{4F}MW_{O_2} \tag{3.47}$$

Since no mass flux of air is leaving the domain through the remaining boundary, the following boundary condition is applied.

$$-\mathbf{n}\cdot\left[-\rho w_{O_2}\sum_{k=1}^{2}\left[\tilde{D}_{O_2,k}\left(\nabla x_k+(x_k-w_k)\frac{\nabla P}{P}\right)\right]+\rho w_{O_2}\mathbf{u}\right]=0 \tag{3.48}$$

This boundary condition is also known as the insulation/symmetry condition.

Subdomain Equation - Anode and Fuel Channel

The applicable modelling domains for mass transport of fuel are shown in Figure 3.7. Three gas constituents are present in the anode and fuel channel ($N = 3$); hydrogen, water, and nitrogen. The mass transport equations are similar to those of the cathode and the air channel. At the anode:

$$\frac{\partial}{\partial t}(\rho w_{H_2})+\nabla\cdot\left[-\rho w_{H_2}\sum_{k=1}^{3}\left[\tilde{D}^{eff}_{H_2,k}\left(\nabla x_k+(x_k-w_k)\frac{\nabla P}{P}\right)\right]+\rho w_{H_2}\mathbf{u}\right]=0 \tag{3.49}$$

$$\frac{\partial}{\partial t}(\rho w_{H_2O})+\nabla\cdot\left[-\rho w_{H_2O}\sum_{k=1}^{3}\left[\tilde{D}^{eff}_{H_2O,k}\left(\nabla x_k+(x_k-w_k)\frac{\nabla P}{P}\right)\right]+\rho w_{H_2O}\mathbf{u}\right]=0 \tag{3.50}$$

In the fuel channel:

$$\frac{\partial}{\partial t}(\rho w_{H_2})+\nabla\cdot\left[-\rho w_{H_2}\sum_{k=1}^{3}\left[\tilde{D}_{H_2,k}\left(\nabla x_k+(x_k-w_k)\frac{\nabla P}{P}\right)\right]+\rho w_{H_2}\mathbf{u}\right]=0 \tag{3.51}$$

$$\frac{\partial}{\partial t}(\rho w_{H_2O})+\nabla\cdot\left[-\rho w_{H_2O}\sum_{k=1}^{3}\left[\tilde{D}_{H_2O,k}\left(\nabla x_k+(x_k-w_k)\frac{\nabla P}{P}\right)\right]+\rho w_{H_2O}\mathbf{u}\right]=0 \tag{3.52}$$

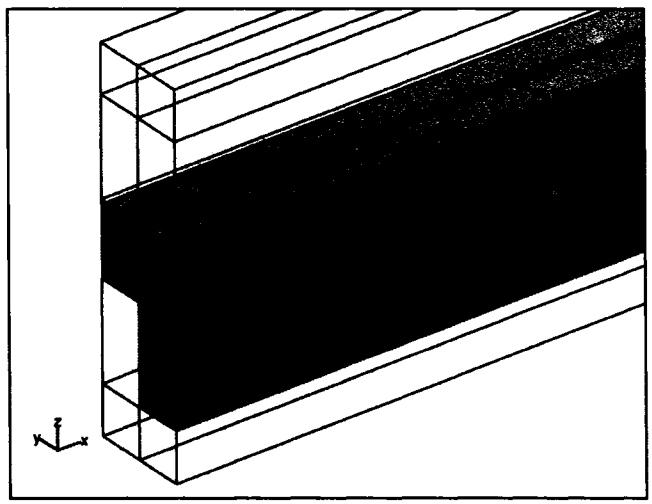

Figure 3.7: Applicable domains for mass transport (fuel).

In both modelling domains, the mass fraction of nitrogen is calculated by

$$w_{N_2} = 1 - w_{H_2} - w_{H_2O} \tag{3.53}$$

Boundary Condition - Anode and Fuel Channel

The mass fractions of hydrogen and water are specified at the fuel channel inlet.

$$w_{H_2} = w_{H_2,in} \tag{3.54}$$

$$w_{H_2O} = w_{H_2O,in} \tag{3.55}$$

At the fuel channel outlet, a convective flux boundary condition is imposed. It is again assumed that the gas channel is convection-dominated.

$$-\mathbf{n} \cdot \left[-\rho w_{H_2} \sum_{k=1}^{3} \left[\tilde{D}_{H_2,k} \left(\nabla x_k + (x_k - w_k) \frac{\nabla P}{P} \right) \right] \right] = 0 \tag{3.56}$$

$$-\mathbf{n} \cdot \left[-\rho w_{H_2O} \sum_{k=1}^{3} \left[\tilde{D}_{H_2O,k} \left(\nabla x_k + (x_k - w_k) \frac{\nabla P}{P} \right) \right] \right] = 0 \tag{3.57}$$

At the anode-electrolyte interface, the rates of production of hydrogen and consumption of water are proportional to the rate of the anodic current density, J_A, given by the Butler-Volmer equation.

$$-\mathbf{n}\cdot\left[-\rho w_{H_2}\sum_{k=1}^{3}\left[\tilde{D}^{eff}_{H_2,k}\left(\nabla x_k+(x_k-w_k)\frac{\nabla P}{P}\right)\right]+\rho w_{H_2}\mathbf{u}\right]=-\frac{J_A}{2F}MW_{H_2} \quad (3.58)$$

$$-\mathbf{n}\cdot\left[-\rho w_{H_2O}\sum_{k=1}^{3}\left[\tilde{D}^{eff}_{H_2O,k}\left(\nabla x_k+(x_k-w_k)\frac{\nabla P}{P}\right)\right]+\rho w_{H_2O}\mathbf{u}\right]=\frac{J_A}{2F}MW_{H_2O} \quad (3.59)$$

Since the fuel does not escape through any other boundaries, the insulated boundary condition is specified elsewhere.

$$-\mathbf{n}\cdot\left[-\rho w_{H_2}\sum_{k=1}^{3}\left[\tilde{D}_{H_2,k}\left(\nabla x_k+(x_k-w_k)\frac{\nabla P}{P}\right)\right]+\rho w_{H_2}\mathbf{u}\right]=0 \quad (3.60)$$

$$-\mathbf{n}\cdot\left[-\rho w_{H_2O}\sum_{k=1}^{3}\left[\tilde{D}_{H_2O,k}\left(\nabla x_k+(x_k-w_k)\frac{\nabla P}{P}\right)\right]+\rho w_{H_2O}\mathbf{u}\right]=0 \quad (3.61)$$

3.4.4 Momentum Transport

Since convection plays a dominant role in the mass and heat transports in the gas channel, it is necessary that the fluid velocity and partial pressure be modelled to examine their effects on the cell performance. Also, several transport phenomena occur simultaneously in the porous electrode. The conservation of momentum must extend to the porous structure to accurately examine the flow effect. Here, the equation of motion (neglecting the gravity term) is considered [10].

$$\rho\frac{D\mathbf{u}}{Dt}=-\nabla\cdot P+\nabla\cdot\vec{\tau} \quad (3.62)$$

where $\vec{\tau}$ is the stress tensor. For an ideal monoatomic gas, the form of stress tensor is expressed as

$$\vec{\tau}=\mu\left((\nabla\mathbf{u}+(\nabla\mathbf{u})^T)-\frac{2}{3}\nabla\cdot\mathbf{u}\right) \quad (3.63)$$

where μ is the dynamic viscosity. By combining the stress tensor and the equation of motion, it follows that

$$\rho\frac{D}{Dt}(\mathbf{u})=\nabla\cdot\left[-P+\mu(\nabla\mathbf{u}+(\nabla\mathbf{u})^T)-\frac{2}{3}\mu\nabla\cdot\mathbf{u}\right] \quad (3.64)$$

Expanding the substantial derivative term, the momentum transport becomes

$$\rho\frac{\partial \mathbf{u}}{\partial t} + \rho\mathbf{u}\cdot\nabla\mathbf{u} = \nabla\cdot\left[-P + \mu(\nabla\mathbf{u} + (\nabla\mathbf{u})^T) - \frac{2}{3}\mu\nabla\cdot\mathbf{u}\right] \tag{3.65}$$

The above equation is also known as the general Navier-Stokes equation which is often used in conjunction with the continuity equation.

$$\frac{\partial \rho}{\partial t} + \nabla\cdot(\rho\mathbf{u}) = 0 \tag{3.66}$$

In the gas channels, the pressure and the velocity are modelled using Equation (3.65) and Equation (3.66). In the porous electrodes, the flow is modelled using the Darcy's Law

$$\mathbf{u} = -\frac{\kappa}{\mu}\nabla P \tag{3.67}$$

where κ is the permeability of the porous electrode. The continuity equation for porous medium is adjusted with the porosity, ε, as shown below.

$$\frac{\partial(\rho\varepsilon)}{\partial t} + \nabla\cdot\left[\rho\left(-\frac{\kappa}{\mu}\nabla P\right)\right] = 0 \tag{3.68}$$

Subdomain Equation - Gas Channels

The momentum transport equation applies to both the air and fuel channels as shown in Figure 3.8. At the anode and cathode gas channel, the flow transport is modelled using the Equation (3.65) and Equation (3.66).

Boundary Condition - Gas Channels

Uniform velocity is specified at the gas channel inlets.

$$\mathbf{u}_x = 0, \tag{3.69}$$

$$\mathbf{u}_y = 0, \tag{3.70}$$

$$\mathbf{u}_z = \begin{cases} u_{C,in}, & \text{At the air channel inlet} \\ u_{A,in}, & \text{At the fuel channel inlet} \end{cases} \tag{3.71}$$

Zero velocity or no-slip condition is applied along the gas channel walls.

$$\mathbf{u} = 0 \tag{3.72}$$

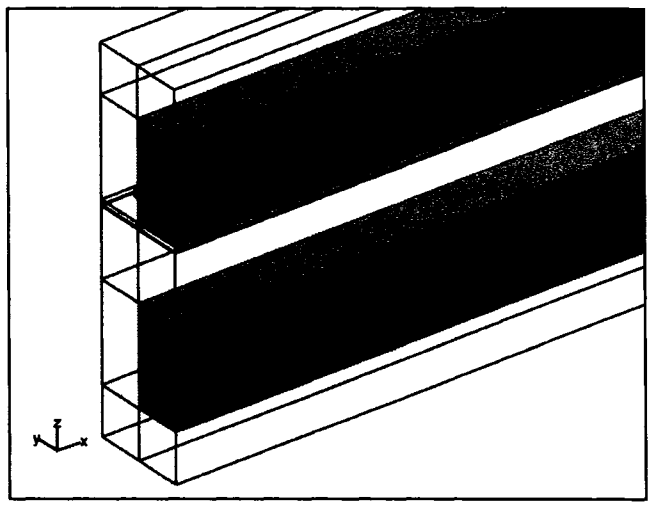

Figure 3.8: Applicable domains for momentum transport.

At the gas channel outlets, the pressures and the normal flow boundary condition are specified.

$$P = \begin{cases} P_{C,out} & \text{At the air channel outlet} \\ P_{A,out} & \text{At the fuel channel outlet} \end{cases} \tag{3.73}$$

$$\mathbf{t} \cdot \mathbf{u} = 0 \tag{3.74}$$

The outlet pressures $P_{C,out}$ and $P_{A,out}$ are both 1 atm. The above boundary condition indicates that the tangential velocity is negligible at the boundary where pressure is specified. For the boundary along the axis of symmetry, the perpendicular velocity component is set to zero. This is referred to as a slip boundary condition.

$$\mathbf{n} \cdot \mathbf{u} = 0 \tag{3.75}$$

Subdomain Equation - Porous Electrodes

Momentum transport in porous electrodes using the Darcy's law applies to the domains shown in Figure 3.9. Equation (3.68) is applied to both electrodes. For example, the mod-

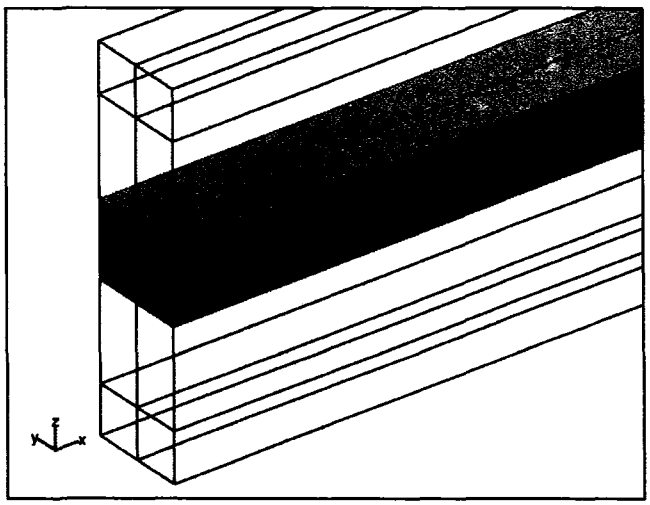

Figure 3.9: Applicable domain for momentum transport in porous media.

elling equation at the cathode is

$$\frac{\partial(\rho\varepsilon_C)}{\partial t} + \nabla \cdot \left[\rho\left(-\frac{\kappa_C}{\mu_C}\nabla P\right)\right] = 0 \tag{3.76}$$

Boundary Condition - Porous Electrodes

At the electrode-electrolyte boundaries, the change in the gas velocity depends on the net rate of the species produced and consumed at that interface. At the cathode-electrolyte interface, the net change in velocity is

$$-\mathbf{n}\cdot\mathbf{u} = \left(-\frac{MW_{O_2}}{4F}\right)\frac{J_C}{\rho} \tag{3.77}$$

At the anode-electrolyte interface, the change in velocity is

$$-\mathbf{n}\cdot\mathbf{u} = \left(-\frac{MW_{H_2}}{2F} + \frac{\mathrm{MW_{H_2O}}}{2F}\right)\frac{J_A}{\rho} \tag{3.78}$$

Pressure condition at the electrode-gas channel interfaces are specified to be equal to the pressure at the gas channel walls.

$$P_{\text{Darcy}} = P_{\text{Navier-Stokes}} \tag{3.79}$$

Insulation/symmetry condition is applied to all of the remaining boundary.

$$-\mathbf{n}\cdot\left(-\frac{\kappa}{\mu}\nabla P\right)=0 \tag{3.80}$$

3.4.5 Heat Transport

It is known that the temperature distribution in the SOFC strongly influences the cell performance. Many mechanical properties of the SOFC components are also strongly temperature dependent. Therefore, it is vital to develop a heat transport model that can account for various heat effects in both the solid structure and the gas channel. It is generally agreed that the conductive heat transfer predominates in the porous electrode and the electrolyte layers, whereas the convective heat dominates in the flow channels. Hence, the temperature distribution in the solid structure will be modelled separately from the gas channels.

The heat transport equation applies to the entire modelling domain. A general heat transport equation is of the form

$$\frac{\partial}{\partial t}\left((\rho C_p)T\right)=-\nabla\cdot\left(-k_{eff}\nabla T+(\rho C_p)_f\mathbf{u}T\right)+Q \tag{3.81}$$

where C_p is the specific heat capacity, k is the thermal conductivity and Q is the heat source. The subscript eff denotes the effective parameters associated with the solid and fluid regions, e.g., the porous electrodes, where f represents the fluid property. For example, the effective thermal conductivity of a porous electrode is determined from [7]

$$k_{eff}=\varepsilon k_f+(1-\varepsilon)k_s \tag{3.82}$$

where ε is the electrode porosity and the subscript s denotes the property of solid electrodes. Since heat transfer in the solid structure is conduction-dominated, the heat transfer equation is reduced to

$$\frac{\partial}{\partial t}\left((\rho C_p)T\right)=-\nabla\cdot\left(-k_{eff}\nabla T\right)+Q \tag{3.83}$$

In the electrodes and the electrolyte, the heat source, Q, is generated by various means. The followings describe the heat effects found in SOFC [51]:

- Ohmic heating due to resistances in ionic and electronic conducting materials.

- Heat generated by the activation overpotentials under a non-equilibrium condition.
- Heat loss through entropy change in the electrochemical reactions.
- Heat of side reactions occurring in the electrodes.

Since hydrogen is used as fuel in this proposed model, no chemical reaction such as the reforming reaction occurs. The heat of reaction term can be disregarded in this case. Other types of heat source are discussed below.

Ohmic Heating is the heat generated by the material resistance due to current flow. Both ionic and electronic currents contribute to the heat generation according to Ohm's Law. Heat produced by ionic and electronic resistances are of the form

$$Q_{ohm,io} = \frac{J_{io}^2}{\sigma_{io}} \tag{3.84}$$

and

$$Q_{ohm,el} = \frac{J_{el}^2}{\sigma_{el}} \tag{3.85}$$

Ohmic heating is generated in all ionically and electronically conductive domains.

Activation Heat The activation overpotential contributes to the heat generation at the electrode-electrolyte boundaries. This is an irreversible heat loss which is not recoverable from the electrochemical reaction. Activation heat at the electrode-electrolyte boundaries are the product of the electronic current and the activation overpotential [51].

$$Q_{act,C} = J_{el}\eta_{act,C} \tag{3.86}$$

$$Q_{act,A} = J_{el}\eta_{act,A} \tag{3.87}$$

Entropy Change The overall entropy change ($T\Delta S$) is a reversible heat loss involved in the SOFC chemical reactions (Equation (2.3)), which takes place at the electrode-electrolyte boundaries. Some part of the energy provided by the overall reaction cannot be completely converted to electrical energy. As a results, the change in entropy of reaction contributes to heat generation at the electrode-electrolyte interfaces [21]. The entropic heat effects are generated in unequal amounts the the interfaces. It is also known that most of the heat

is generated in the cathode-electrolyte boundary [35, 51]. To investigate the entropic heat effect at each electrode, the entropy change is separated into the local entropy change for each half cell reaction. The reversible entropy loss at the cathode-electrolyte boundary is

$$Q_{rev,C} = J_{el}\left(-\frac{T(\Delta S)_C}{2F}\right) \tag{3.88}$$

Similarly, the entropy change at the anode-electrolyte boundary is

$$Q_{rev,A} = J_{el}\left(-\frac{T(\Delta S)_A}{2F}\right) \tag{3.89}$$

Where $(\Delta S)_C$ and $(\Delta S)_A$ are the entropy change of the half cell reaction at the cathode and the anode, respectively. According to Singhal and Kendall (2003) [47], the half-cell entropy can be calculated from

$$(\Delta S)_C = S^*_{O^{2-}} - \frac{1}{2}S_{O_2} - 2S^*_{e^-} \tag{3.90}$$

and

$$(\Delta S)_A = S_{H_2O} - S_{H_2} - S^*_{O^{2-}} + 2S^*_{e^-} \tag{3.91}$$

where $S^*_{O^{2-}}$ and $S^*_{e^-}$ are the transported entropy of the oxygen ion and the electron, respectively. The value of the transported entropy for the half-cell SOFC reaction with YSZ electrolyte have been reported in various literatures [35, 41, 43, 42]. Though the reported values are not consistent, they have been found to be within the same magnitude of one another. In the present study, the transported entropy of the oxygen ion and the electron of 42 J/(molK) and -1 J/(molK) are used, respectively [42].

It has been determined that surface radiation contributes to the overall heat effect in SOFC, and the radiative effect must be incorporated in the heat model [51]. Since radiation is a form of surface heat transfer, the radiative heat effect is implemented as a boundary condition along the flow channel walls.

Subdomain Equation - Solid Temperature

In the solid region, the heat equation applies to the interconnects, electrolyte, and electrodes as shown in Figure 3.10. At the anode and cathode interconnects, the following conductive heat models are applied.

$$(\rho C_p)_{CI}\frac{\partial T_s}{\partial t} = -\nabla\cdot(-k_{CI}\nabla T_s) + Q_{ohm,CI} \tag{3.92}$$

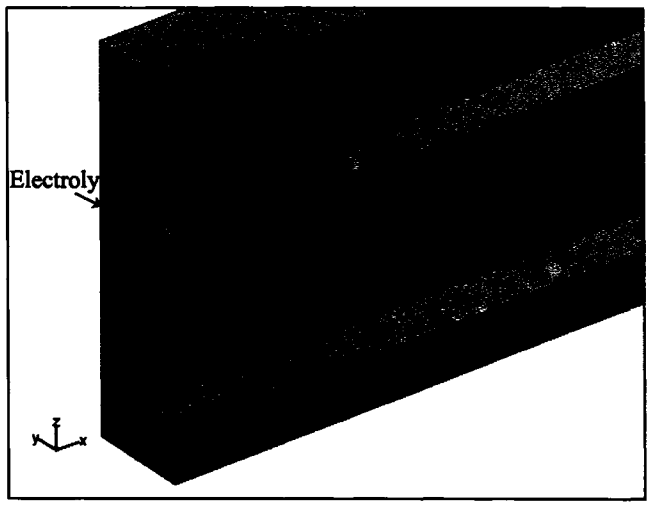

Figure 3.10: Applicable domains for solid temperature modelling.

$$(\rho C_p)_{AI}\frac{\partial T_s}{\partial t} = -\nabla \cdot (-k_{AI}\nabla T_s) + Q_{ohm,AI} \tag{3.93}$$

At the electrolyte, cathode, and anode, the heat balance equations respectively are

$$(\rho C_p)_{E}\frac{\partial T_s}{\partial t} = -\nabla \cdot (-k_{E}\nabla T_s) + Q_{ohm,E} \tag{3.94}$$

$$(\rho C_p)_{eff,C}\frac{\partial T_s}{\partial t} = -\nabla \cdot (-k_{eff,C}\nabla T_s) + Q_{ohm,C} \tag{3.95}$$

$$(\rho C_p)_{eff,A}\frac{\partial T_s}{\partial t} = -\nabla \cdot (-k_{eff,A}\nabla T_s) + Q_{ohm,A} \tag{3.96}$$

Boundary Condition - Solid Temperature

At the cathode-electrolyte boundary, the heat flux is generated by the activation overpotential and the reversible entropy change in the half cell reaction.

$$-\mathbf{n} \cdot (-k_{eff}\nabla T_s) = \left(-\frac{T(\Delta S)_C}{2F} + \eta_{act,C}\right) J_{el} \tag{3.97}$$

The heat flux at the anode-electrolyte boundary is produced in a similar manner.

$$-\mathbf{n} \cdot (-k_{eff}\nabla T_s) = \left(-\frac{T(\Delta S)_A}{2F} + \eta_{act,A}\right) J_{el} \tag{3.98}$$

Since the cell is assumed to be insulated, an adiabatic boundary condition is applied for the outer walls and at the axis of symmetry.

$$-\mathbf{n} \cdot (-k\nabla T_s) = 0 \tag{3.99}$$

Along the faces of the flow channels, an outward heat flux is generated by the convective heat transfer and the surface radiation.

$$-\mathbf{n} \cdot (-k_{eff}\nabla T_s) = h_f(T_{f,bulk} - T_s) + \epsilon\tilde{\sigma}\hat{F}(T_{f,bulk}^4 - T_s^4) \tag{3.100}$$

Here, h_f is the convective heat transfer coefficient in W/m^{2}K, $T_{f,bulk}$ is the bulk fluid temperature, ϵ is the emissivity of the solid, and $\tilde{\sigma}$ is the Stefan-Boltzmann constant (5.67×10^{-8} W/(m^{2}K^4). $\hat{F}$ is the radiative view factor which accounts for the radiative interaction between surfaces. The fundamental expression for the view factor between black-body surfaces is [3]

$$\hat{F}_{1\to 2} = \frac{1}{\pi A_1}\int_{A_1}\int_{A_2}\frac{-(\mathbf{n}_1 \cdot \mathbf{r})(\mathbf{n}_2 \cdot \mathbf{r})}{(\mathbf{r} \cdot \mathbf{r})^2}dA_2 dA_1 \tag{3.101}$$

where $\mathbf{n_1}$ and $\mathbf{n_2}$ are the unit vectors normal to the surfaces A_1 and A_2, respectively. The vector $\mathbf{r}$ represents the distance between the two surfaces as shown in Figure 3.11. The view factor for surface-to-surface radiation is calculated directly from the modelling geometry via COMSOL Multiphysics.

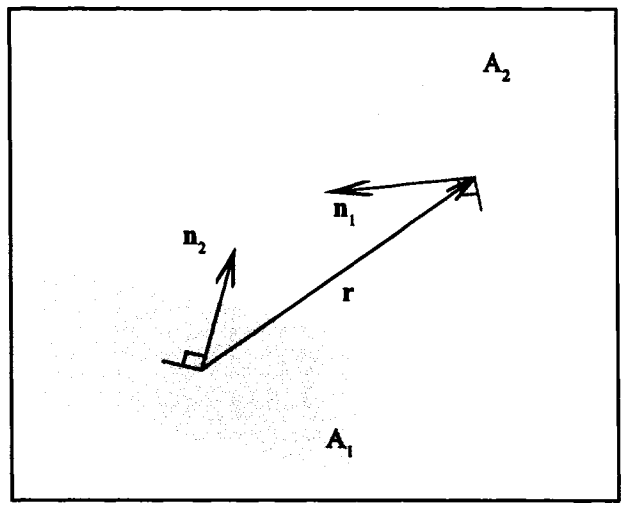

Figure 3.11: Geometry for the view factor calculation.

Subdomain Equation - Fluid Temperature

The fluid temperature model applies to the air and fuel channels. The modelling domains are the same as the Navier-Stokes flow modelling domains shown in Figure 3.8. Since convection predominates conduction in the gas phase, the convective heat flux, $(\rho C_p)_f \mathbf{u} \cdot \nabla T$, is present in the gas channels. To account for the effect of mass transport in the gas channel, the enthalpy change as a result of species diffusion is included. The heat transport equation applied in the flow channels becomes

$$(\rho C_p)_f \frac{\partial T_f}{\partial t} = -\nabla \cdot (-k_f \nabla T_f + \sum_{i=1}^{N} h_i \mathbf{j}_i) - (\rho C_p)_f \mathbf{u} \cdot \nabla T_f \tag{3.102}$$

where h_i is the species enthalpy in J/kg, and $\mathbf{j}_i$ is the mass flux of species i.

Boundary Condition - Fluid Temperature

The fluid temperature is specified at the gas channel inlets.

$$T_f = \begin{cases} T_{fC,in} & \text{At the air channel inlet} \\ \\ T_{fA,in} & \text{At the fuel channel inlet} \end{cases} \tag{3.103}$$

Due to the convection-dominated heat transfer, the convective flux condition is applied at both outlets of the gas channels. This condition indicates that the flux across the boundary is entirely convective, whereas the conductive heat flux is zero.

$$-\mathbf{n} \cdot (-k_f \nabla T_f) = 0 \tag{3.104}$$

Along the channel wall, the fluid is heated by an inward heat flux from the solid phase, Q_{wall}.

$$-\mathbf{n} \cdot (-k_f \nabla T_f + (\rho C_p)_f T_f \mathbf{u}) = Q_{wall} \tag{3.105}$$

This inward heat flux boundary condition is coupled with the amount of heat produced by the solid structure. Lastly, a symmetry condition is specified around the axis of symmetry of the gas channels.

$$-\mathbf{n} \cdot (-k_f \nabla T_f + (\rho C_p)_f T_f \mathbf{u}) = 0 \tag{3.106}$$

3.5 Mesh

A structured 3D mesh is constructed for the proposed modelling geometry in COMSOL Multiphysics. Since the geometry consists of rectangular shapes, mesh elements are composed of 3D rectangular parallelepiped with faces perpendicular to one another. As a result, three component vectors in x, y, and z direction are represented accurately. Figure 3.12 illustrates the mesh used in this work. The mesh parameters are summarized in Table 3.2.

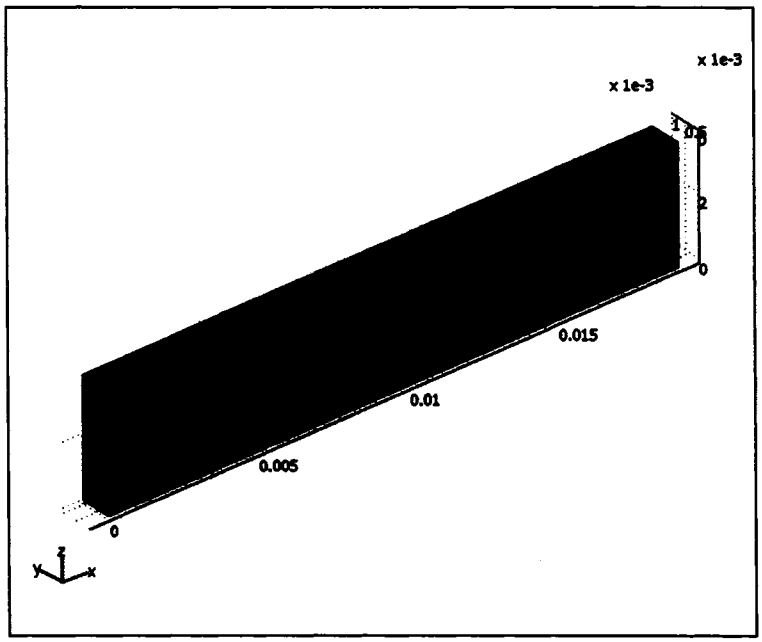

Figure 3.12: Mapped mesh for 3D geometry.

3.5.1 Solver Settings

To solve the model in a stationary (steady-state) mode, the sparse matrix direct solver called the unsymmetric multifrontal package (UMFPACK) was used to solve the linear systems. A relative tolerance of 1×10^{-5} is specified for the nonlinear system solver.

Table 3.2: Summary of 3D mesh parameters.

Parameter	Value
Number of degree of freedom	42,487
Number of elements	1,152
Number of boundary elements	1,232
Number of edge elements	428
Number of nodes	1,539

In the dynamic simulation, changes to the system input variables with respect to time are generated using a step function. Again, the UMFPACK solver is selected for linear solver setting. The initial and final simulation time are specified, and the automatic time steps are generated using the adaptive time-stepping solver. The relative and absolute tolerance settings for the time-stepping solver are 0.01 and 0.001, respectively.

Chapter 4

Numerical Results and Discussion

4.1 Introduction

This chapter presents the results obtained from the steady-state and dynamic analyses of the proposed SOFC model. The operating parameters and the solution algorithm required to perform the computational simulations are provided. This chapter is organized into two parts. The first part deals with the steady-state results. The model is able to predict the local potentials of the SOFC components, gas composition distributions, gas velocity, pressure, and the temperature gradients in the corresponding modelling domains. The steady-state solutions of the developed model are compared with the experimental results obtained from the literature. The dynamic modelling results are shown in the second part. The solutions obtained from the steady-state analysis are chosen as initial conditions in the time-dependent simulation. SOFC parameters of interest are assigned with step functions to represent practical transient operating conditions of SOFC. The dynamic behaviours and the cell performance are determined from the step responses of the dynamic model.

4.2 Parameters Settings and Solution Algorithm

Table 4.1 presents the model operating parameters: inlet feed compositions, inlet feed flow rates, inlet feed velocities, inlet gas temperature, and outlet gas pressure. The specified parameters were used for the half-channel SOFC model developed in this work.

The algorithm for solving the steady-state and the dynamic model is presented in Figure 4.1. The steady-state model results were obtained for five different fuel compositions,

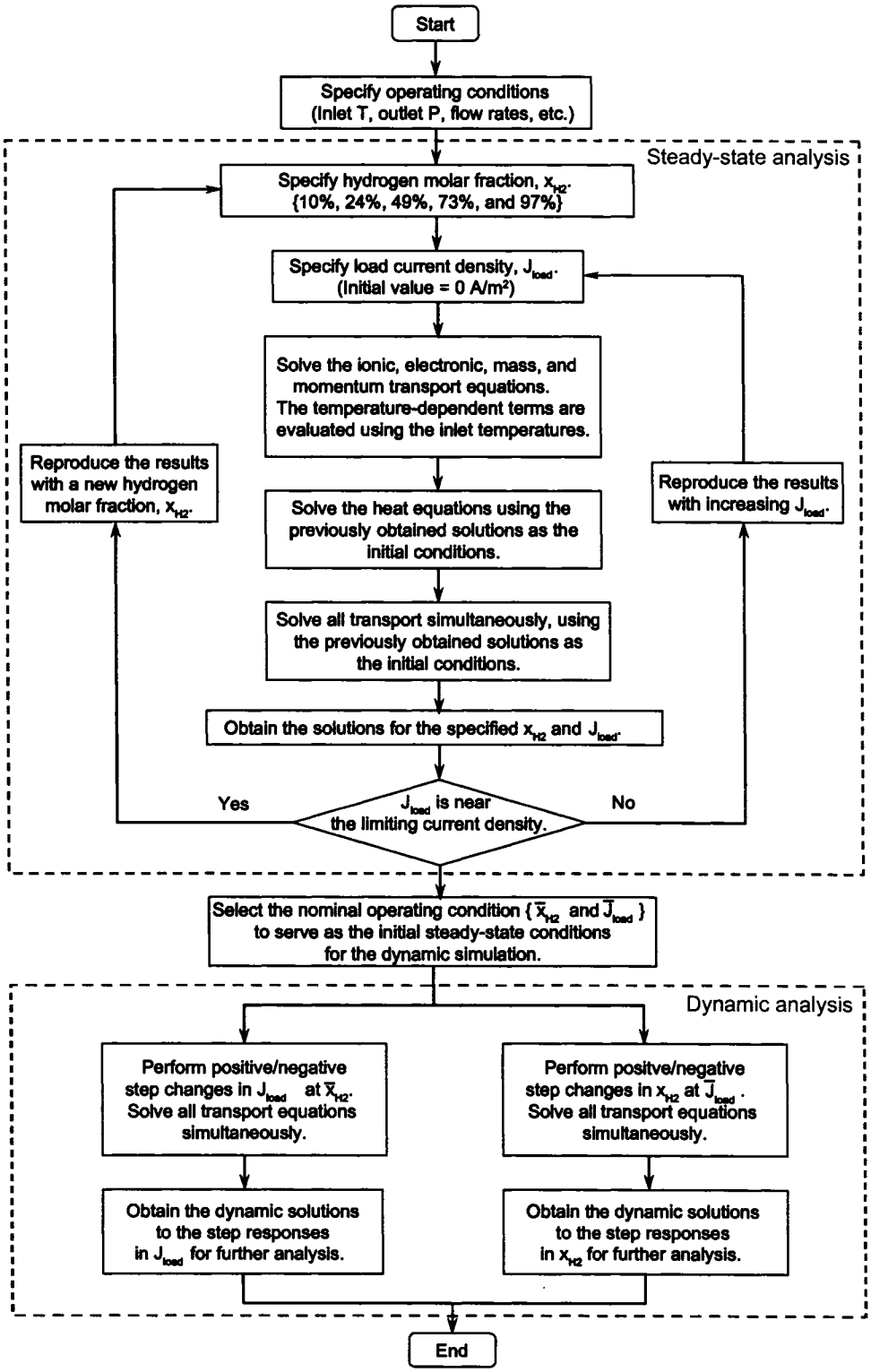

Figure 4.1: Computational algorithm for steady-state and dynamic SOFC model analysis.

Table 4.1: Simulation parameters for the half-channel SOFC model.

Parameter	Fuel	Air
Composition	10 mol% – 97 mol% H_2 3 mol% H_2O Balancing N_2	21 mol% O_2 79 mol% N_2
Flow rate	10 standard cm^3/min	15 standard cm^3/min
Inlet velocity	1.25 m/s	1.87 m/s
Inlet temperature	1,023 K (750°C)	
Outlet pressure	1 atm	

each containing 10%, 24%, 49%, 73%, and 97% hydrogen. The molar fraction of water was specified as 3% in all of the fuel compositions with the remaining molar fraction comprised of nitrogen.

The model was solved by using the specified current density as a forcing function for each fuel composition. The load current densities in the simulation were varied between 0 A/cm^2 to 1.8 A/cm^2. The solutions corresponding to each fuel composition and each current density were determined. After the steady-state analysis was completed, the nominal operating parameters were selected for the time-dependent simulation. These nominal operating conditions were used as the initial conditions for the dynamic model.

In a normal SOFC operation, the external load current was often varied as a result of variable power demand. Since the load current density was directly proportional to the output power, it was considered as a process disturbance. The hydrogen composition in the fuel was also considered as an input parameter of the SOFC model. Step changes in the load current with different magnitudes were performed while the hydrogen concentration was kept constant at its nominal value. The dynamic effects of changes in load disturbances were determined from the solutions to the time-dependent simulations. The dynamic responses of the output voltage to the step changes in the load current were observed. To investigate the effects of changes in the fuel composition on the cell performance, step changes in the molar fraction of hydrogen in the fuel were performed. While the load current densities were maintained constant at their nominal values, the dynamic responses to the hydrogen composition changes were determined.

4.3 Steady-State Analysis

The solutions to the PDE of the SOFC model described in Chapter 3 were obtained using finite element method with COMSOL Multiphysics 3.2b [4]. The proposed model was also tested for mesh independence. The information on the current mesh setting can be found in Table 3.2 of Chapter 3. The steady-state simulation was repeated for the model with a new mesh containing 1,296 elements and 1,710 nodes. Using the finer mesh, the solutions obtained from the repeated model agreed well with the solutions from the proposed model. Thus, it was verified that the model was mesh independent.

To verify that the modelling results were independent on the solver, the solutions were reproduced using different solvers. The sparse object oriented linear equations solver (SPOOLES) and the general minimum residual solver (GMRES) with an incomplete LU preconditioner were used to solve the numerical model. The results obtained from different solvers conformed with each other, thus verifying that the solution was independent on the solver.

4.3.1 Steady-state Modelling Results

Figure 4.2 illustrates the predicted cell voltage and power density as a function of current density for various fuel compositions with the inlet flow temperature of 1,023 K. The general voltage-current characteristic was observed, i.e., the cell potential decreased with increasing current density. It was observed that the lowest V_{OCV} was obtained from the fuel with the lowest hydrogen molar fraction. Therefore, the Nernst equation was confirmed.

The current density at which the voltage approached zero was referred to as the limiting current density. From the overall trend of the performance curve, it was observed that the higher limiting current density was achieved from the fuel with higher hydrogen content. The presence of mass transport limitation was evident as the performance curve approached the limiting current. In this work, the cathode tortuosity of 2.5 was considered [15]. The typical value of the anode tortuosity were reported in the range of 2–10, and most often found to be in the range of 2-6[52]. To simulate the tailing effect in the voltage drop at high current density, the anode tortuosity of 8.5 was specified. At high current density, the depletion of hydrogen at the anode had a stronger effect than the depletion of oxygen at the cathode. This was due to the limitation in the porous anode by long diffusion pathway

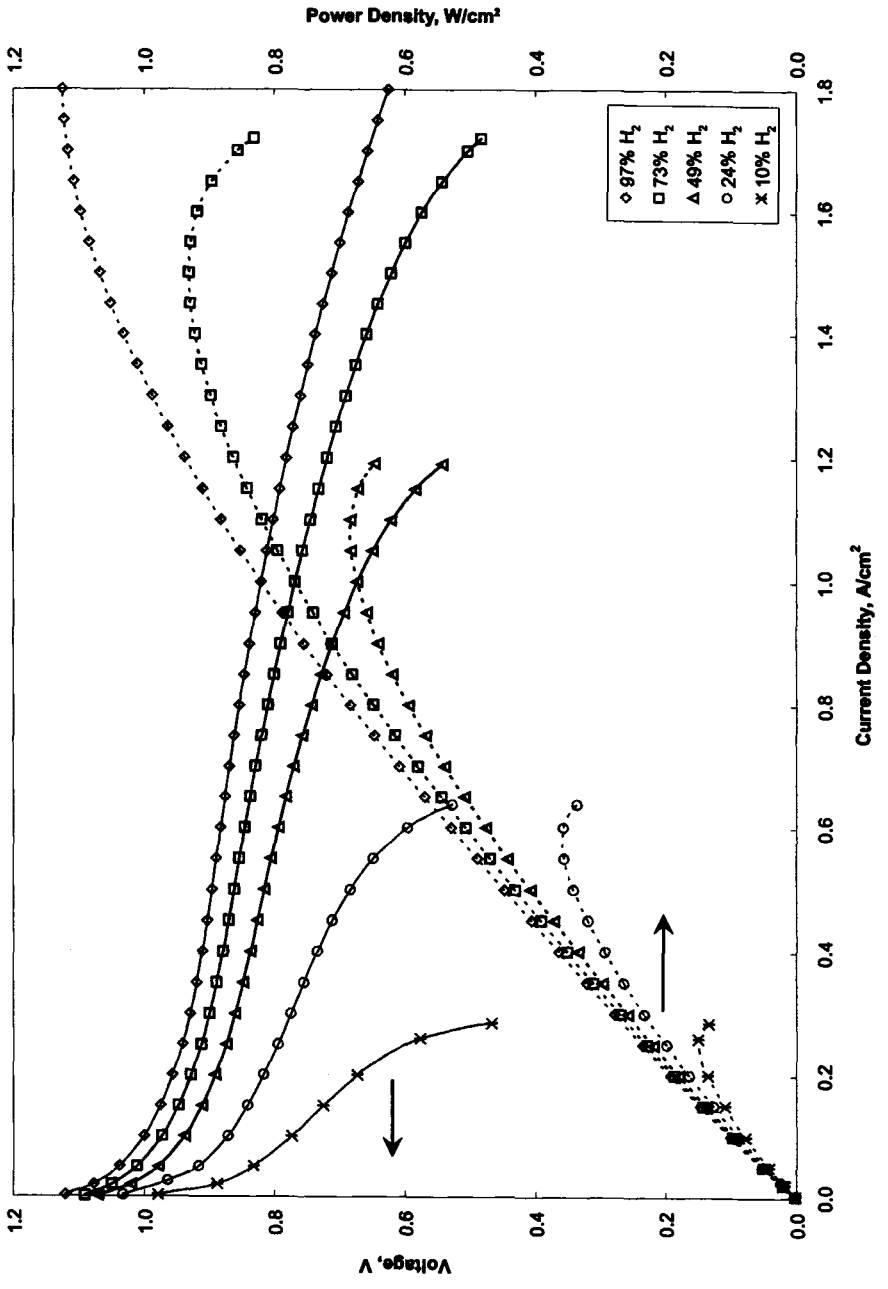

Figure 4.2: Cell voltage and power density as a function of current density at 750°C. The solid line represents the voltage, and the dashed line represents the power density.

in the anode-supported structure and high anode tortuosity. Although high fuel utilization was required at high current density, the amount of diffused hydrogen was not sufficient to supply the electrode reaction. As a result, the sharp drop in the voltage was evident in the high current region. In the low current region, the voltage drop was present as a result of the kinetic limitation of the electrode reactions.

The power density shown in Figure 4.2 was obtained from the product of the cell voltage and current density. The maximum power density was obtained from the fuel with the highest hydrogen content. Again, the power density significantly decreased when the current density approached its limit. For the fuel with 49% hydrogen, it was observed that the power density reached a maximum value of 0.682 W/cm^2 at a current density of 1.10 A/cm^2 and a cell voltage of 0.621 V. When SOFC were operated at their maximum power density, an increase in the load current would cause the voltage and the power output to drop sharply. Therefore, it was essential that SOFC operation did not approach the limiting current region. The information obtained from the predicted cell performance allowed for the envelope of appropriate operating conditions to be established.

The contribution of ionic potential and the activation overpotential losses in SOFC components to the overall voltage for 49% hydrogen fuel is illustrated in Figure 4.3. It was seen that the overall open circuit potential decreased with increasing current density. Thus, it was verified that the irreversible voltage at a specified current density was dependent on the mass diffusion and the temperature distribution at the reactive sites. The overall activation overpotentials contributed to most of the voltage loss between the current density of 0 A/cm^2 to 0.8 A/cm^2. The ionic potential loss by ohmic resistance in the electrolyte layer was more noticeable in the current density range of greater than 0.1 A/cm^2.

The following steady-state modelling results were obtained using the fuel with 49% hydrogen at the current density of 0.8 A/cm^2. The corresponding cell voltage was 0.743 V.

Ionic and Electronic Potentials

The cross-sectional plot of the electronic cell potential in the middle of the SOFC is presented in Figure 4.4. The overall cell voltage was calculated from the potential difference between the cathode and anode interconnects. The arrows represented the direction of the

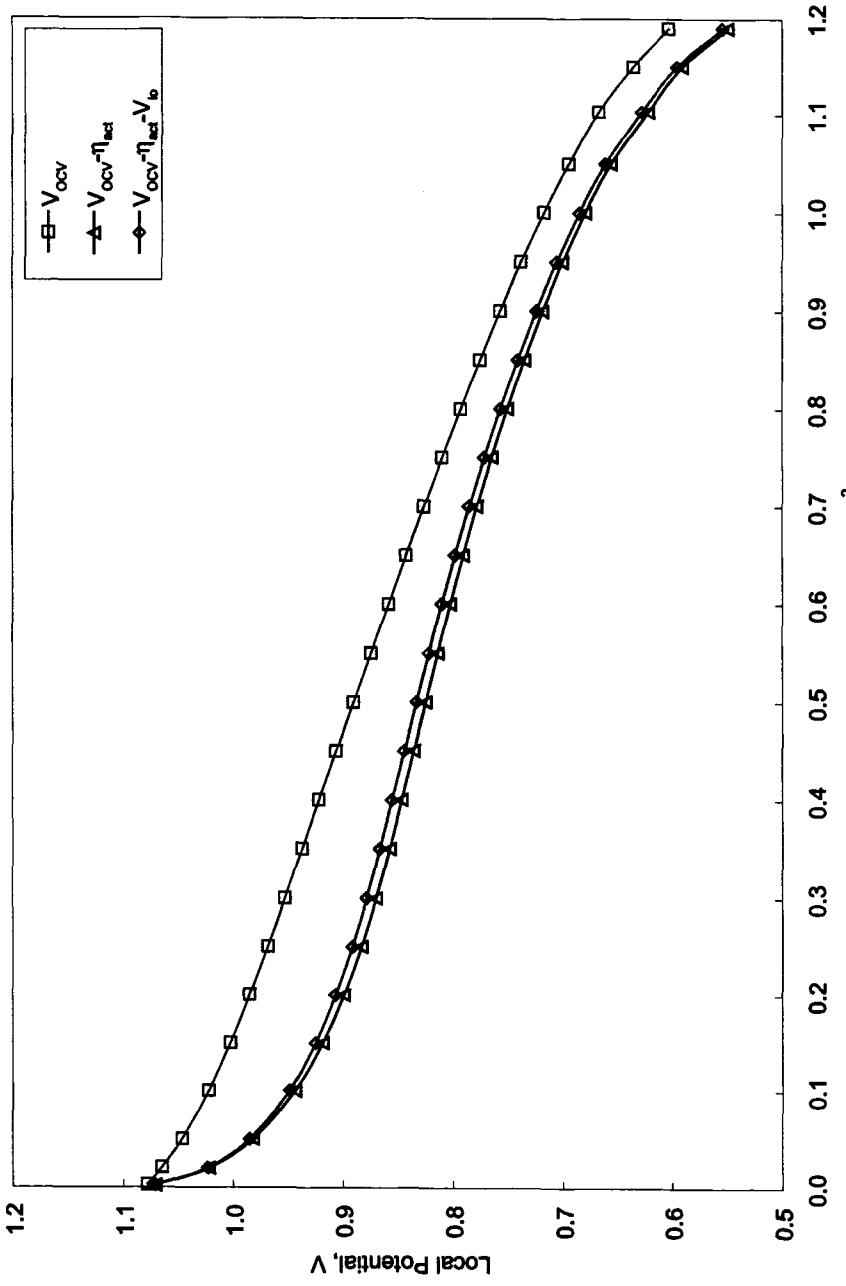

Figure 4.3: Potential losses as a function of current density for 49% H_2 fuel.

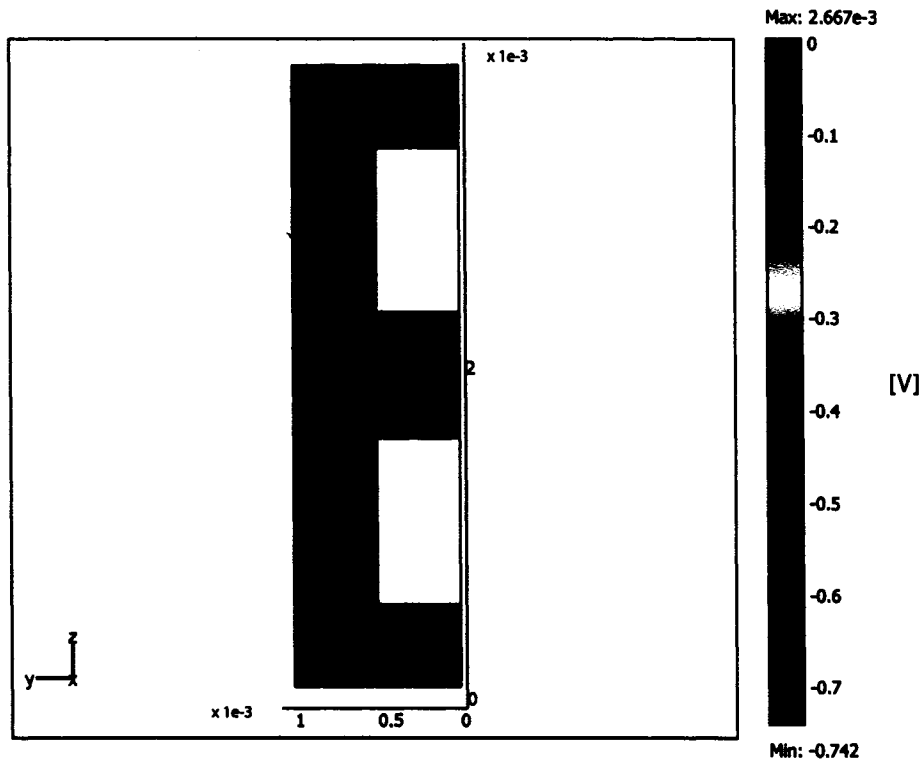

Figure 4.4: Cross-sectional voltage (x = 9.5 mm) with arrows showing the direction of the current flow. The arrow magnitude is proportional to the current density.

current flow. A detailed illustration of the current streamlines is shown in Figure 4.5. The magnitude of the current density was largest as the current flew through the corners of the electrode-gas channels due to the geometry effect. This was more prominent at the cathode where the layer thickness was much smaller than the anode.

The cathode activation overpotential over the cathode-electrolyte interface is shown in Figure 4.6. To identify the overpotential effect on the ionic and electronic potential, local potentials were plotted as a function of SOFC width in the y-direction and are presented in Figure 4.7. It was observed that the local ionic and electronic potentials gradients were highest under the interconnect area (y = 0.5–1.0 mm). The electronic current flew directly from the interconnect to the cathode without diverting underneath the air channels. Therefore, the electrochemical kinetics was enhanced in this region.

The anode activation overpotential at the anode-electrolyte interface is shown in Fig-

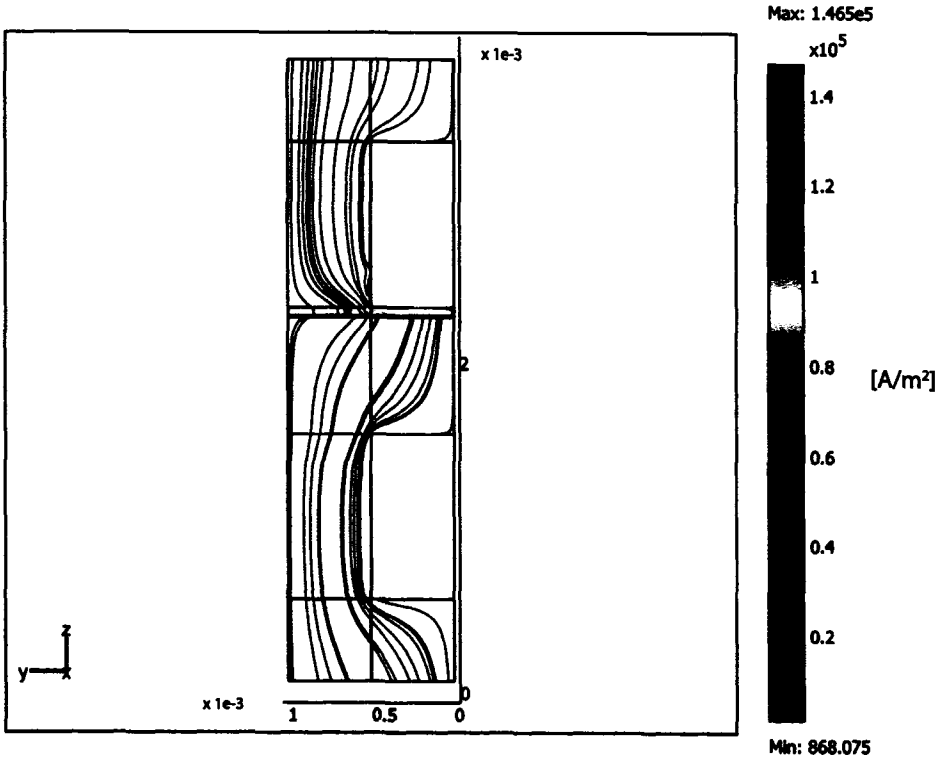

Figure 4.5: Cross-sectional SOFC showing streamlines of current density (x = 0 mm) for 49% H_2 fuel at 0.8 A/cm^2.

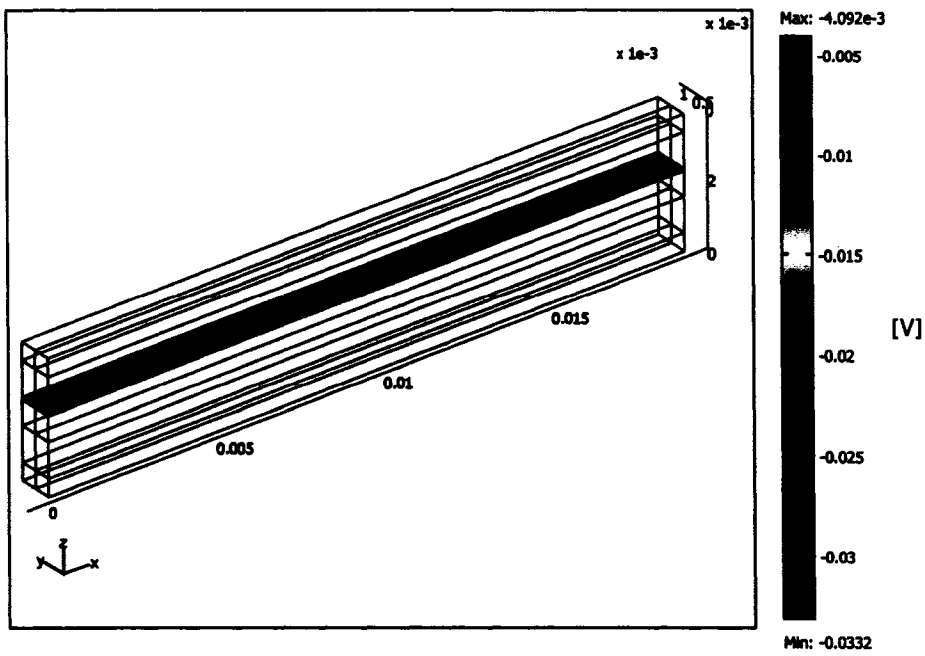

Figure 4.6: Activation overpotential at the cathode-electrolyte interface for 49% H_2 fuel at 0.8 A/cm^2.

ure 4.8. The anode activation overpotential relative to the local ionic, electronic, and open circuit potentials is presented in Figure 4.9. The gradients of the anode activation overpotential, ionic and open circuit potentials were less observable when compared with that of the cathode. The overpotential loss was higher in the cathode than the anode due to larger kinetics loss in the cathode half-cell reaction. This was a typical result observed in SOFC with LSM cathode and Ni/YSZ anode [51]. Larger potentials gradients were observed in the region right above the interconnect than the region above the fuel channel. It can be seen that the geometry of the fuel cell has a significant effect on the cell potentials, especially in the electrode-electrolyte regions.

Mass Diffusion and Convection

Anode and Fuel Channel The hydrogen and water distributions in the anode and fuel channel are illustrated in Figure 4.10 and Figure 4.11, respectively. The concentration gradients of hydrogen and water in the fuel channel were not substantial, whereas the gradients were large in the porous anode. It was observed that hydrogen was consumed mostly in the

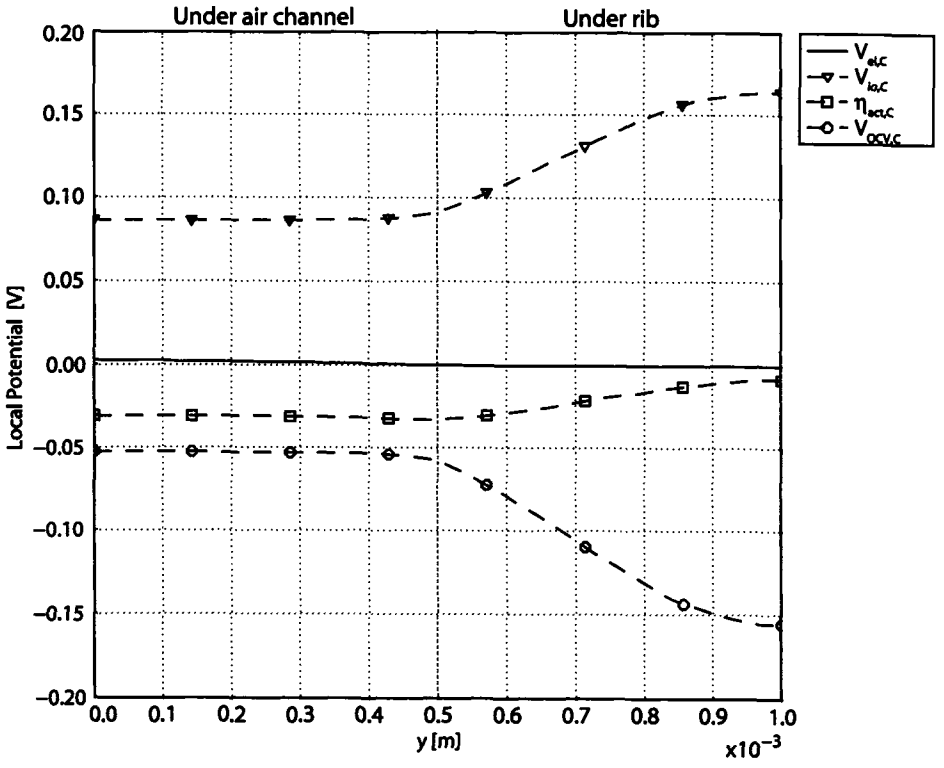

Figure 4.7: Local potentials at the cathode-electrolyte interface (x = 9.5 mm) for 49% H_2 fuel at 0.8 A/cm^2.

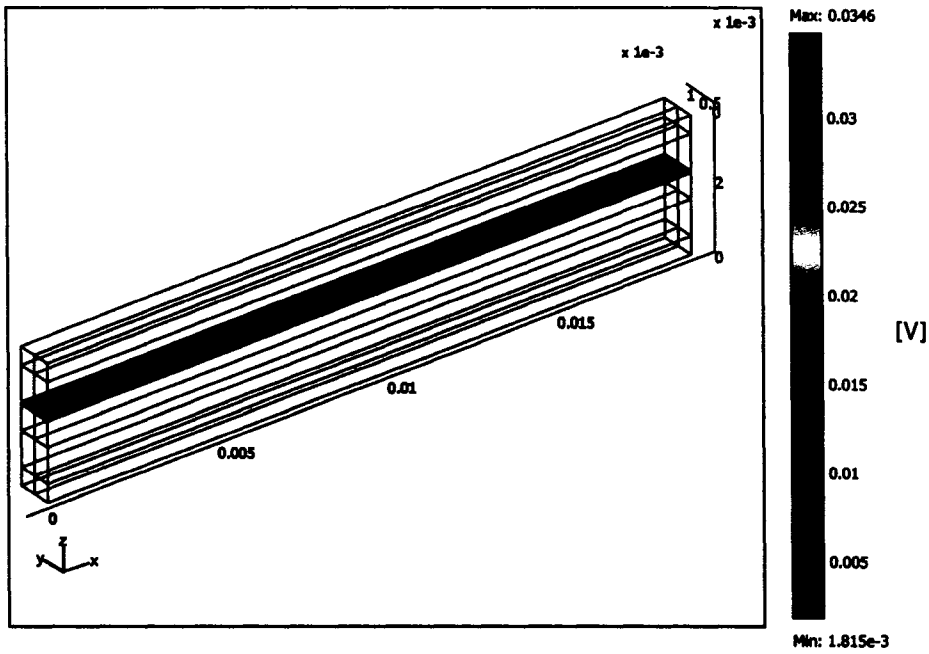

Figure 4.8: Activation overpotential at the anode-electrolyte interface for 49% H_2 fuel at 0.8 A/cm^2.

porous anode close to the fuel channel outlet. This was also the area where the most water was produced. For the planar SOFC with counter-current flow configuration, most of the anode reaction activity occurred in the anode region close to the fuel channel outlet. The outlet molar fraction of hydrogen and water were 39% and 13% , respectively.

The distribution of molar fraction of hydrogen and water from the fuel channel to the anode-electrolyte interface is given in Figure 4.12. It can be seen that the diffusive effect dominated in the porous anode, where the convective effect was dominant in the gas channel.

Cathode and Air Channel The oxygen distribution in the porous cathode and the air channel is shown in Figure 4.13. The gradient of oxygen along the air channel was significantly less than that along the porous cathode. The oxygen concentration at the cathode-electrolyte was almost depleted. Although the thickness of the cathode was smaller than the anode, the diffusivity of oxygen in the cathode was much smaller than that of hydrogen in the anode. This contributed to a large gradient in the oxygen concentration in the porous cathode. The

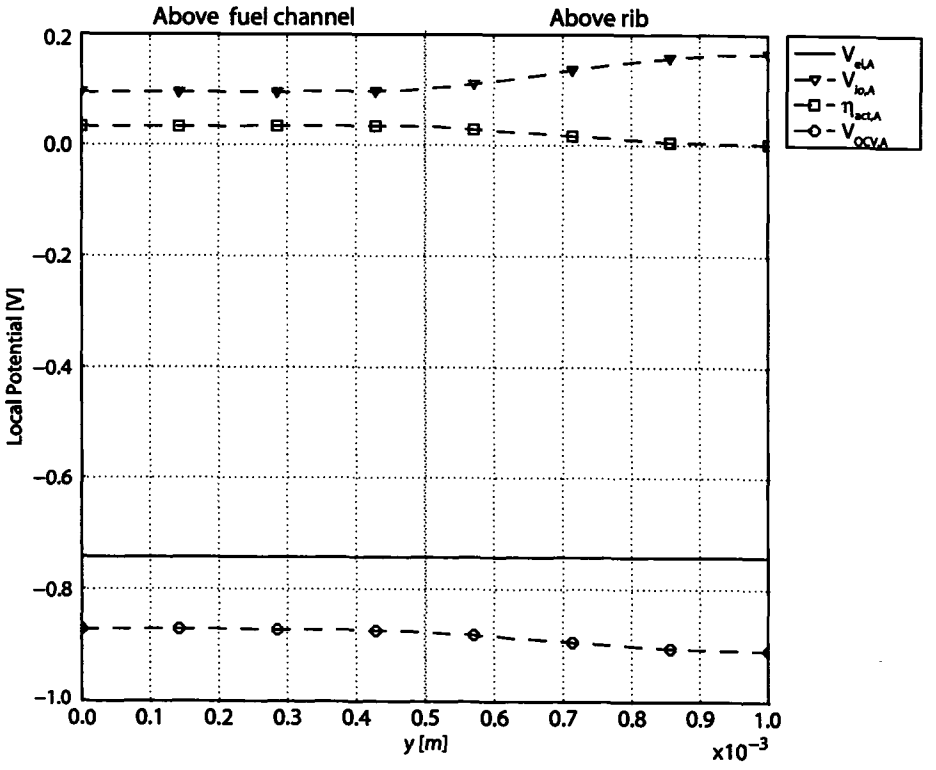

Figure 4.9: Local potentials at the anode-electrolyte interface (x = 9.5 mm) for 49% H_2 fuel at 0.8 A/cm^2.

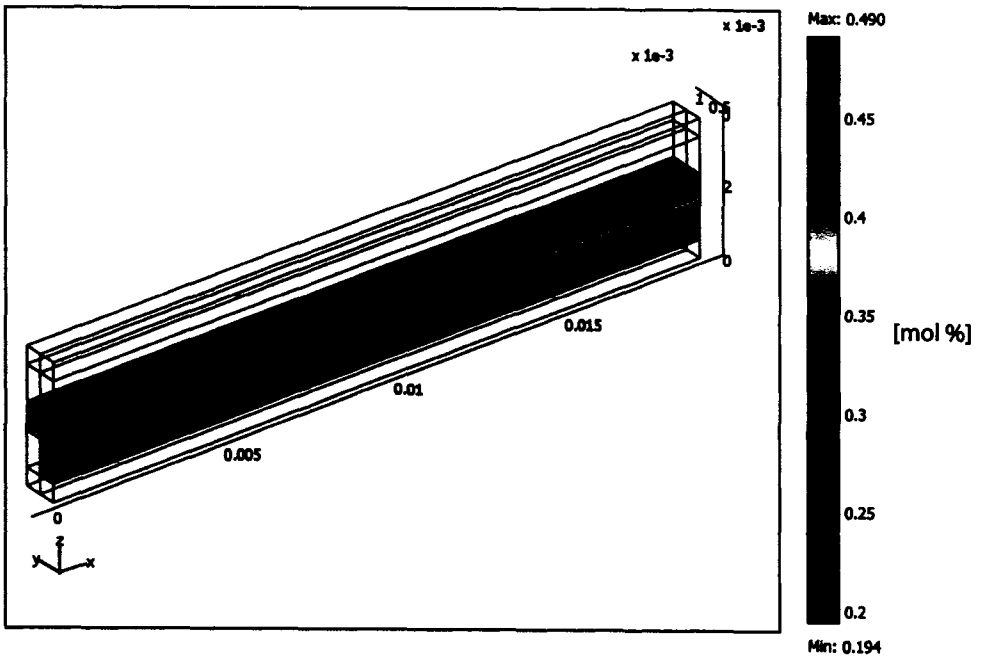

Figure 4.10: Molar fraction of hydrogen in the anode and the fuel channel for 49% H_2 fuel at 0.8 A/cm^2.

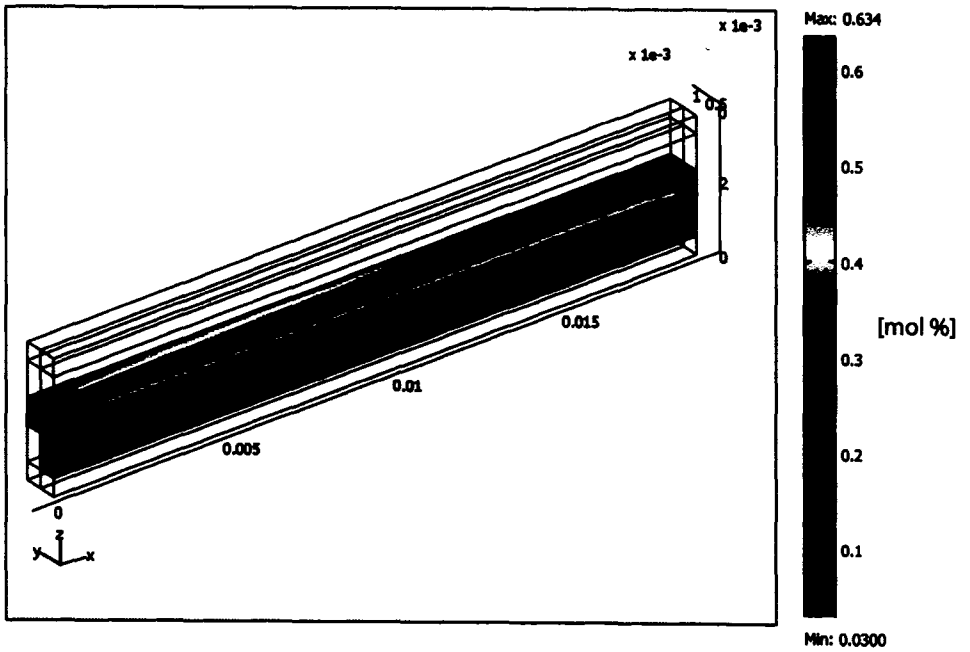

Figure 4.11: Molar fraction of water in the anode and the fuel channel for 49% H_2 fuel at 0.8 A/cm^2.

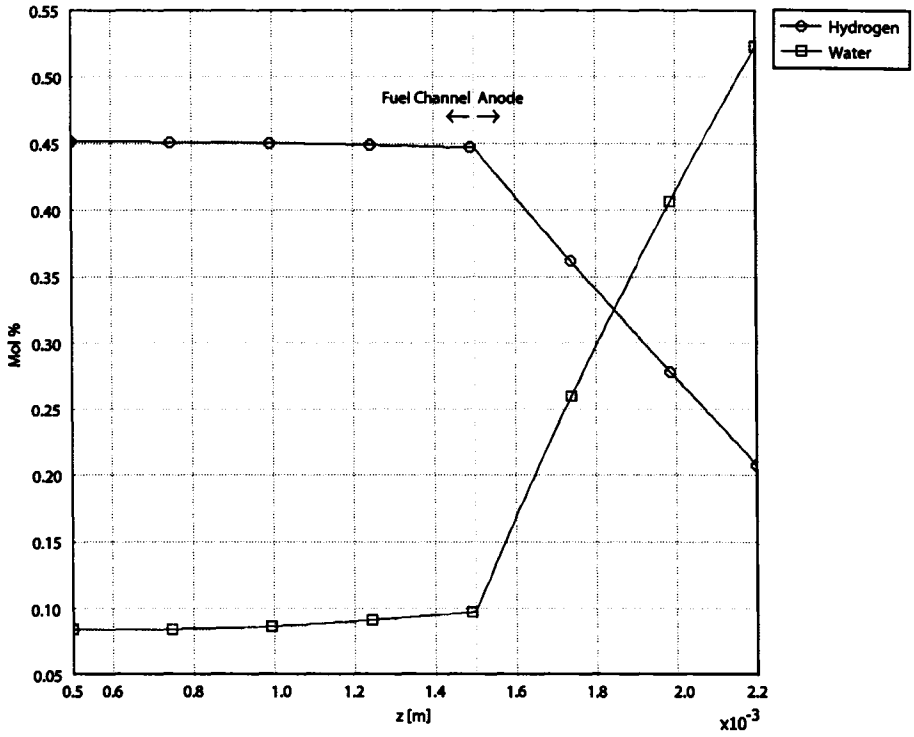

Figure 4.12: Molar fraction of hydrogen and water across the anode and the fuel channel (x = 9.5 mm, y = 0) for 49% H_2 fuel at 0.8 A/cm^2.

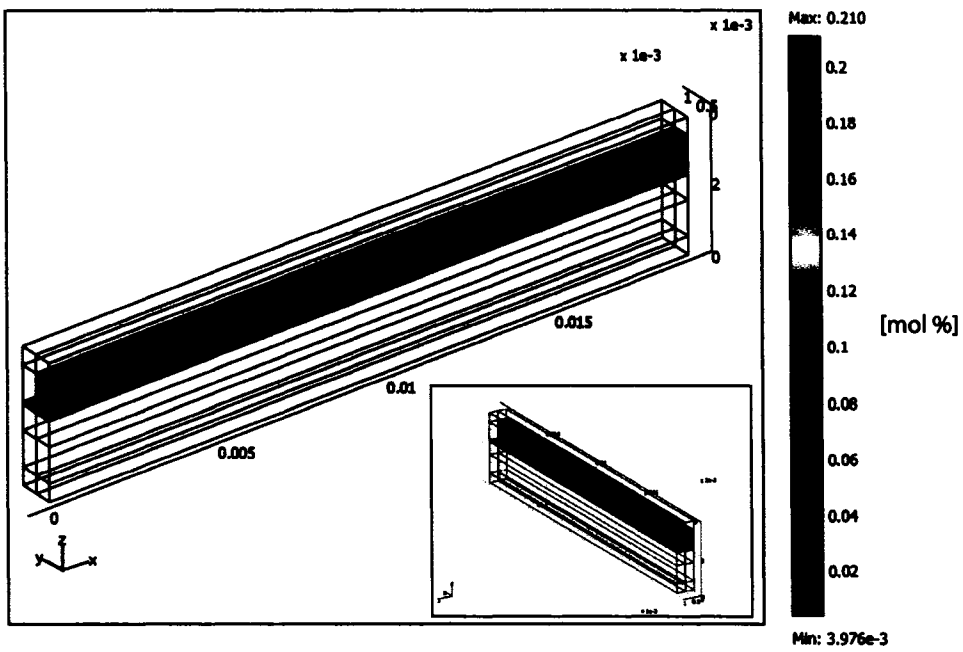

Figure 4.13: Molar fraction of oxygen in the cathode and the air channel for 49% H_2 fuel at 0.8 A/cm^2.

outlet molar fraction of oxygen was approximately 16%.

A closer look at the oxygen concentration gradient from the fuel channel to the cathode-electrolyte interface is given in Figure 4.14. Unlike the gas species at the anode, the molar fraction of oxygen dropped about 12% from the air channel to the cathode-air channel boundary. The mass diffusive effect in the flow channel was larger at the cathode than at the anode.

Fluid Velocity and Pressure

The gas velocities in the flow channels and the porous electrodes are shown in Figure 4.15. The arrow shows the direction of the fluid flow with the magnitude being proportional to the fluid velocity. The fuel and air flows reached their maximum velocity of approximately 3.3 m/s and 5.5 m/s, respectively at their channel outlets. The velocity changes in the porous electrodes relative to the gas channels were considerably less noticeable.

The total fluid pressures in the flow channels and the porous electrodes are shown in Figure 4.16. It was observed that the pressure gradient at the cathode and the air channel

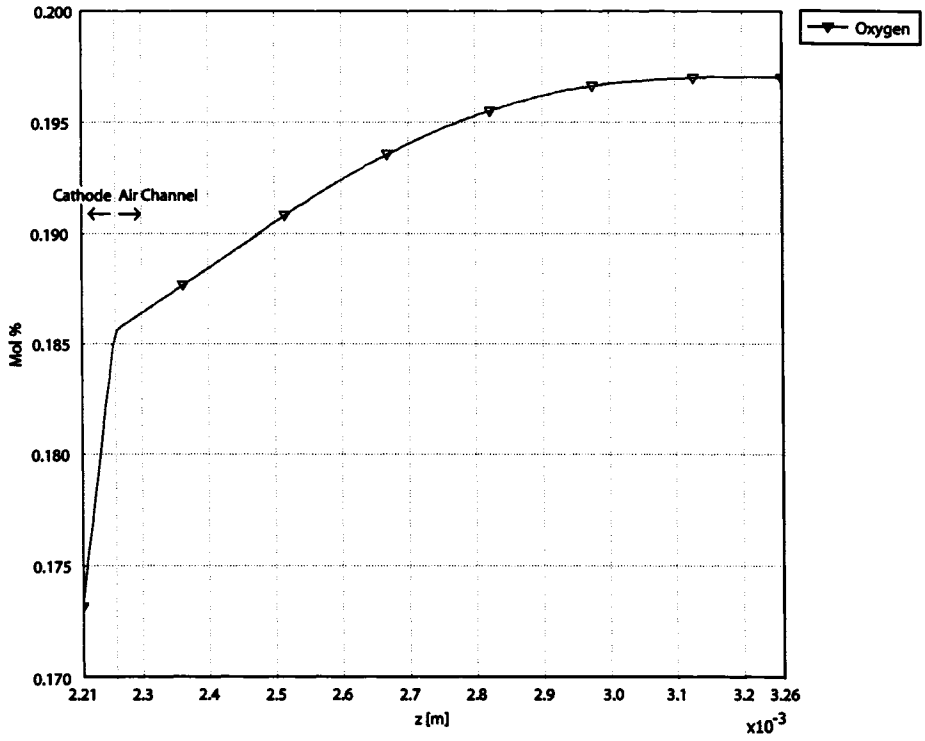

Figure 4.14: Molar fraction of oxygen across the cathode and the air channel (x = 9.5 mm, y = 0) for 49% H_2 fuel at 0.8 A/cm^2.

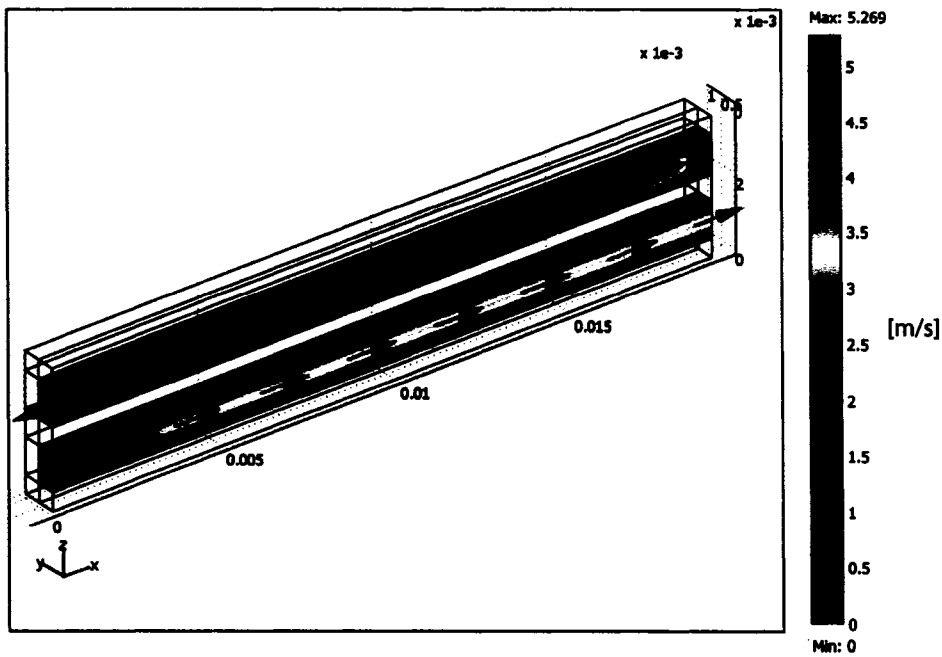

Figure 4.15: Fluid velocity in the electrodes and the gas channels. The arrows show the gas flow directions with the arrow magnitude being proportional to the velocity magnitude.

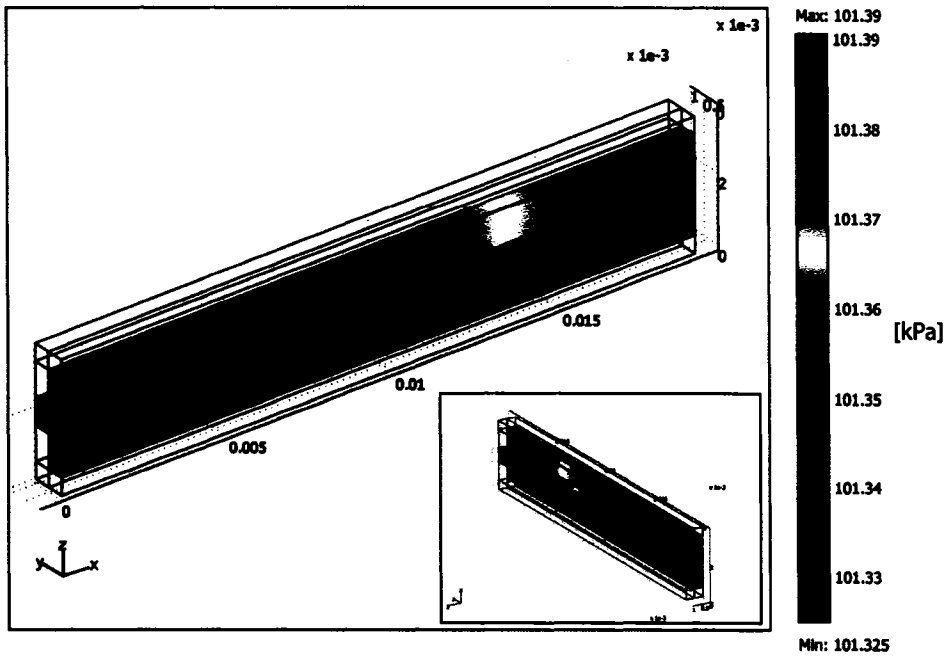

Figure 4.16: Pressure in the gas channels and the porous electrodes for 49% H_2 fuel at 0.8 A/cm^2.

was substantially larger than that of the anode and the fuel channel. The pressure drop in the fuel channel was 30 kPa, whereas the pressure drop in the air channel was 65 kPa. The larger pressure drop occurred as a result of greater fluid velocity.

Temperature Distribution

Solid Temperature The temperature distribution in the solid phase is presented in Figure 4.17. The maximum temperature difference for the overall SOFC was found to be 40 K. The maximum temperature was observed in the electrode-electrolyte area in the middle of the cell. Also, the solid temperature near the air outlet was higher than the temperature near the fuel outlet. The temperature distribution in the anode, cathode, and electrolyte at the middle of the SOFC is illustrated in Figure 4.18. Since the electrochemical reaction of the cathode was exothermic, the highest solid temperature was seen at the interface between the cathode and electrolyte. However, the maximum temperature difference between the electrodes and electrolytes was insignificant (0.56 K).

Figure 4.19 shows the temperature distribution of various interfaces along the cell length

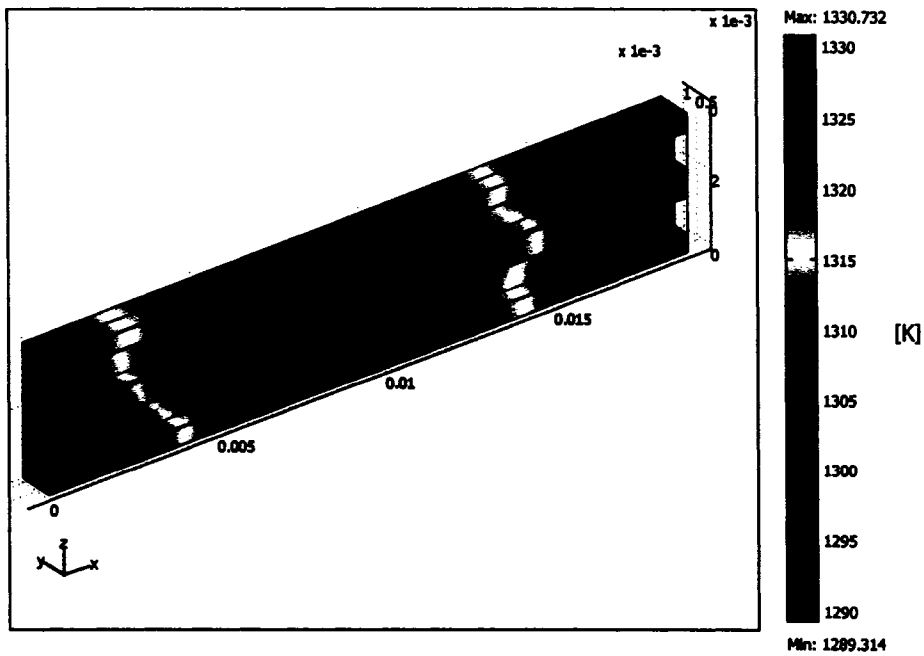

Figure 4.17: Solid temperature of the electrolyte, electrodes, and interconnects for 49% H_2 fuel at 0.8 A/cm^2.

in the x-direction. The largest temperature difference was approximately 35 K. The maximum temperature was observed at the cathode-electrolyte boundary at x = 8.4 mm. Overall, the temperature at the interfaces were higher along the air outlet (x = 0.0 mm) than the fuel outlet (x = 19.0 mm).

The solid temperature distribution in the electrode-electrolyte across the y-direction is presented in Figure 4.20. The temperatures shown were obtained from the section corresponding to the maximum temperature (x = 8.4 mm). Unlike the activation overpotentials, the noticeable changes in the solid temperatures were observed between the flow channels (y = 0–0.05 mm). This was the area where the gas constituents diffused directly through the electrodes to react at the active interfaces. Therefore, large temperature differences observed in this region were contributed by the heat generated from the electrode reactions. The temperature difference across the anode was larger than that across the cathode due to the greater anode thickness.

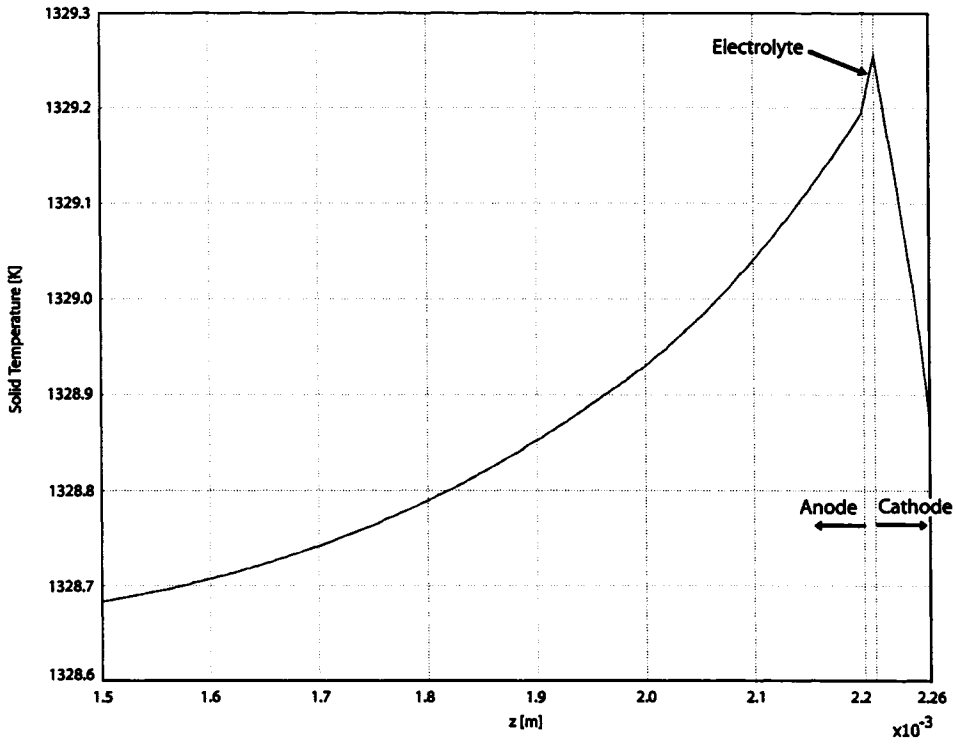

Figure 4.18: Solid temperature across the electrodes and electrolyte (x = 9 mm, y = 1 mm) for 49% H_2 fuel at 0.8 A/cm^2.

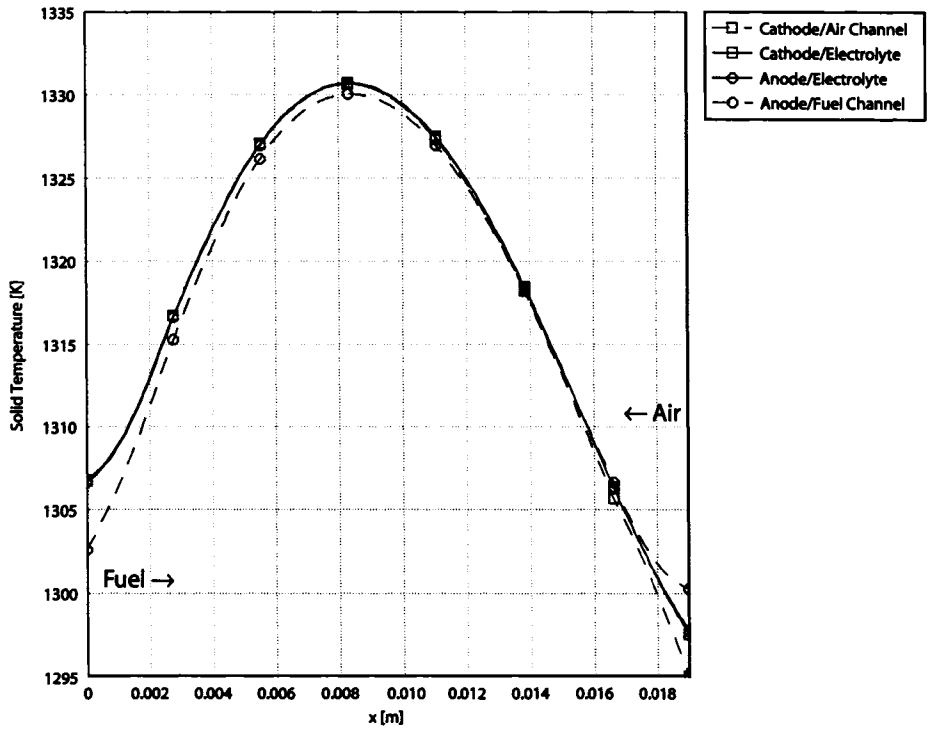

Figure 4.19: Cross-sectional solid temperature at various interfaces along SOFC length (y = 0.25 mm) for 49% H_2 fuel at 0.8 A/cm^2.

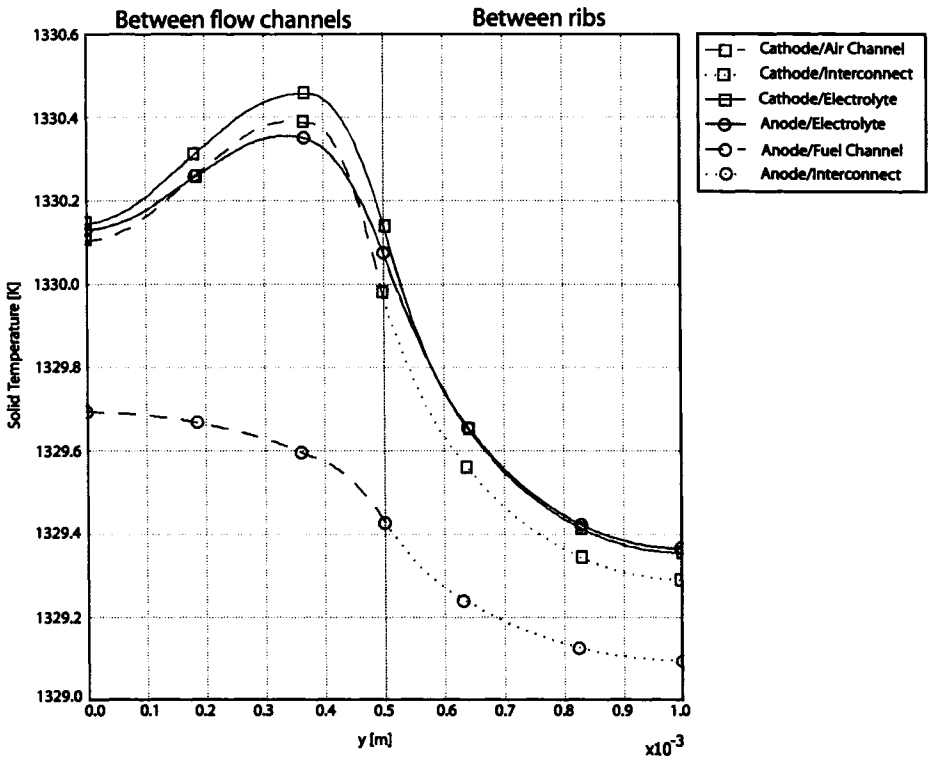

Figure 4.20: Cross-sectional solid temperature at various interfaces along SOFC width (x = 8.4 mm).

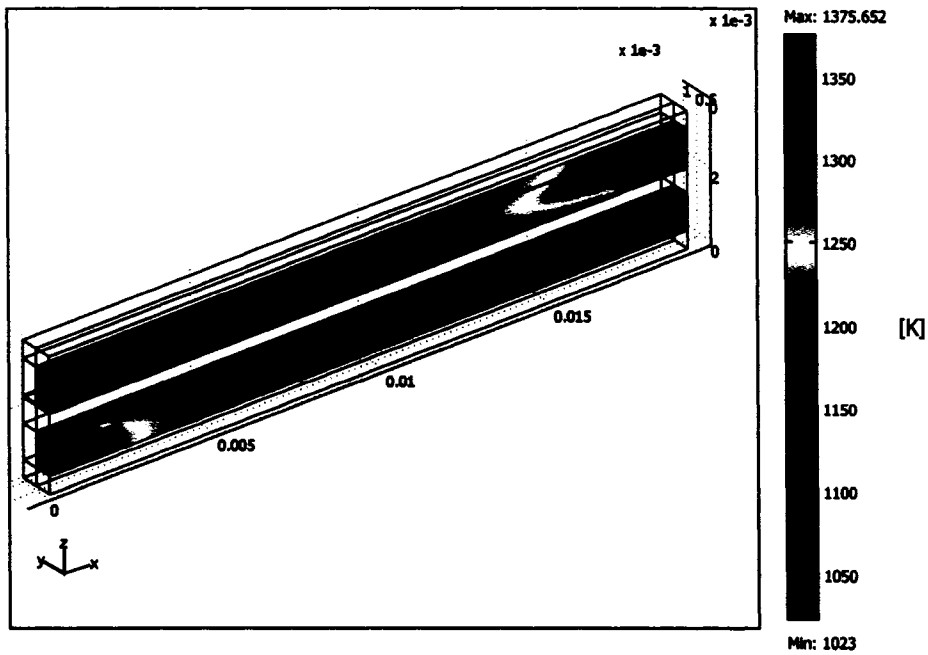

Figure 4.21: Fluid temperature in the gas channels for 49% H_2 fuel at 0.8 A/cm^2.

Fluid Temperature The temperature of gases in the flow channels is shown in Figure 4.21. The inlet temperatures were specified to be 1,023 K. The outlet air and fuel temperatures were found to be 1,314 K and 1,298 K, respectively. It was evident that the greater temperature gradient of the air stream resulted from the heat of cathode half-cell reaction.

4.3.2 Steady-state Model Validation

The steady-state simulations were performed using five different fuel compositions. The results from the simulations were compared to the data from experiments conducted by Keegan et al. (2002) [29]. The test cell consisted of 500μm-Ni/YSZ anode, 10μm-YSZ electrolyte, and 40μm-LSF cathode with the active cell area of 3.8 cm^2. The fuel and air flow rates were 200 cm^3/min and 300 cm^3/min at standard condition, respectively. The performance curve was generated at the operating temperature of 1,023 K with the fuel compositions of 10%, 24%, 49%, 73%, and 97% hydrogen. The inlet water concentration was maintained at approximately 3 mol%, and the fuel gas was then diluted with nitrogen. The oxidant used in their study was air. The experimental cell voltage at various fuel concentration is shown

in Figure 4.22. By comparing the simulation results in Figure 4.2 with Figure 4.22, it was observed that the predicted voltage curve has similar shape to that of the experimental data. Although the limiting currents did not agreed well with each other, the predicted voltages showed similar tailing effects at high current densities.

Although the operating conditions were similar to the model setup, the experiment was conducted on a button cell type which had a different geometry than the proposed model. Because of the difference in the geometry, the modelling results would not fully represent the experimental results from the button cell. However, the purpose of this thesis was to develop a dynamic model for the process control. For that reason, the validation goal was not to precisely fit the experimental data, but rather to capture the overall trend of the fuel cell performance curve. Additionally, the exact match between the model and the experiment was not required in the development of controllers, since the presence of feedback control would compensate for the model error. In controller design, it is essential that the process be stable under a normal operation. The stability of the process was presented in the previous section where it was shown that the output voltage decreased with increasing current density. By having an uncontrolled process, the output voltage was guaranteed to take a finite value between zero and the open circuit voltage. Therefore, the controller stability would be attainable even when model errors existed. For this reason, the modelling results were compared to the experimental results for qualitative purposes. The numerical comparison between the simulated data and the experimental data are tabulated in Table 4.2.

Table 4.2: Comparison of the simulated results with the experimental results from Keegan et al. [29].

H_2 Mol fraction	Maximum deviation (V)	Percent of maximum deviation	Average of percent difference
97% H_2	0.08	10.3%	5.8%
73% H_2	0.10	17.3%	4.9%
49% H_2	0.09	13.8%	3.2%
24% H_2	0.16	22.9%	12.5%
10% H_2	0.16	26.0%	12.4%

Large absolute deviations in the predicted voltage from the experimental values were observed for the fuel with 10% and 24% hydrogen. These deviations occurred as the op-

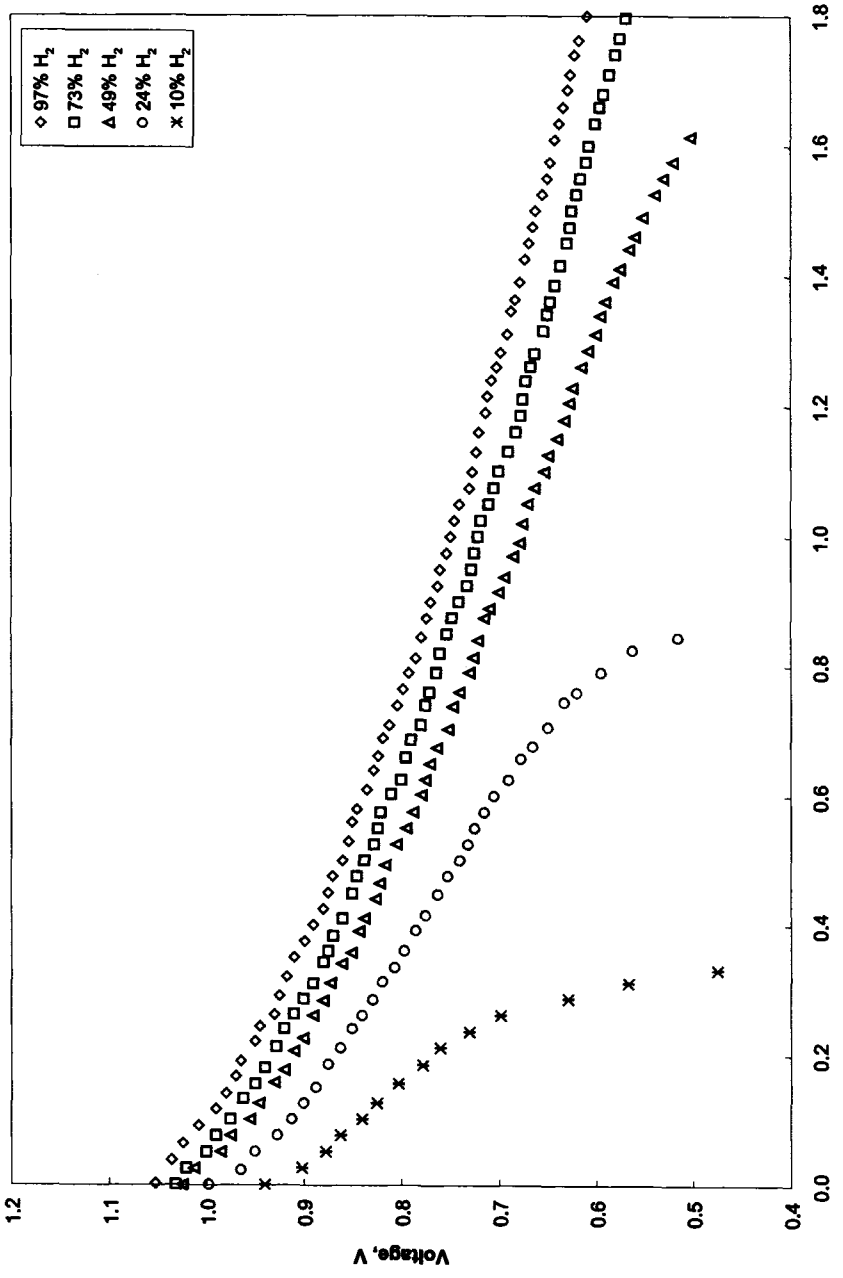

Figure 4.22: The experimental cell voltage as a function of current density at 750°C [29].

eration approach the limiting current densities. Although the performance curve contained the same trend at low hydrogen concentration, the mismatch in the limiting current density contributed to large maximum deviations. The smallest absolute deviation was obtained for 97% hydrogen fuel. On average, the predicted voltages for the SOFC operating with 49% hydrogen fuel agreed best with the experimental values. Overall, the simulated voltages at various fuel concentrations were within the same magnitude with those from the experiment, with the maximum percent discrepancy of 12.4% for the case of 10% hydrogen fuel. The main contribution to the discrepancy was the model parameter errors. The parameters used in the model were collected from various sources. Additionally, the existing parameters from open literature were found in wide ranges. The difference in the component thicknesses and the cell geometry between the proposed model and the experiment was a major contribution to the overall discrepancy.

4.3.3 Mass Balance Verification

The mass balance analysis was performed on the steady-state solution obtained from the fuel with 49% hydrogen, 3% water, and 48% nitrogen. The corresponding current density of 0.8 A/cm^2 was specified. The summary of the component balance is shown in Table 4.3.

Table 4.3: Summary of the component balance in the steady-state analysis.

Component		Inlet mass flow rates (kg/s)	Outlet mass flow rates (kg/s)	% Difference
Anode	H_2	7.42×10^{-9}	5.99×10^{-9}	N/A
	H_2O	3.85×10^{-9}	1.81×10^{-8}	N/A
	N_2	1.00×10^{-7}	9.99×10^{-8}	0.29%
Cathode	O_2	7.51×10^{-8}	6.14×10^{-8}	N/A
	N_2	2.47×10^{-7}	2.69×10^{-7}	8.85%
Total		4.34×10^{-7}	4.54×10^{-7}	4.75%

The discrepancy between the total inlet and outlet gas streams were 4.75%. This difference was numerically acceptable and could potentially be accounted for by numerical error. By refining the mesh, this error can be mitigated. Although the presence of nitrogen of both electrodes did not affect the electrochemical reaction, the mass balance analysis showed that nitrogen at the cathode was not conserved. This could be explained by examining how

nitrogen was calculated in the mass balance equation. The mass fraction of oxygen was calculated using the Maxwell-Stefan equation, and the mass fraction of nitrogen was calculated from 1-w_{O_2} (see Section 3.4.3 in Chapter 3). When the oxygen was consumed, less oxygen mass fraction would thereby increase the nitrogen mass fraction. The discrepancies in the nitrogen balance could be caused by this calculation.

The gas consumptions and generation of are tabulated in Table 4.4. The relative percent differences between the theoretical hydrogen and oxygen consumption compared with those from simulation were 2.24% and 1.56%, respectively. These discrepancies were acceptable and the mass balance analysis was verified. For the proposed model, the fuel and air utilizations of 19.2% and 18.3% were obtained for 49% H_2 fuel and air under the load current of 0.8 A/cm^2.

Table 4.4: Summary of the simulated and theoretical reactant consumptions and product generation.

Component		Simulated flow rate (kg/s)	Theoretical flow rate (kg/s)	% Difference wrt. inlet flow rate
Anode	H_2 consumption	1.42×10^{-9}	1.59×10^{-9}	2.24%
	H_2O generation	1.42×10^{-8}	1.42×10^{-8}	1.06%
Cathode	O_2 consumption	1.38×10^{-8}	1.26×10^{-8}	1.56%

4.4 Dynamic Analysis

To study the SOFC dynamic performance, an initial steady-state operating conditions must be defined. Selecting the operating conditions for the SOFC is often not a trivial process. To achieve the maximum power output, many trade-offs are involved. From the current-voltage characteristics, the maximum power can be supplied by fuel cell in a medium to high voltage range. SOFC are normally designed to operate within a voltage range of 0.6 V to 0.7 V, although higher or lower voltage are acceptable [9]. This range of voltages may not yield the highest power supply, but it provides a stable operation and consistent cell efficiency. Operating in the current density range near the limiting current could result in high power generation but low efficiency. In the high current region, the reactants utilization

increases with the increasing current. However, the sharp drop in the cell voltage is caused by diffusion limitation, making this condition uneconomical.

4.4.1 Nominal Operating Condition

From the steady-state model validation, it was observed that the predicted cell performance for 49% hydrogen fuel contained the least discrepancies when compared with the literature data. The model was able to predict acceptable cell voltages in the current density range of 0.2 A/cm^2–1.0 A/cm^2. To operate the SOFC within the designed voltage range, the operating current density of 0.8 A/cm^2 was chosen. This current density corresponded to the cell voltage of 0.743 V. Therefore, 49% hydrogen fuel and the load current density of 0.8 A/cm^2 were chosen as a nominal operating condition in the dynamic SOFC model. By choosing to operate around this nominal condition, the optimum performance can be achieved by operating at higher current density or increasing the molar fraction of hydrogen. Summary of nominal operating conditions for used in dynamic simulation is given in Table 4.5.

Table 4.5: Summary of nominal SOFC operating condition for the dynamic model.

Parameter	Value
Inlet gas temperature, T	1,023 K
Operating pressure, P	1 atm
Nominal voltage, $\bar{V}$	0.743 V
Range of operating voltage, V	0.7 V–0.8 V
Nominal current density, $\bar{J}$	0.8 A/cm^2
Range of operating current density, J	0.7 A/cm^2–0.9 A/cm^2
Nominal inlet hydrogen concentration, $\bar{x}_{H_2}$	49%
Range of inlet hydrogen concentration, x_{H_2}	38%–60%

In transient operations, the SOFC were often subjected to sudden changes in the load resistance. Consequently, this resulted in changes in the power demand which required varying current density from the fuel cell. In the dynamic model, a step function was used to represent the sudden change in the load current at an instantaneous time. The dynamic model was subjected to positive and negative step changes with different magnitudes in the load current density. The step changes were made within the range of operating condition envelope shown in Table 4.5. The dynamic response of the cell performance was then investigated.

Also, the effects of varying the molar fraction in hydrogen fuel was studied.

4.4.2 Dynamic Modelling Results

Step Changes in Load Current Density

Three step changes were made to the parameters of interest in the dynamic model: positive and negative step changes with the same magnitude, and a positive step change with a smaller magnitude. The load current density was varied from 0.8 A/cm^2 to 0.9 A/cm^2, 0.85 A/cm^2, and 0.7 A/cm^2. The hydrogen concentration in the fuel was maintained at the nominal value of 49%. The step changes in the load current density occurred at the time of 10 seconds. The corresponding output voltage and overall solid temperature responses to load step changes are presented in Figure 4.23. The temperatures shown were obtained from the average temperature over the cathode-electrolyte interface where maximum temperatures were expected. It was seen that the voltage responded immediately to the change in load demand according to Ohm's law. In Figure 4.23(a), a small inflection point in the voltage response was observed after the load current was increased from 0.8 A/cm^2 to 0.9 A/cm^2. This small dip in the solution occurred as a result of a numerical error caused by a discontinuity in time. Small dynamic effects were observed and the response time for the output voltages to reached new steady-states were approximately 330 seconds. The dynamic response provided the steady-state gain information which can be used to develop a simplified model. The gains, K_L were calculated from changes in the output voltage with respect to changes in the load current at the final steady-states.

$$K_L = \frac{\Delta V}{\Delta J_{load}} \tag{4.1}$$

The steady-state gains, K_L, are summarized in Table 4.6. It was observed that the gains were consistent for the positive step changes in the load current. However, the gain from the negative step change was approximately 10% lower. The slight inconsistency in the steady-state gains indicated that the effect of load change on the output voltage was nonlinear in this operating region.

In Figure 4.23(b), it was shown that the solid temperature had the largest response time of approximately 400 seconds. The cell temperature had a substantial effect in the transient

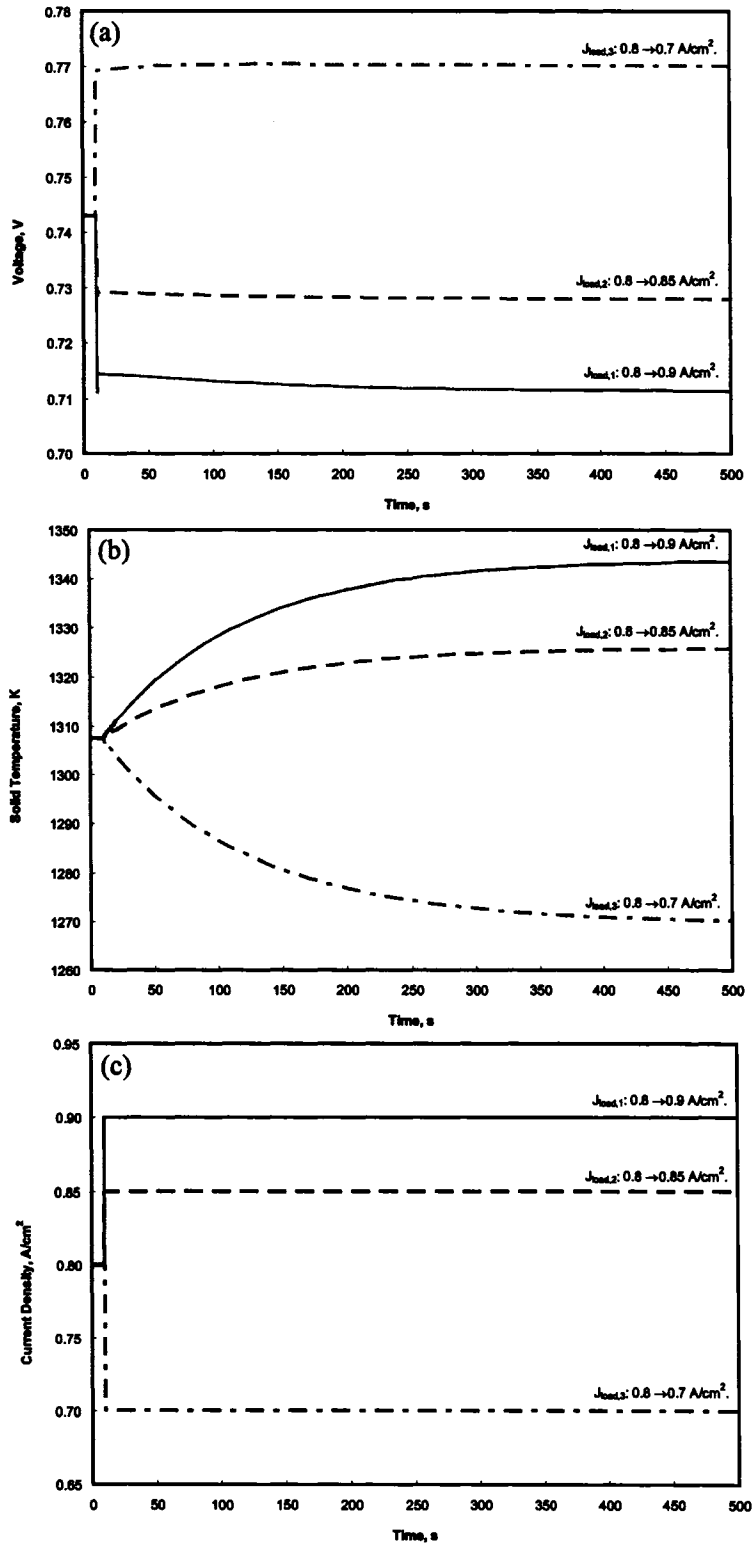

Figure 4.23: Output voltage responses (a) and the temperature responses (b) to step changes in load current densities (c).

Table 4.6: Steady-state gains in the output voltages with respect to the load step changes.

Final load current density, A/cm^2	Final output voltage, V	Steady-state gain (K_L), Ωcm^2
0.90	0.711	-0.315
0.85	0.728	-0.302
0.70	0.770	-0.271

operation of SOFC. Although the overall voltages were not significantly influenced by the temperature distribution, the material stresses could potentially be a problem. The largest temperature increase of 36 K was obtained from the load change from 0.8 A/cm^2 to 0.9 A/cm^2. At such a large temperature gradient, the stresses would likely be developed. A complete thermal stress analysis must be perform the investigate the effect of temperature gradient on the material stresses.

Figure 4.24 shows the time responses of the anode and cathode activation overpotentials with respect to load step-changes from 0.8 A/cm^2 to 0.9 A/cm^2, 0.85 A/cm^2, and 0.7 A/cm^2. Although the change in the overall cell voltage were instantaneous, the activation overpotentials were substantially dependent on the temperature dynamics. The overshoots in the overpotential responses were observed for both the anode and cathode. It was known that the overpotentials represented the kinetics of the electrode reactions. Thus, the activation overpotentials were critically associated with the solid temperature at the reactive sites. Figure 4.25 shows the outlet gas concentration responses to load step changes. By increasing the load current, the reactant utilizations were increased. This was observed in the concentration profiles of the reactants in the presence of the positive load changes. As the load current was increased, more hydrogen and oxygen were consumed, and vice versa. Although, the concentrations changed instantaneously, some dynamic effects were observed. The response time of approximately 250 seconds in the change in oxygen flux was more noticeable than those of the hydrogen and water.

Step Changes in Hydrogen Molar Fraction

Figure 4.25 shows the dynamic responses of the outlet gas to step changes in the inlet hydrogen concentration from 49% to 60%, 55%, and 38%. The load current density was kept at its nominal value of 0.8 A/cm^2. The step tests in the hydrogen molar fraction were introduced at

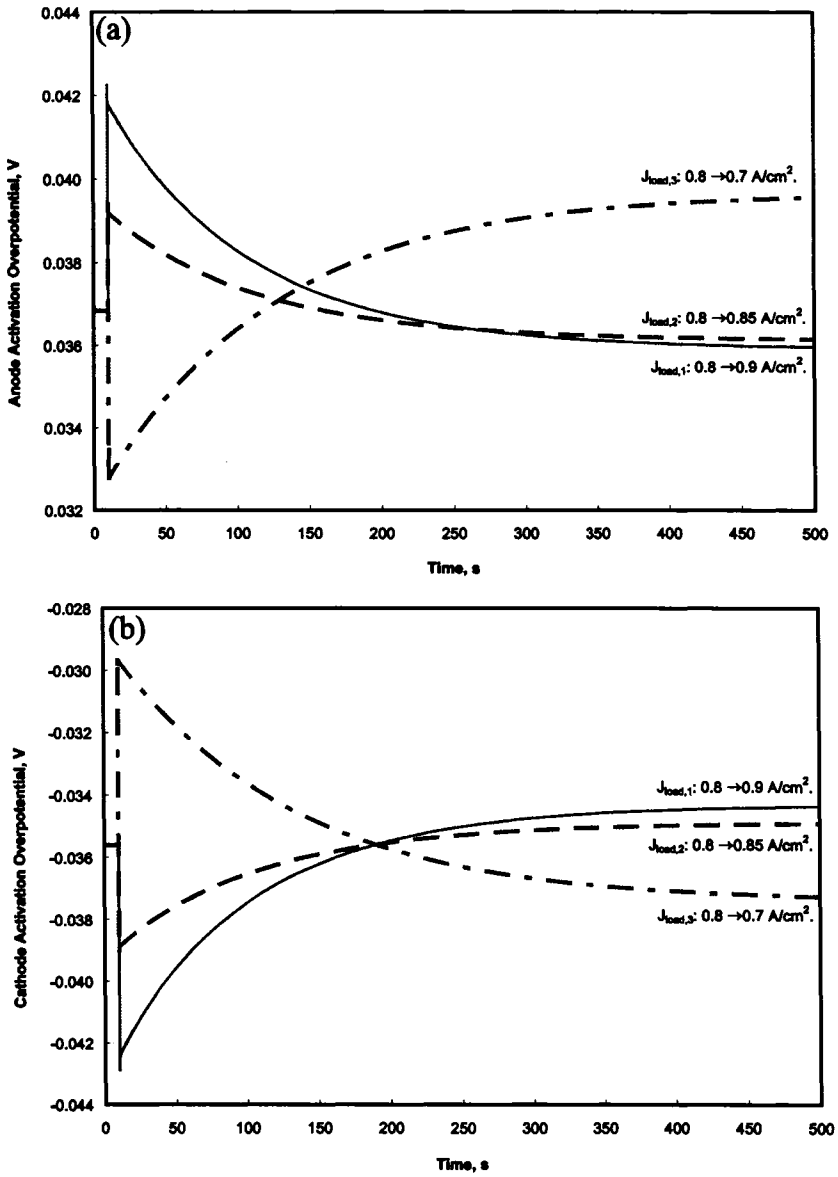

Figure 4.24: Time responses of the anode (a) and cathode (b) activation overpotentials to step changes in load current densities.

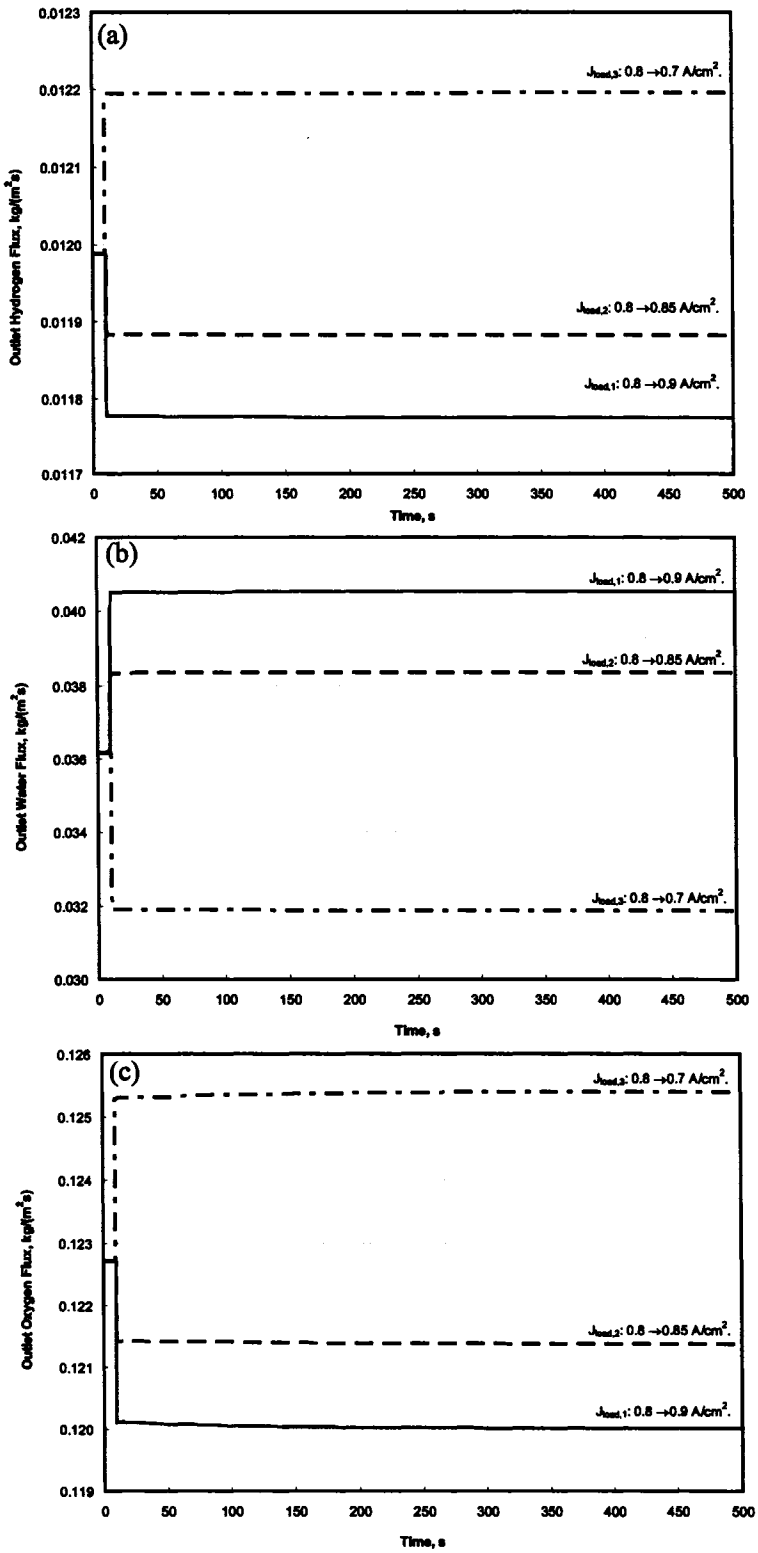

Figure 4.25: Time responses of hydrogen (a), water (b), and oxygen (c) outlet mass fluxes to step changes in load current densities.

10 seconds. The temperature responses were obtained from the overall solid temperature at the cathode-electrolyte interface. When the hydrogen concentrations were step changed, the sudden changes in the voltage were observed. The dynamic effects in the voltage changes were unnoticeable. The steady-state gains, K_P, were calculated for the changes in the cell voltage with respect to changes in hydrogen molar fractions.

$$K_P = \frac{\Delta V}{\Delta x_{H_2}} \tag{4.2}$$

A summary of the steady-state gains, K_P, is provided in Table 4.7. The gains for the positive step changes in hydrogen concentration were consistently in agreement with one another. However, the negative step change in hydrogen produced a larger gain twice the magnitude of the expected gain result. This was indicative that the nonlinear effects were present in this operating condition. For control design purposes, the output voltage can be difficult to control in this region with low hydrogen molar fraction.

Table 4.7: Steady-state gains in the output voltages with respect to the changes in the inlet hydrogen compositions.

Final molar fraction of hydrogen, %	Final output voltage, V	Steady-state gain (K_P), V/%
60%	0.780	0.334
55%	0.765	0.365
38%	0.675	0.622

In Figure 4.26(b), the response time of the temperature change of approximately 400 seconds were observed in all cases. By increasing the hydrogen content, a lower temperature was observed. This could be responsible by the change in the activation overpotentials shown in Figure 4.27. It was seen that the dynamic effect of hydrogen concentration change was more profound on the cathode overpotential than the anode overpotential. Initially, the overshoot in the cathode activation overpotential was observed when the change in the hydrogen content was introduced. However, the cathode activation overpotential then decreased below the original value as the new steady-state was obtained. The heat sources along the electrode-electrolyte boundaries were calculated from the entropic (reversible) and the activation (irreversible) heat effects. Since the current was maintained constant, the change in the entropic heat became less significant and the heat source was more dependent

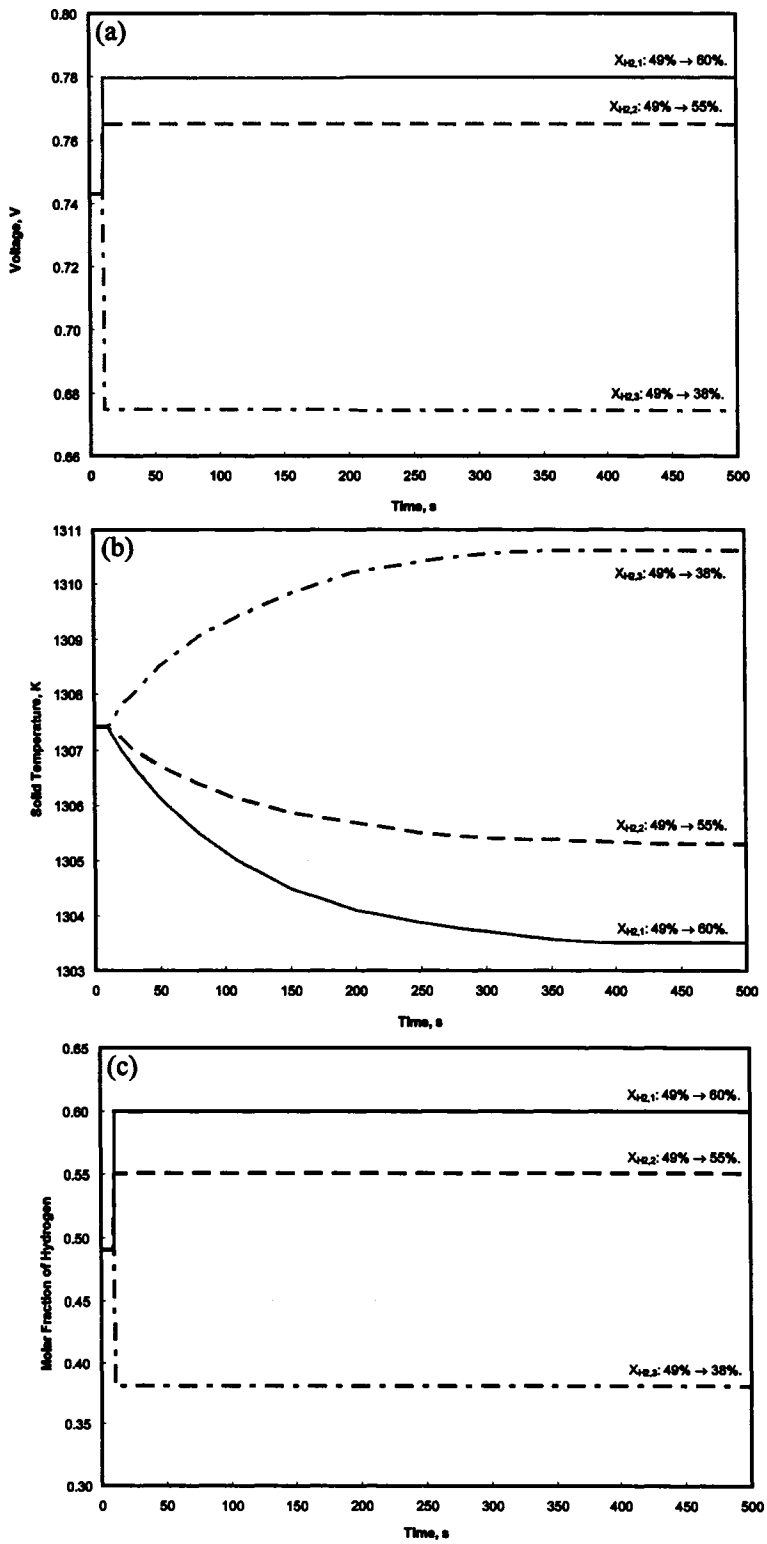

Figure 4.26: Output voltage responses (a) and the temperature responses (b) to step changes in inlet hydrogen molar fractions (c).

Table 4.8: Comparison of the dynamic modelling results at 750°C and 0.8 A/cm^2 with the interpolated results from Keegan et al. [29].

H_2 Molar fraction	Final steady-state voltage (V)	Interpolated voltage (V) [29]	Percent difference
60% H_2	0.780	0.746	4.48%
55% H_2	0.765	0.738	3.60%
38% H_2	0.674	0.694	2.88%

on the activation overpotential term. When both of the anode and cathode activation overpotentials were reduced, less irreversible heat effect was generated and the temperature was lowered as a result. The dynamic responses of the outlet gas concentration to changes in hydrogen concentrations are illustrated in Figure 4.28. The dynamic effects were not observed. However, the overshoots in the outlet water mass flux were observed right after step changes were introduced. The numerical errors could be responsible for these overshoots. The errors were likely generated by the discontinuity in time when the step changes were introduced. By simulating the dynamic model using a smaller time increment, this numerical errors can be avoided.

4.4.3 Dynamic Model Validation

The results from the dynamic model were validated with the interpolated data from the experiment by Keegan et al. [29]. From the experimental results, the voltages were determined for the hydrogen molar fraction of 38%, 55%, and 60% in the fuel using linear interpolation. The interpolated data are plotted against the experimental results as shown in Figure 4.29.

The final steady-state output voltages obtained from the step change in the inlet hydrogen molar fraction were compared with the interpolated data. The validation results are tabulated in Table 4.8. It was observed that, the overall results were in agreement with the experimental data. The maximum voltage difference of 4.48% were obtained from 60% hydrogen fuel. It was confirmed that the dynamic model produced a physically reasonable result. This detailed model gave insightful information on the dynamic characteristics of the SOFC. It also provided a foundation for further control strategies, which will be discussed in the next chapter.

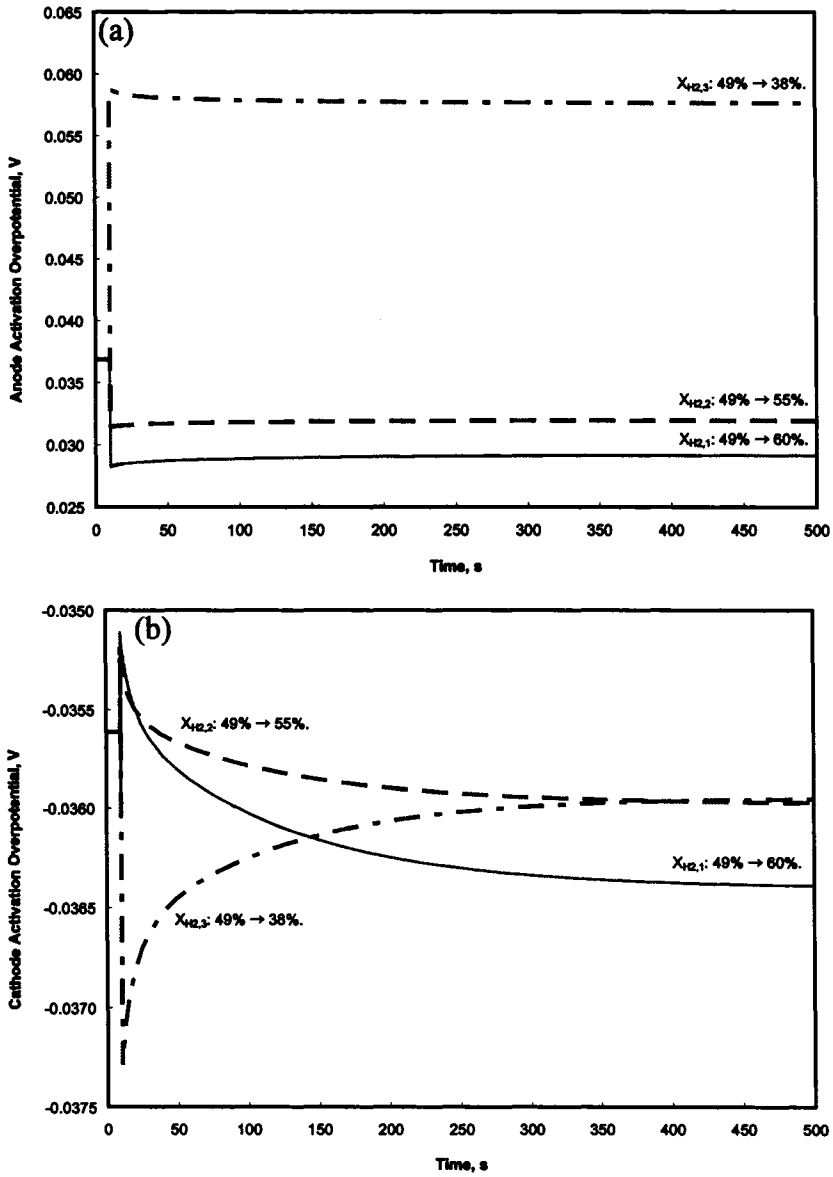

Figure 4.27: Time responses of the anode (a) and cathode (b) activation overpotentials to step changes in inlet hydrogen molar fractions.

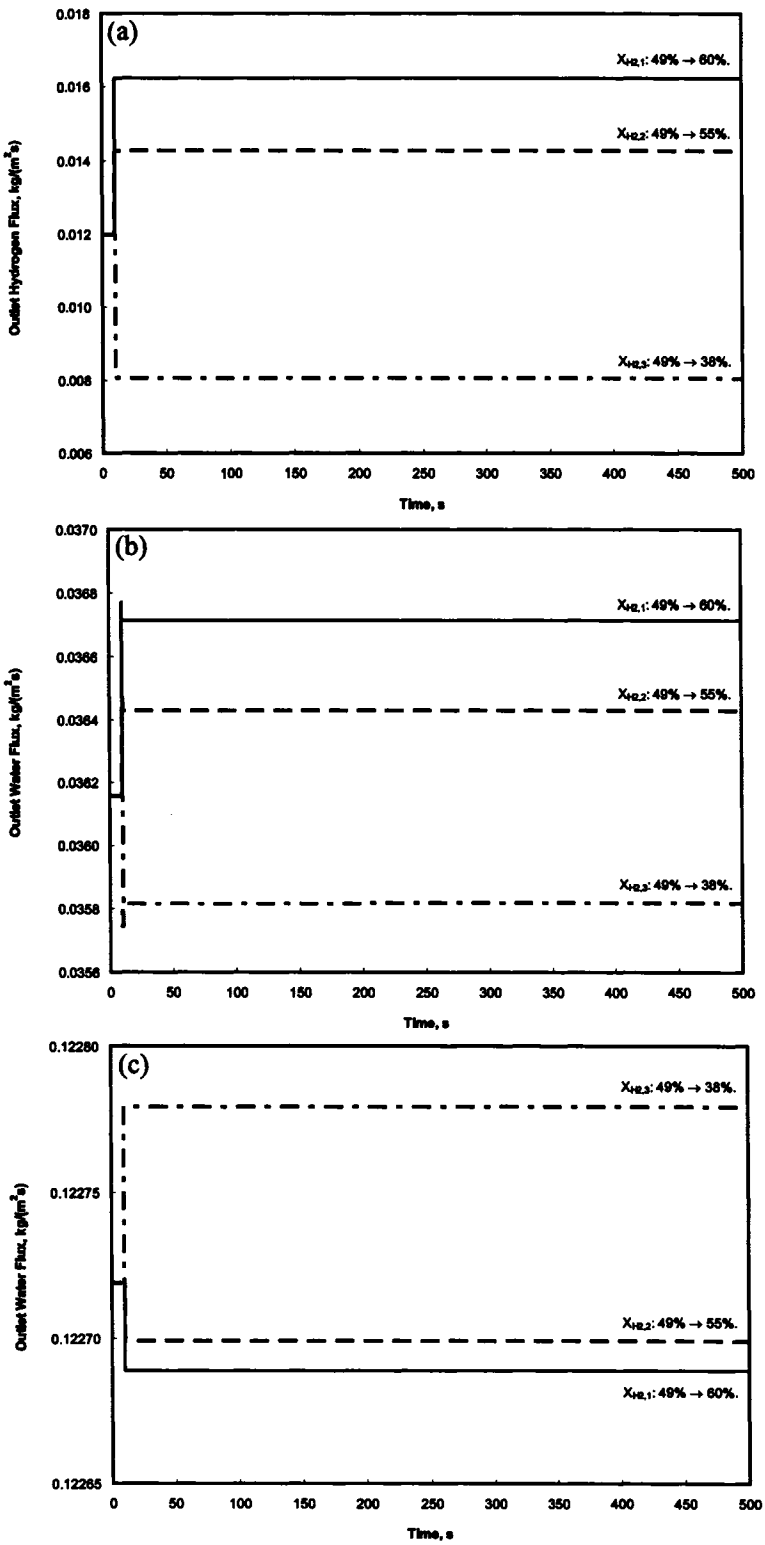

Figure 4.28: Time responses of hydrogen (a), water (b), and oxygen (c) outlet mass fluxes to the step changes in inlet hydrogen molar fractions.

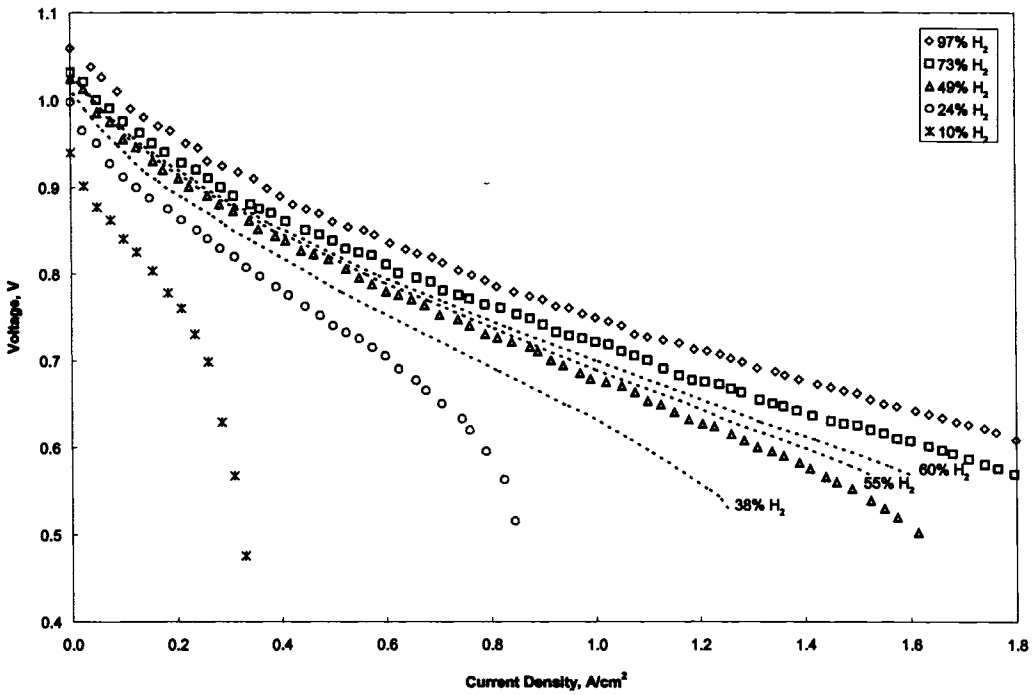

Figure 4.29: Interpolation of cell performance curve for 38%, 55%, and 60% hydrogen fuel.

Chapter 5

Process Control of SOFC

5.1 Introduction

A comprehensive dynamic model allows for the performance prediction of the SOFC under transient operations. It also provides an insightful information into the dynamic characteristics and control system performance. The results obtained from the physically-based models often provide the most accurate analysis on the dynamic behaviour. However, substantial computer effort is required to demonstrate control testing on such a model with high level of complexity. To determine the effects of various control settings in an early stage, low-order dynamic models based on simple transfer functions can be developed. The controller design can be carried out on the simplified models which are capable of representing the main dynamic properties of the system. These transfer function models can also provide insight to the limitation of the control system without demanding substantial engineering effort in the development stage.

In practice, SOFC are often subjected to load changes which result in voltage drops. Therefore, the load current can be accounted for as a disturbance to the SOFC system. By increasing the composition of hydrogen in the fuel, the cell voltage can be restored. In this chapter, first-order transfer functions are derived from the dynamic step responses of the SOFC to represent the relationship between the output voltage, load current, and the fuel composition. The control objective is proposed to maintain the output voltage despite changes in the load current. The approach to control the voltage using feedback PI controllers is demonstrated and the limitation of the control system is discussed.

5.2 Low-Order Dynamic Model

For the control of SOFC in the present study, it was specified that two input variables are for the change in the overall cell voltage. The inlet hydrogen concentration and the load current density are chosen as the input variables for this study. Two low-order models are developed such that the dynamic responses of the output voltage are described by the transient changes in each input variables. A block diagram illustrating the SOFC system with two process models is shown in Figure 5.1. The blocks G_P and G_L represent the process models for the

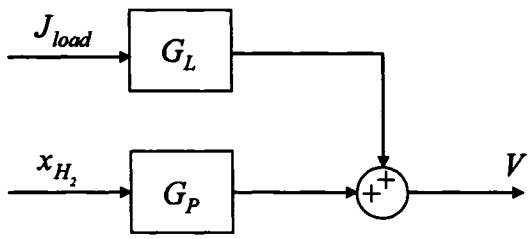

Figure 5.1: Block diagram of the SOFC system with two process transfer functions.

output voltages with respect to the input variables, which are the hydrogen content and the load current, respectively. The process model can be described using the Laplace transfer function to represent the dynamic response in the time-domain. The process input and output can be related using the process transfer functions [44];

$$G_P(s) = \frac{K_P}{\tau_P s + 1} \tag{5.1}$$

$$G_L(s) = \frac{K_L}{\tau_L s + 1} \tag{5.2}$$

Here, $G_P(s)$ and $G_L(s)$ are the transfer functions for the process and the disturbance, respectively. The process transfer function, $G_P(s)$, has the unit of V/%H_2. The disturbance transfer function, $G_L(s)$, carries the unit of V/(A/cm^2) or Ωcm^2. The process and disturbance gains, K_P and K_L, represent the steady-state gains with respect to the change in the corresponding input variables. The parameters τ_P and τ_L are the time constants of the pro-

cess and the disturbance, respectively. These parameters in the transfer function model can be derived from the dynamic step response to the input variables.

To determine the parameters for the transfer function models, the steady-state gains information reported in Chapter 4 were revisited. It was observed that the nonlinear effect of changes in the inlet hydrogen concentration on the output voltage was more prominent in the low concentration region. It was difficult to control the voltage within this region since the nonlinear effect could not be accurately accounted for in the first-order transfer function model. For the purpose of control simulation, the steady-state gain of 0.334 V/% was chosen for K_P. This was the gain corresponding to the change in the hydrogen content from 49% to 60%. The steady-state gain of the voltage with respect to the load current of -0.315 Ωcm^2 were selected for K_L.

The process time constant represented the dynamic component of the output response. It was observed that the output voltage responded to the changes in the hydrogen content and the load current instantaneously. Since the dynamic components in the output responses were negligible, the process and disturbance transfer functions could be developed as gain-only models. However, the value of τ_P and τ_I were taken as 0.1 seconds to simulate various controller settings for the first-order transfer functions. These time constants were sufficiently small to provide an instantaneous voltage response. They also allowed for the dynamics of the controller responses to be observed. By substituting the selected parameters in Equation (5.1) and Equation (5.2), the process and disturbance transfer functions were obtained.

$$G_P(s) = \frac{0.334}{0.1s + 1} \tag{5.3}$$

$$G_L(s) = \frac{-0.315}{0.1s + 1} \tag{5.4}$$

The nominal operating conditions of these transfer function models were the same as those specified in the previous chapter. The SOFC was operated at 1,023 K and 1 atm with 49% H_2 fuel and was subjected to the load current density of 0.8 A/cm^2. The corresponding output voltage was 0.743 V. Since the transfer function models were derived from step changes around these conditions, the dynamic behaviours outside of this operating range would not be adequately captured by the simplified models. Due to nonlinearity of the SOFC system, new transfer functions must be obtained for different nominal operating conditions.

5.3 Feedback Control

Feedback control is one of the most commonly used control strategies. In feedback control, the actual output variable (y) is measured and the discrepancy between the actual and the desired set-point values (y_{sp}) is used to adjust the process input variable (u). The feedback control objective is to minimize the error signal, e.

$$e(t) = y(t) - y_{sp}(t) \tag{5.5}$$

Three basic modes of feedback control are proportional (P), integral (I), and derivative (D) control. According to the PID control algorithm, the controller output is the process input variable to be adjusted. The controller output, u, is calculated from the following relationship in time-domain [44]

$$u = \bar{u} + K_c \left[e(t) + \frac{1}{\tau_I} \int_0^t e(t)dt + \tau_D \frac{d(e(t))}{dt} \right] \tag{5.6}$$

where $\bar{u}$ is the nominal value of the process input. The nominal condition is often specified as the initial steady-state condition in control simulation. The controller tuning parameters, K_c, τ_I, and τ_D are the controller gain, integral time, and derivative time, respectively. They each represent the proportiona, integral, and derivative actions in the controller accordingly. The PID controller can be represented by the transfer function in s-domain

$$G_C = \frac{U(s)}{E(s)} = K_c \left(1 + \frac{1}{\tau_I s} + \tau_D s \right) \tag{5.7}$$

where $G_C(s)$ is the controller transfer function. $U(s)$ and $E(s)$ are the Laplace transforms of the controller output $u(t)$ and the error signal $e(t)$. These parameters are known as the PID controller tuning parameters which can be adjusted to produce the desired output response. In proportional control, a large value of K_c is required to achieve perfect control. However, this also requires a high controller effort. Generally, the P-only control yields steady-state errors that occur after a change in the set-point or the disturbance. This offset can be eliminated by incorporating the integral action τ_I in the PI controller. For the case where significant dynamic effects are observed, the presence of the derivative control action often improves the settling time of the system.

In this study, the control objective was to maintain the output voltage despite changes in the load current. The controlled variable was the output SOFC voltage, and the manipulated

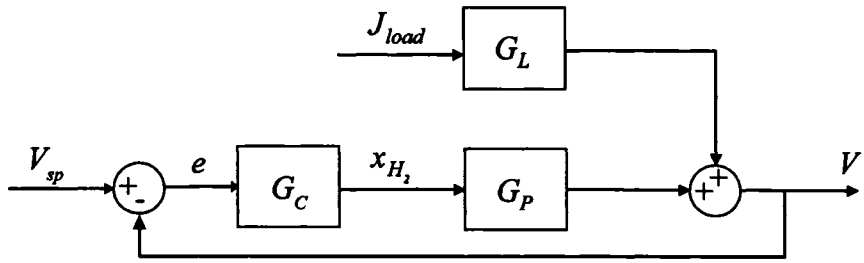

Figure 5.2: Block diagram for the SOFC system with feedback control.

variable was the inlet hydrogen molar fraction in the fuel. The load current density was specified as the disturbance to the SOFC. The desired set-point voltage was maintained at its nominal voltage. The PI controller was implemented in the voltage control loop. The derivative term was omitted due to the lack of dynamic effects on the voltage responses of the SOFC. The block diagram illustrating a closed-loop SOFC system with a feedback controller is shown in Figure 5.2. The open-loop representation of the SOFC in this work was given in the previous section (Figure 5.1).

5.3.1 Closed-loop SOFC System Response

The voltage controller for the SOFC system was implemented in Matlab Simulink [2]. The Simulink diagram of the open-loop process and the closed-loop feedback control is shown in Figure 5.3. The limiting bounds were set on the PI controller output such that the inlet hydrogen molar fraction of the fuel was within 0% to 100%.

The closed-loop voltage control simulation were first subjected to various proportional controller settings. The step change in load current from 0.8 A/cm^2 to 0.9 A/cm^2 was introduced at 10 seconds. The set-point voltage was specified at 0.743 V, which was the initial voltage for the SOFC system operating with 49% hydrogen fuel and the load current of 0.8 A/cm^2. The closed-loop voltage responses and the controller output responses obtained from various proportional control settings are shown in Figure 5.4. The controller parameters were selected to investigate the control effects on the closed-loop system. They were not comprehensively tuned to achieve the optimum controller performance. From Figure 5.4(a), it was observed that the uncontrolled (open-loop) voltage dropped instantaneously after the change in the load current was introduced. With the controller, the output voltage was brought

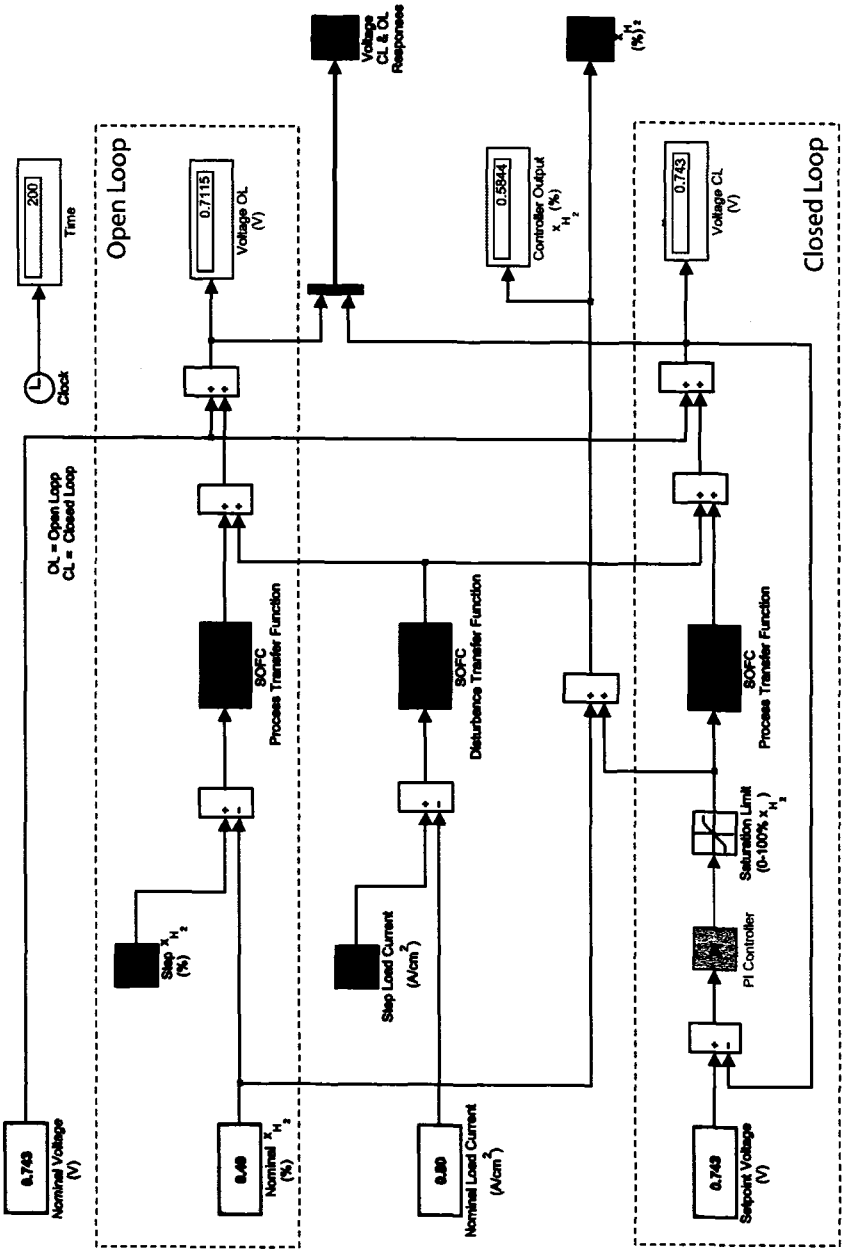

Figure 5.3: Open-loop and closed-loop feedback control diagram in MATLAB Simulink.

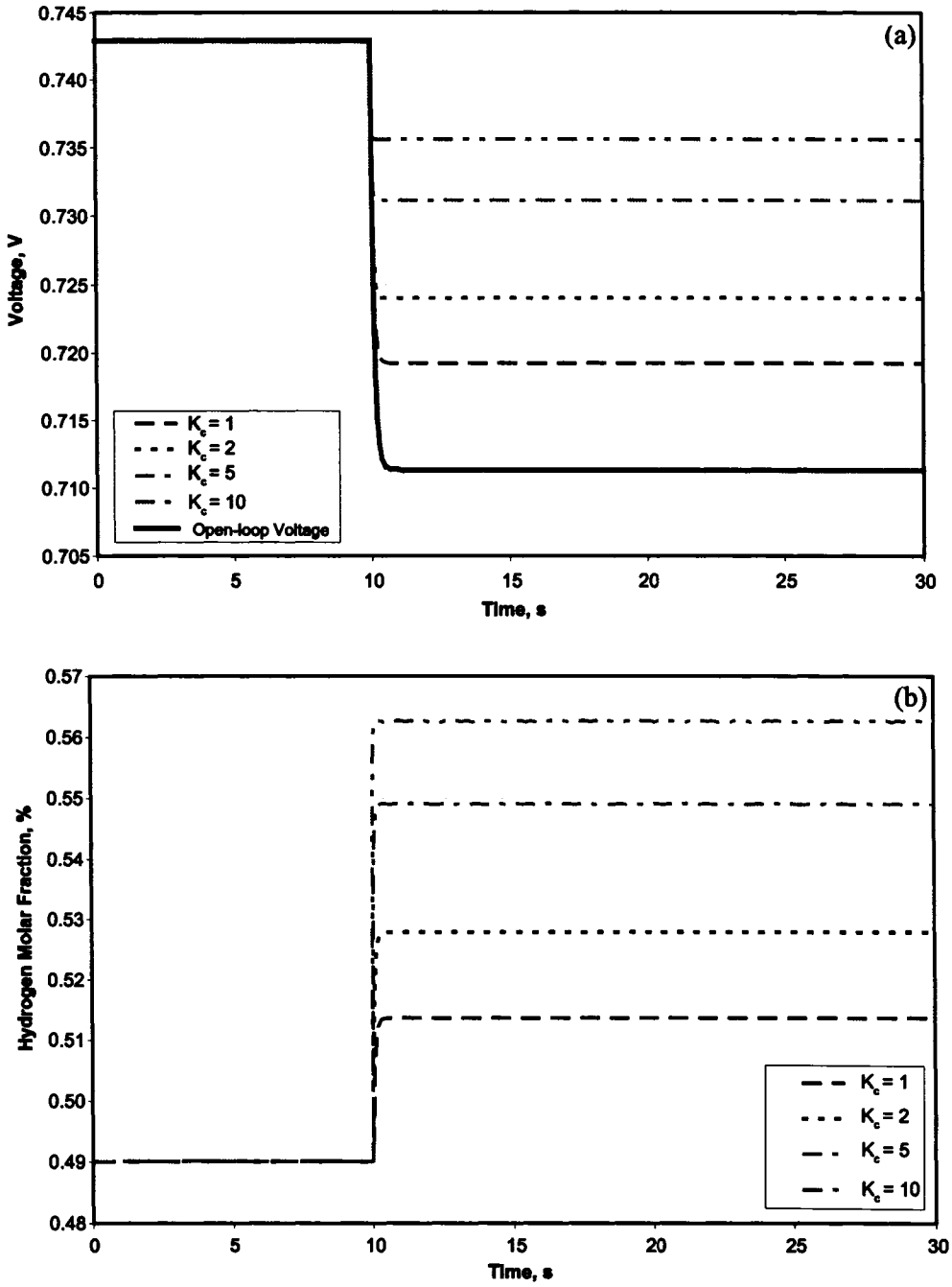

Figure 5.4: Closed-loop voltage responses (a) and controller output responses (b) for the proportional control settings.

closer to the desired voltage. However, the offsets between the steady-state and the set-point voltages were observed. This was the expected output response from the process with proportional control. The controller output was calculated from the product of the controller gain (K_c) and the offset (e). Therefore, the presence of the offset was always required to generate the output for the proportional controller.

By increasing the controller gain, the offset was reduced and a fast response to load change was obtained. However, large values of K_c created instability as observed in Figure 5.4(b). For the controller responses with K_c = 10 a slightly oscillatory voltage response was obtained. A proportional control with large controller gain would be undesirable since it may lead to an unstable operation.

The proportional plus integral (PI) controllers were implemented in the voltage control loop. The step changes in the load current from 0.8 A/cm^2 to 0.9 A/cm^2 at 10 seconds were simulated. The voltage responses for various PI controller setting and the controller output responses are presented in Figure 5.5. With the integral action, the steady-state offsets were eliminated and the desired set-point voltage was obtained. The dynamic voltage responses were reflected by the controller responses of the hydrogen molar fractions. The slow responses from the controller with lower integral time were observed. A robust control was obtained for the PI controller setting with a small controller gain K_c and a large integral time τ_I. It was observed that the controller settings of K_c = 1 and τ_I = 10 yielded the most robust controller performance.

The PI controller with the controller gain of 1 and the integral time of 10 seconds was used to maintain the output voltage in the control-loop under various load disturbances. At 10 seconds, the load disturbance was changed from its nominal value of 0.8 A/cm^2 to 0.85 A/cm^2, 0.7 A/cm^2, and 0.65 A/cm^2. The voltage responses and the controller output responses of the inlet hydrogen content are shown in Figure 5.6. After the load disturbances were introduced, the output voltages increased for the negative load changes, and vice versa. The PI controller successfully restored the output voltage to the desired set-point value after approximately 2 seconds. Therefore, the PI controller gave a satisfactory performance in rejecting the load disturbances. In Figure 5.6(c), it was observed that the PI controller responded to changes in the load disturbance by manipulating the controller output, i.e., the inlet hydrogen concentrations, such that the set-point value of the output voltage was re-

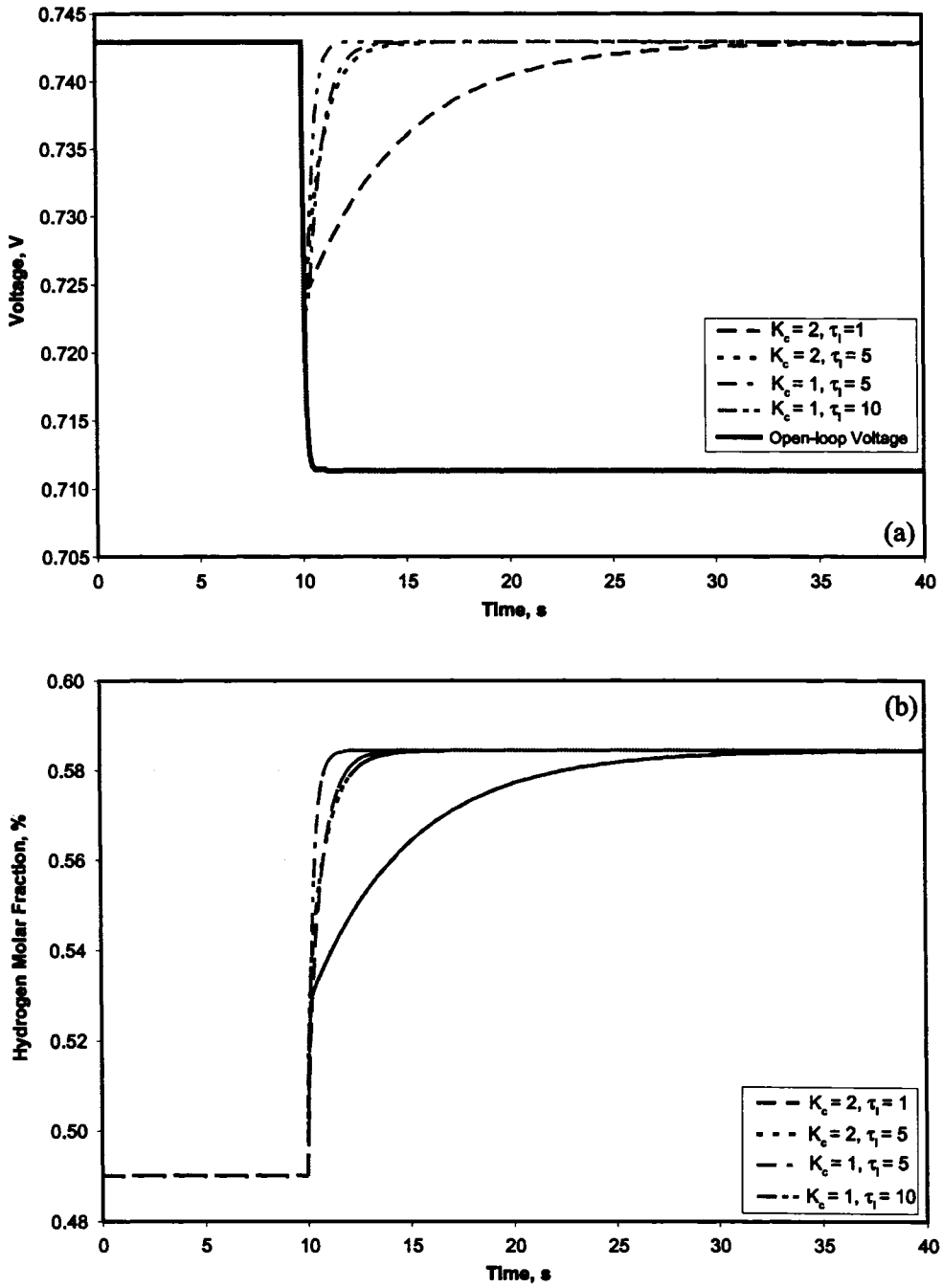

Figure 5.5: Closed-loop voltage responses (a) and controller output responses (b) for the proportional and integral control settings.

stored. For a positive change, the inlet hydrogen concentration was increased to obtained the desired output voltage. As seen from the figures, the range of hydrogen concentration of 35% to 54% were required to maintain the voltage of 0.743 V when the SOFC was subjected to the load current range of 0.65 A/cm^2 to 0.8 A/cm^2.

The feedback PI controller provided insightful information about the relation between the process outputs and the controller responses. It has been demonstrated that the low-order dynamic models developed from the physically-based model allowed for the implementation of controller design without involving a significant amount of computational effort. However, the simplified models must be used with caution when representing highly non-linear process such as the SOFC. Since the low-order models were derived under a specific operating range, the predicted cell performance obtained for a different operating region would be less accurate. When a new operating condition is specified as a nominal operating point, the low-order models must be reproduced from the detailed model accordingly.

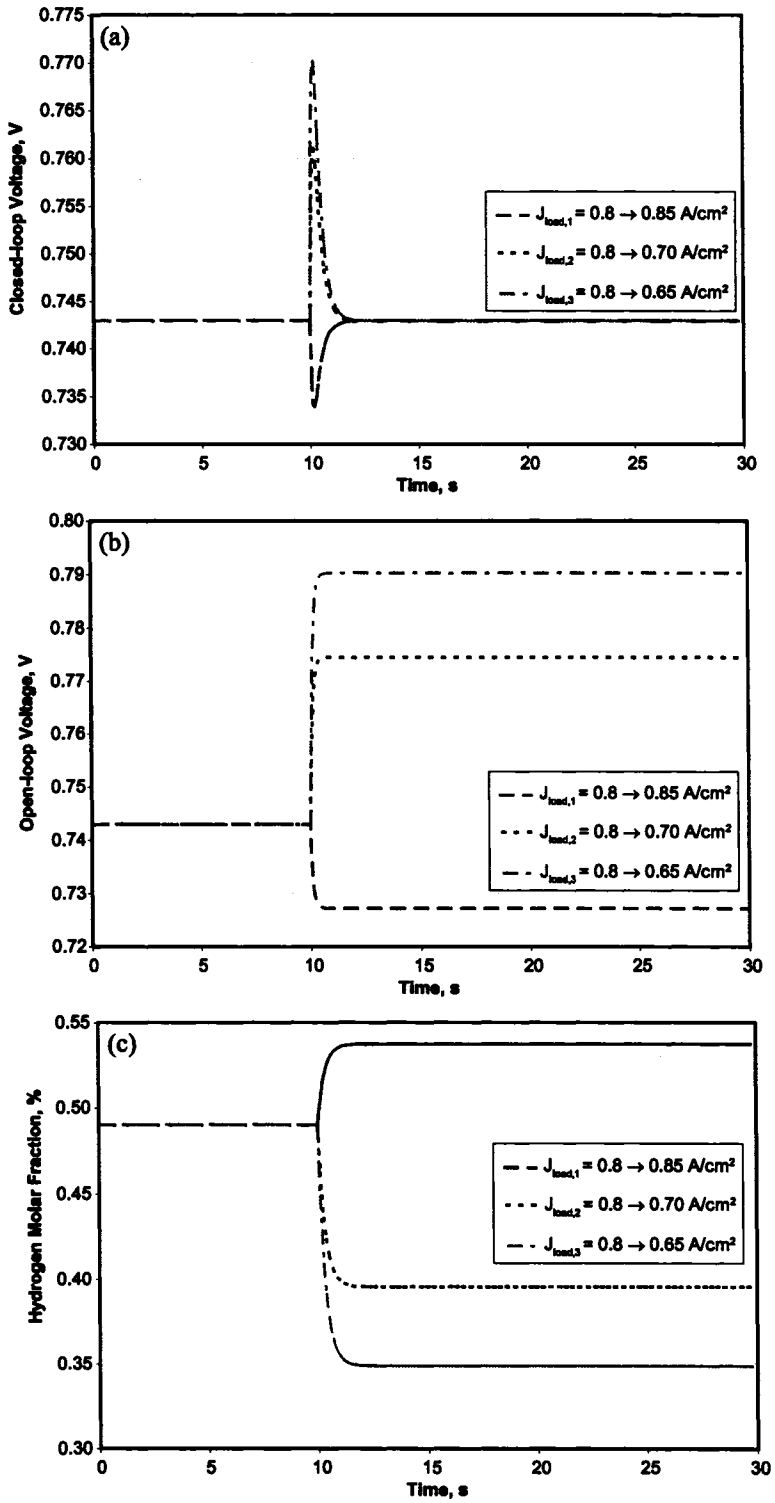

Figure 5.6: Closed-loop voltage responses (a), open-loop voltage (b), and controller output responses (c) under various load changes obtained from the PI controller settings: $K_c = 1$, $\tau_I = 10$ s.

Chapter 6

Conclusion

Through this research, a 3D dynamic model of an anode-supported planar SOFC has been presented. Theoretical principles underlying the electrochemical kinetics of fuel cells are first introduced in this thesis. The physically-based model has been developed from the conservation laws of charges, mass, momentum, and energy. The solutions have been obtained from the mathematical model consisting of partial differential equations. The steady-state cell performance curve has been qualitatively compared with the experiment from literature. Overall, the simulation results conform to the experimental data despite the difference in SOFC geometry. From the modelling results, the steady-state cell performance is concluded to be significantly dependent on the solid temperature. Additionally, it has been observed that the temperature variation along the SOFC is significant. The mass diffusion limitations have been found to contribute to voltage losses at high current density, whereas the kinetic limitations of the electrode reactions are responsible for the voltage loss at at low current density.

A nominal operating condition is chosen such that it becomes the initial condition for the dynamic simulations. Step changes in the load current densities and the hydrogen concentrations in the fuel source are introduced around the nominal operating condition and the step responses of the output voltage, solid temperature, and outlet gas concentration are obtained. The settling time of the temperature of approximately 400 seconds is reported, whereas the dynamic effects of the output voltage and mass diffusion are substantially small. From the dynamic step responses, the first-order dynamic transfer function models have been derived. These low-order models have been shown to sufficiently capture the main dynamic proper-

ties of the SOFC within a small deviation from the nominal operating condition. A method to control the SOFC output voltage in the presence of load changes is presented. The proposed method is based on varying the inlet hydrogen molar fraction in the fuel to achieve the desired output voltage. The PI controller is implemented in the voltage feedback control loop to adjust the required hydrogen content in the fuel. The PI controller performance gives a satisfactory results in the load disturbance rejection. This would allow assessment of the controller performance at other operating conditions. Before such controller testings are performed, consideration should be given to the choice of nominal operating condition in which the low-order models are derived. The proposed dynamic model provides a useful tool for the SOFC performance prediction and design optimization. Additionally, it has given insight on the dynamic SOFC characteristics and control of SOFC. In SOFC operation, the output voltage decreases with increasing load current. By comparing the simulated data with the experimental data, it is verified that the SOFC process is stable and the output voltage is guaranteed to be finite. A stable controller can be implemented since the model error is compensated for by feedback control.

6.1 Future Work

An approach to the physically-based modelling has been developed. Fundamental understanding of charge-transfer electrochemistry is essential to the development of an accurate SOFC model. Electrochemical reactions play an important role in the determination of SOFC output performance, especially at a cell-level. The electrochemical properties such as the exchange current densities and the charge transfer coefficients must be accurately determined. Additionally, the diffusion mechanisms in the porous electrode must be understood in order to better estimate the limiting current densities in the SOFC.

The final consideration not assessed in the present model is the thermal gradient in the SOFC. From the detailed mathematical SOFC model developed in this work, further investigation can be performed on the thermal stress and material degradation analysis. A prerequisite for the control of SOFC system has been established from the physically-based model in this work. A focus on the control of SOFC can be extended to the mechanical stress simulations by identifying the proper means of control to maintain the material stress

within an acceptable range.

Bibliography

[1] *Fuel Cell Handbook.* Number DOE/NETL-2002/1179. U.S. Department of Energy, Morgantown, 6th edition, November 2002.

[2] *MATLAB 6.5 (R13).* The MathWorks, Inc., 2002.

[3] *Chemical Engineering Module Users Guide.* COMSOL AB., 2004.

[4] *COMSOL Multiphysics 3.2b.* COMSOL AB., 2006.

[5] E. Achenbach. Three-dimensional and time-dependent simulation of a planar solid oxide fuel cell stack. *J. Power Sources*, 49:333–348, 1994.

[6] E. Achenbach. Response of a solid oxide fuel cell to load change. *J. Power Sources*, 57:105–109, 1995.

[7] T. Ackmann, L.G.J. de Haart, W. Lehnert, and D. Stolten. Modeling of mass and heat transport in planar substrate type SOFCs. *J. Electrochem. Soc.*, 150(6):A783–A789, 2003.

[8] P. Aguiar, C.S. Adjimana, and N.P. Brandon. Anode-supported intermediate temperature direct internal reforming solid oxide fuel cell. I: model-based steady-state performance. *J. Power Sources*, 138:120–136, 2004.

[9] P. Aguiar, C.S. Adjimana, and N.P. Brandon. Anode-supported intermediate temperature direct internal reforming solid oxide fuel cell. II: model-based dynamic performance and control. *J. Power Sources*, 147:136–147, 2005.

[10] R.B. Bird, W.E. Steward, and E.N. Lightfoot. *Transport Phenomena.* Wiley International, New York, 2nd edition, 2002.

[11] B. Borglum. The status of SOFC development at Versa Power Systems. Presented at the Ninth International Symposium on Solid Oxide Fuel Cells, Quebec City, QC, Canada, May 16, 2005.

[12] N. Brandon and J. Hill. Short Course: Principles of Fuel Cells. Presented at the 2003 Canadian Fuel Cell Systems Symposium, Calgary, AB, Canada, February 18, 2003.

[13] Industry Canada. Canadian fuel cell commercialization roadmap, March 2003.

[14] Y.A. Çengel. *Heat Transfer: A Practical Approach.* McGraw Hill, New York, 2nd edition, 2003.

[15] S.H. Chan, X.J. Chen, and K.A. Khor. Cathode micromodel of solid oxide fuel cell. *J. Electrochem. Soc.*, 151(1):A164–A172, 2004.

[16] M.W. Chase Jr., C.A. Davies, J.R. Downey Jr., D.J. Frurip, R.A. McDonald, and A.N. Syverud. JANAF Thermochemical Tables, Third Edition, Part II, Cr-Zr. *JPCRD*, 14:1260, 1274, and 1667, 1985.

[17] E. Chen. *Fuel Cell Technology Handbook*, chapter 3 Thermodynamics and Electrochemical Kinetics. CRC Press, Boca Raton, 1st edition, 2003.

[18] M.K. Chyu. Numerical modeling of transport phenomena in solid oxide fuel cells. Presented at the 2005 Taiwan Solid Oxide Fuel Cell Symposium, Taiwan, R.O.C, June 1, 2005.

[19] P. Costamagna and K. Honegger. Modeling of solid oxide heat exchanger integrated stacks and simulation at high fuel utilization. *J. Electrochem. Soc.*, 145(11):3995–4007, 1998.

[20] B. de Boer. *SOFC Anode Hydrogen oxidation at porous nickel and nickel-yttria stabilised zirconia cermet electrodes.* PhD thesis, University of Twente, Twente, The Netherlands, October 1998.

[21] J.R. Ferguson, J.M. Fiard, and R. Herbin. Three-dimensional numerical simulation for various geometries of solid oxide fuel cells. *J. Power Sources*, 58:109–222, 1996.

[22] J.M. Fiard and Herbin R. Comparison between finite volume and finite element methods for an elliptic system arising in electrochemical engineering. *Comput. Methods Appl. Mech. Engrg.*, 115:315–338, 1994.

[23] R.J. Gorte and J.M. Vohs. Novel SOFC anodes for the direct electrochemical oxidation of hydrocarbons. *J. Catal.*, 216:477–486, 2003.

[24] D.J. Hall and R.G. Colclaser. Transient modeling and simulation of a tubular solid oxide fuel cell. *IEEE Transactions on Energy Conversion*, 14(3):749–753, 1999.

[25] C. Haynes. Simulating process settings for unslaved SOFC response to increase in load demand. *J. Power Sources*, 109:365–376, 2002.

[26] M.M. Husssain, X. Li, and I. Dincer. Multi-component mathematical model of solid oxide fuel cell anode. 29:1083–1101, Int. J. Energy Res.

[27] E. Ivers-Tiffée, A. Weber, and D. Herbstritt. Materials and technologies for SOFC-components. *J. Eur. Ceram. Soc.*, 21:1805–1811, 2001.

[28] R.J. Kee, H. Zhu, and D.G. Goodwin. Solid-oxide fuel cells (SOFC) with hydrocarbon and hydrocarbon-derived fuels. Presented at the 30th International Symposium on Combustion, Chicago, Illinois, USA, July 25-30, 2004.

[29] K. Keegan, M. Khaleel, L. Chick, K. Recknagle, S. Simner, and J. Deibler. Analysis of a planar solid oxide fuel cell based automotive auxiliary power unit. *SAE Technical Paper Series 2002-01-0413*, 2002.

[30] M.A. Khaleel, K.P. Recknagle, Z. Lin, J.E. Deibler, L.A. Chick, and J.W. Stevenson. Thermo-mechanical and electrochemistry modeling of planar sofc stacks. *Electrochem. Soc. Proc.*, 16:1032–1041, 2001.

[31] J. Larminie and A. Dicks. *Fuel Cell Systems Explained.* Wiley, West Sussex, 2nd edition, 2003.

[32] S. McIntosh and R.J. Gorte. Direct hydrocarbon solid oxide fuel cells. *Chem. Rev.*, 104:4845–4865, 2004.

[33] N. Minh. Recent advances in SOFC technology. Presented at the American Ceramic Society PCRM, Seattle, WA, USA, October 1-4, 2002.

[34] A. Nakajo, C. Stiller, G. Härkegård, and O. Bolland. Modeling of thermal stresses and probability of survival of tubular SOFC. *J. Power Sources.*, 158:287–294, 2006.

[35] K. Nishida, T. Takagi, and S. Kinoshita. Process analysis and evaluation of exergy loss in solid oxide fuel cell. *JSME Int J., Ser. B*, 47(4):786–794, 2004.

[36] T. Ota, M. Koyama, C. Wen, K. Yamada, and H. Takahashi. Object-based modeling of SOFC system dynamic behavior of micro-tube SOFC. *J. Power Sources*, 118:430–439, 2003.

[37] J. Padullés, G.W. Ault, and J.R. McDonald. An integrated SOFC plant dynamic model for power systems simulation. *J. Power Sources*, 86:495–500, 2000.

[38] U. Pasaogullari and C.Y. Wang. Computational fluid dynamics modeling of solid oxide fuel cells. *Proceeding of the 8th International Symposium on Solid Oxide Fuel Cells* (SOFC-VIII), pages 1403–1412, 2003. S.C. Singhal and M. Dokiya (Eds.), Pennington, NJ.

[39] B.E. Poling, J.M Prausnitz, and J.P. O'Connell. *The Properties of Gases and Liquids*. McGraw Hill Book Company, New York, 5th edition, 2001.

[40] Y. Qi, B. Huang, and K.T. Chuang. Dynamic modeling of solid oxide fuel cell: The effect of diffusion and inherent impedance. *J. Power Sources*, 150:32–47, 2005.

[41] S.K. Ratkje and K.S. Førland. The transported entropy of oxygen ion in YSZ. *J. Electrochem Soc.*, 138(8):2374–2376, 1991.

[42] S.K. Ratkje and S. Møller-Holst. Exergy efficiency and local heat production in solid oxide fuel cells. *Electrochimica Acta*, 38(2/3):447–453, 1993.

[43] S.K. Ratkje and Y. Tomii. Transported entropy in Zirconia with 3 to 12 mole percent Yttria. *J. Electrochem Soc.*, 140(1):59–66, 1993.

[44] D.E. Seborg, T.F. Edgar, and D.A. Mellichamp. *Process Dynamics and Controls*. Wiley, New York, 1st edition, 1989.

[45] P. Singh and N.Q. Minh. Solid oxide fuel cells: Technology status. *Int. J. Appl. Ceram. Technol.*, 1(1):5–15, 2004.

[46] S.C. Singhal. Science and technology of solid-oxide fuel cells. *MRS Bulletin*, pages 16–21, 2000.

[47] S.C. Singhal and K. Kendall. *High Temperature Solid Oxide Fuel Cells Fundamentals, Designs, and Applications*. Elsevier, Oxford, UK, 2003.

[48] C. Stiller, B. Thorud, O. Bolland, R. Kandepu, and L. Imsland. Control strategy for a solid oxide fuel cell and gas turbine hybrid system. *J. Power Sources*, 158:303–315, 2006.

[49] B. Thorud, O. Bolland, and H.M. Kvamsdal. Modelling and simulation of transient behaviour of SOFC. 2002. Presented at the Symposium on Polymer Fuel Cells, Throndheim, Norway, September 13, 2002.

[50] B. Todd and J.B. Young. Thermodynamic and transport properties of gases for use in SOFC modeling. *J. Power Sources*, 110:186–200, 2002.

[51] J.D. VanderSteen, B. Kenney, J.G. Pharoah, and K. Karan. Mathematical modelling of the transport phenomena and the chemical/electrical reactions in solid oxide fuel cells: A review. Presented at the Canadian Hydrogen and Fuel Cells Conference, Toronto, Ontario, Canada, September 25-28, 2004.

[52] R.E. Williford, L.A. Chick, G.D. Maupin, S.P. Simner, and J.W. Stevenson. Diffusion limitations in the porous anodes of SOFCs. *J. Electrochem. Soc.*, 150(8):A1067–A1072, 2003.

[53] Z.T. Xia, S.H. Chan, and K.A. Khor. An improved anode micro model of SOFC. *Electrochem. Solid-State Lett.*, 7(3):A63–A65, 2004.

[54] H. Yakabe, M. Hishinuma, M. Uratani, Y. Matsuzaki, and I. Yasuda. Evaluation and modeling of performance of anode-supported solid oxide fuel cell. *J. Power Sources*, 86:423–431, 2000.

[55] F. Zenith and S. Skogestad. Dynamic modelling for control of fuel cells. 2004. Presented at the 2004 AIChE Annual Meeting Conference, Austin, TX, November 7-12, 2004.

[56] F. Zenith and S. Skogestad. Control of a fuel-cell powered DC electric vehicle motor. 2005. Presented at the 2005 AIChE Annual Meeting Conference, Cincinnati, OH, USA, November 2, 2005.

[57] H. Zhu and R.J. Kee. A general mathematical model for analyzing the performance of fuel-cell membrane-electrode assemblies. *J. Power Sources*, 117:61–74, 2003.

Appendix A

Thermodynamics of Hydrogen Fuel Cell

Appendix A contains an estimation of enthalpy change, entropy change, and Gibbs energy of reactions in solid oxide fuel cells.

A.1 Enthalpy of Reaction

The enthalpy change (ΔH) is calculated from the difference between the enthalpy of the products and the reactants. For the overall reaction in hydrogen fuel cell ($H_2+\frac{1}{2}O_2 \rightarrow H_2O$), it follows that the overall enthalpy change is

$$\Delta H(T) = H(T)_{H_2O} - H(T)_{H_2} - \frac{1}{2}H(T)_{O_2} \tag{A.1}$$

The species enthalpy, $H_i(T)$, is given by

$$H_i(T) = H_i(298.15K) + \int_{298.15K}^{T} C_{p,i}(T)dT \tag{A.2}$$

Here, the standard temperature is $298.15K$ and C_p is the molar heat capacity at constant pressure. The method for calculating $C_{p,i}(T)$ can be found in Appendix B.

A.2 Entropy of Reaction

Since the entropy is a measure of disorder in the system, the entropy change of hydrogen fuel cell, (ΔS), is present as a result of the electrochemical reactions. For the overall reaction in

hydrogen fuel cell, the entropy change is defined as

$$\Delta S(T) = S(T)_{H_2O} - S(T)_{H_2} - \frac{1}{2}S(T)_{O_2} \tag{A.3}$$

where the molar entropy of species i at a specified temperature T is given by

$$S_i(T) = S_i(298.15K) + \int_{298.15K}^{T} \frac{1}{T} C_{p,i}(T)dT \tag{A.4}$$

The values of molar enthalpy and entropy for various species in hydrogen fuel cell at 298.15 K and 0.1 MPa are given in Table A.1 [31].

Table A.1: Summary of molar enthalpy and entropy at 298.15 K and 0.1 MPa for the hydrogen fuel cell [31].

Species i	$H_i(298.15K)$ (J/mol)	$S_i(298.15K)$ (J/molK)
H_2O (steam)	-241,827	188.83
H_2	0	130.59
O_2	0	205.14

A.3 Gibbs Free Energy

The Gibbs free energy is defined in terms of the enthalpy and entropy of a system.

$$G = H - TS \tag{A.5}$$

The change in Gibbs energy at a constant temperature can be obtained from the above equation in a differential form shown below.

$$\Delta G = \Delta H - T\Delta S \tag{A.6}$$

Here, the values of ΔH and ΔS are obtained from Equation (A.1) and (A.3), respectively. The term $T\Delta S$ represents the amount of heat generated by a fuel cell operating reversibly. This property can either be positive or negative, which reflects the endothermic or the exothermic heat effects, respectively.

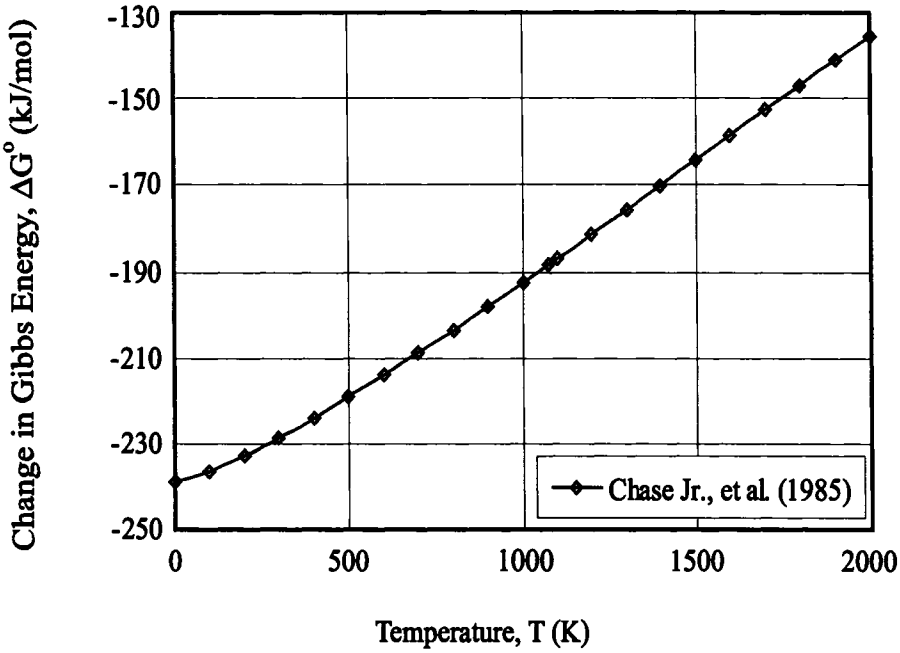

Figure A.1: Change in Gibbs free energy of water formation at standard state (0.1 MPa) as a function of temperature [16].

The standard change in Gibbs free energy ($\Delta G^\circ(T)$) refers to the change of Gibbs energy at a standard pressure of 0.1 MPa (1 bar). For temperatures between 0 K–2,000 K, the standard change in Gibbs energy for hydrogen fuel cell is illustrated in Figure A.1.

The standard change in Gibbs energy is an important thermodynamic parameter which determines the electrode potential of a fuel cell at standard state.

A.3.1 Standard Electrode Potential

The standard electrode potential at equilibrium represents the theoretically maximum voltage which can be achieved at standard state. This potential is a function of temperature and is calculated from the standard change in Gibbs energy.

$$E^\circ(T) = -\frac{\Delta G^\circ(T)}{n_e F} \tag{A.7}$$

where n_e is the number of electrons involved in the electrochemical reaction ($n_e = 2$), and F is the Faraday's constant. The standard electrode potential E° as a function of temperature is shown in Figure A.2

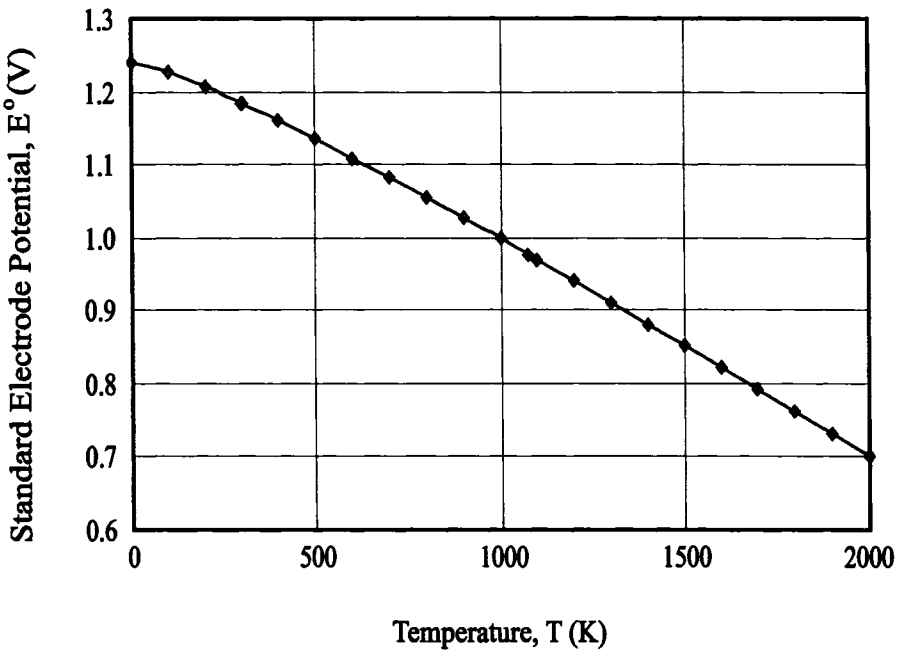

Figure A.2: Standard electrode potential of a hydrogen fuel cell as a function of temperature at 0.1 MPa.

Appendix B

Estimation of Gas Property

Appendix B contains methods of gas property estimation at various temperature. Recommended method of calculating the binary diffusivity, dynamic viscosity, isobaric molar heat capacity, thermal conductivity, and convective heat transfer coefficient of the gas mixtures are presented.

B.1 Gas Binary Diffusivity

The binary diffusivity of a pair of gaseous species is calculated using the Chapman-Enskog kinetic theory.

$$D_{ik} = \frac{(1.8583 \times 10^{-7})T^{1.5}}{P\hat{\sigma}_{ik}^2 \hat{\Omega}_{D,ik}} \left(\frac{1}{MW_i} + \frac{1}{MW_k} \right)^{0.5} \tag{B.1}$$

where $D_{i,k}$ is the bulk diffusivity of a binary gas mixture in m^2/s, P is the total gas pressure, $\hat{\sigma}_{ik}$ is the average collision diameter, $\hat{\Omega}_{D,ik}$ is the collision integral based on the Lennard-Jones potential, and MW is the gas molecular weight. The parameter $\hat{\sigma}_{ik}$ is determined from an average value of the collision diameters of i and k [10].

$$\hat{\sigma}_{ik} = \frac{1}{2}(\hat{\sigma}_i + \hat{\sigma}_k) \tag{B.2}$$

The collision integral between molecule i and k is a function of the dimensionless term $k_B T/\varepsilon_{ik}$, where k_B is the Boltzmann's constant with a value of 1.38066×10^{-23} J/K. The parameter ε_{ik} is estimated from

$$\varepsilon_{ik} = \sqrt{\varepsilon_i \varepsilon_k} \tag{B.3}$$

The parameters $\hat{\sigma}_i$ and ε_i/k_B are tabulated in Table B.1 [10, 39].

Table B.1: Collision diameter and dimensionless temperature parameter from the Lennard-Jones potentials [10].

Species i	$\hat{\sigma}_i$ (Å)	ε_i/k_B (K)
H_2	2.827	59.7
H_2O	2.641	809.1
N_2	3.798	71.4
O_2	3.467	106.7

The collision integrals have been curve-fitted using the Lennard-Jones 12–6 potential model [39]. The relationship is given by

$$\hat{\Omega}_{D,ik} = \frac{1.06036}{T^{*0.15610}} + \frac{0.19300}{\exp(0.47635T^*)} + \frac{1.03587}{\exp(1.52996T^*)} + \frac{1.76474}{\exp(3.89411T^*)} \quad \text{(B.4)}$$

where

$$T^* = \frac{k_B T}{\varepsilon_{ik}} \quad \text{(B.5)}$$

At 1,073 K and 1 atm, the binary diffusivity of O_2-N_2 in air as determined by Equation (B.1) is approximately 1.81×10^{-4} m^2/s.

B.2 Dynamic Viscosity of Multicomponent Gas Mixtures

The dynamic viscosity of a pure component, μ, can be calculated from a polynomial relationship as provided by Todd and Young (2002) [50]

$$\mu_i(T) = \sum_{k=0}^{6} a_k \tau^k \quad \text{(B.6)}$$

where a_k is the coefficients given in Table B.2 and

$$\tau = \frac{T}{1000} \quad \text{(B.7)}$$

here, μ_i is the dynamic viscosity of a pure component i in micro-poise (μP).

To calculate the dynamic viscosity of a gas mixture with n components, the Reichenberg expression is employed [39].

$$\mu_{mix} = \sum_{i=1}^{n} K_i \left(1 + 2\sum_{j=1}^{i-1} H_{ij} K_j + \sum_{j=1\neq i}^{n} \sum_{k=1\neq i}^{n} H_{ij} H_{ik} K_j K_k \right) \quad \text{(B.8)}$$

Table B.2: Coefficients to calculate the dynamic viscosity in Equation (B.6)

Species	a_0	a_1	a_2	a_3	a_4	a_5	a_6	Error(%)
H_2	15.553	299.78	-244.34	249.41	-167.51	62.966	-9.9892	10
H_2O	-6.7541	244.93	419.50	-522.38	348.12	-126.96	19.591	3
N_2	1.2719	771.45	-809.20	832.47	-553.93	206.15	-32.430	3
O_2	-1.6918	889.75	-892.79	905.98	-598.36	221.64	-34.754	5

where

$$K_i = \frac{x_i \mu_i}{x_i + \mu_i \sum_{k=1 \neq i}^{n} x_k H_{ik} \left[3 + \left(\frac{2MW_k}{MW_i}\right)\right]} \tag{B.9a}$$

$$H_{ij} = \left[\frac{MW_i MW_j}{32(MW_i + MW_j)^3}\right]^{1/2} * (C_i + C_j)^2 \frac{[1 + 0.36T_{rij}(T_{rij} - 1)]^{1/6} F_{Rij}}{T_{rij}^{1/2}} \tag{B.9b}$$

$$C_i = \frac{M_i^{1/4}}{(\mu_i U_i)^{1/2}} \tag{B.9c}$$

$$U_i = \frac{[1 + 0.36T_{ri}(T_{ri} - 1)]^{1/6} F_{Ri}}{T_{ri}^{1/2}} \tag{B.9d}$$

$$T_{ri} = \frac{T}{T_{ci}}, \tag{B.9e}$$

$$F_{Ri} = \frac{T_{ri}^{3.5} + (10\xi_{ri})^7}{T_{ri}^{3.5} + [1 + (10\xi_{ri})^7]} \tag{B.9f}$$

$$\xi_{ri} = 52.46 \frac{\xi_i^2 P_{ci}}{T_{ci}^2} \tag{B.9g}$$

$$T_{rij} = \frac{T}{(T_{ci} T_{cj})^{1/2}} \tag{B.9h}$$

$$F_{Rij} = \frac{T_{rij}^{3.5} + (10\xi_{rij})^7}{T_{rij}^{3.5}[1 + (10\xi_{rij})^7]} \tag{B.9i}$$

$$\xi_{rij} = (\xi_{ri}\xi_{rj})^{1/2} \tag{B.9j}$$

Here, μ_{mix} is the dynamic viscosity of gas mixture (μP), μ_i is the dynamic viscosity of pure component i (μP), x_i is the mole fraction of species i, MW is the molecular weight (kg/kmol), ξ is the dipole moment (debye), T_c is the critical temperature (K), and P_c is the critical pressure (bar). The gas property data is tabulated in Table B.3.

Table B.3: Gas property data used in the dynamic viscosity of a gas mixture calculation

Species i	MW (kg/kmol)	T_c (K)	P_c (bar)	ξ (debye)
H_2	2.016	33.25	12.97	0
H_2O	18.015	647.14	220.64	1.8
N_2	28.014	126.2	33.98	0
O_2	31.999	154.58	50.43	0

At 1,073 K, the dynamic viscosity of pure N_2 and O_2 are 435.25 and 513.38 μP, respectively, as determined by Equation (B.6). For the gas mixture of 79 mol% N_2 and 21 mol% O_2 (air), the mixed dynamic viscosity is approximately 450.85 μP as determined by the method of Reichenberg.

B.3 Isobaric Heat Capacity of Multicomponent Gas Mixtures

The Isobaric heat capacity of a pure component was calculated from a polynomial relationship as provided by Todd and Young (2002). [50].

$$C_{p,i}(T) = \sum_{k=0}^{6} b_k \tau^k \tag{B.10}$$

$$\tau = \frac{T}{1000} \tag{B.11}$$

Here, $C_{p,i}(T)$ is the specific heat capacity of component i (kJ/kmol K) at a given temperature T (K). The coefficient b_k is given in Table B.4.

Table B.4: Coefficients to calculate the isobaric heat capacity of pure gas in Equation (B.10)

Species	b_0	b_1	b_2	b_3	b_4	b_5	b_6	Error(%)
H_2	21.157	56.036	-150.55	199.29	-136.15	46.903	-6.4725	1
H_2O	37.373	-41.205	146.01	-217.08	181.54	-79.409	14.015	1
N_2	29.027	4.8987	-38.040	105.17	-113.56	55.554	-10.350	1
O_2	34.850	-57.975	203.68	-300.37	231.72	-91.821	14.776	1

The heat capacity of a gas mixture, $C_{p,mix}$, is calculated by accounting for the mole fraction of each gas species.

$$C_{p,mix}(T) = \sum_{i=1}^{n} x_i C_{p,i}(T) \tag{B.12}$$

where x_i is the mole fraction and $C_{p,i}$ is the heat capacity of species i. At 1,073 K, the molar specific heat capacity of N_2 and O_2 are 33.1 kJ/kmolK and 35.2 kJ/kmolK, respectively, as determined by Equation (B.10). Using Equation (B.12), the specific heat capacity of air (O_2-N_2 mixture) at 1,073 K is determined to be 33.5 kJ/kmolK.

B.4 Thermal Conductivity of Multicomponent Gas Mixtures

The thermal conductivity of a pure gas component, k, is calculated from a polynomial relationship as provided by Todd and Young (2002) [50].

$$k_i(T) = \sum_{k=0}^{6} c_k \tau^k \tag{B.13}$$

$$\tau = \frac{T}{1000} \tag{B.14}$$

Here, k_i is the thermal conductivity of a pure component i in W/mK. The coefficients c_k are given in Table B.5.

Table B.5: Coefficients to calculate the gas thermal conductivity in Equation (B.13)

Species	c_0	c_1	c_2	c_3	c_4	c_5	c_6	Error(%)
H_2	1.5040	62.892	-47.190	47.763	-31.939	11.972	-1.8954	5
H_2O	2.0103	-7.9139	35.922	-41.390	35.993	-18.974	4.1531	1
N_2	-0.3216	14.810	-25.473	38.837	-32.133	13.493	-2.2741	5
O_2	-0.1857	11.118	-7.3734	6.7130	-4.1797	1.4910	-0.2278	10

For a gas mixture, the effective thermal conductivity can be calculated using the expression [39]

$$k_{mix} = \sum_{i=1}^{n} \frac{x_i k_i}{\sum_{j=1}^{n} x_j A_{ij}} \tag{B.15}$$

where

$$A_{ij} = \frac{\epsilon \left[1 + \left(\frac{k_{tri}}{k_{trj}}\right)^{1/2} \left(\frac{MW_i}{MW_j}\right)^{1/4}\right]^2}{\left[8\left(1 + \frac{MW_i}{MW_j}\right)\right]^{1/2}} \tag{B.16a}$$

$$\frac{k_{tri}}{k_{trj}} = \frac{\mu_i MW_j}{\mu_j MW_i} \tag{B.16b}$$

Here, k is the thermal conductivity of the gas mixture (W/mK), μ is the dynamic viscosity (μP), x_i is the mole fraction of species i, MW is the molecular weight (kg/kmol), and ϵ is the numerical constant, taken as 1.0 [50]. At 1,073 K, the thermal conductivities of N_2 and O_2 as determined by Equation (B.13) are 7.35×10^{-2} W/mK and 7.78×10^{-2} W/mK, respectively. Using Equation (B.15), the mixed thermal heat conductivity of air at 1,073 K is calculated to be 7.74×10^{-2} W/mK.

B.5 Convective Heat Transfer Coefficient

The convective heat transfer coefficient is approximated as an average value over the entire flow channel. The average heat transfer coefficient, h, is determined from an average of the dimensionless Nusselt number (Nu). For laminar flow over the entire flow path, the Nusselt number is defined as

$$\mathrm{Nu} = \frac{hL}{k} = 0.664\mathrm{Re}^{0.5}\mathrm{Pr}^{1/3}, \mathrm{Re} < 5 \times 10^5 \tag{B.17}$$

where h is the average convective heat transfer coefficient in W/m^{2}K, k is the thermal conductivity of fluid and L is the characteristic length of the flow channel [14]. The dimensionless Reynolds number (Re) and Prandtl number (Pr) are defined as

$$\mathrm{Re} = \frac{\rho u_\infty L}{\mu} \tag{B.18}$$

$$\mathrm{Pr} = \frac{\mu C_p}{k} \tag{B.19}$$

where, ρ is the fluid density, u_∞ is the upstream fluid velocity, μ is the dynamic viscosity, and C_p is the specific heat capacity of the fluid.

Appendix C

Modelling Parameters

The modelling parameters discussed in Chapter 3 are tabulated in Table C.1.

Table C.1: Modelling parameters.

Description	Symbol	Value	Unit	Ref.
Specific heat capacity of anode	$C_{p,A}$	377	J/(kgK)	[18]
Specific heat capacity of anode interconnect	$C_{p,AI}$	300	J/(kgK)	[18]
Specific heat capacity of cathode	$C_{p,C}$	377	J/(kgK)	[18]
Specific heat capacity of cathode interconnect	$C_{p,CI}$	300	J/(kgK)	[18]
Specific heat capacity of electrolyte	$C_{p,E}$	100	J/(kgK)	[18]
Thermal conductivity of anode	k_A	11.0	W/(mK)	[18]
Thermal conductivity of anode interconnect	k_{AI}	2.2	W/(mK)	[18]
Thermal conductivity of cathode	k_C	2.37	W/(mK)	[18]
Thermal conductivity of cathode interconnect	k_{CI}	2.34	W/(mK)	[18]
Thermal conductivity of electrolyte	k_E	2.7	W/(mK)	[18]
Mean pore radius of anode	$\bar{r}_A$	1.07×10^{-6}	m	[7]
Mean pore radius of cathode	$\bar{r}_C$	1.0×10^{-6}	m	[57]
Emissivity of anode	ϵ_A	0.855		[19]
Emissivity of anode interconnect	ϵ_{AI}	0.1		[8]
Emissivity of cathode	ϵ_C	0.855		[19]
Emissivity of cathode interconnect	ϵ_{CI}	0.1		[8]
Permeability of anode	κ_A	1.7×10^{-10}	m^2	[54]
Permeability of cathode	κ_C	1.76×10^{-11}	m^2	[38]
Density of anode	ρ_A	4,760	kg/m^3	[18]
Density of anode interconnect	ρ_{AI}	4,760	kg/m^3	[18]

Continued on next page

Table C.1 Modelling parameters – continued from previous page

Description	Symbol	Value	Unit	Ref.
Density of cathode	ρ_C	4,640	kg/m^3	[18]
Density of cathode interconnect	ρ_{CI}	4,640	kg/m^3	[18]
Density of electrolyte	ρ_E	6,000	kg/m^3	[18]
Tortuosity of anode	τ_A	8.5	(m/m)^2	Adjusted value
Tortuosity of cathode	τ_C	2.5	(m/m)^2	[15]
Porosity of anode	ε_A	0.3		[19]
Porosity of cathode	ε_C	0.3		[19]